NANOELECTRODE AND NANOPARTICLE BASED BIOSENSORS FOR ENVIRONMENTAL AND HEALTH MONITORING

by

LATEEF UDDIN SYED

B. Tech, University of Mumbai, 2005

AN ABSTRACT OF A DISSERTATION

submitted in partial fulfillment of the requirements for the degree

DOCTOR OF PHILOSOPHY

Department of Chemistry
College of Arts and Sciences

KANSAS STATE UNIVERSITY
Manhattan, Kansas

2012

Abstract

Reduction in electrode size down to nanometers dramatically enhances the detection sensitivity and temporal resolution. Here we explore nanoelectrode arrays (NEAs) and nanoparticles in building high performance biosensors.

Vertically aligned carbon nanofibers (VACNFs) of diameter ~100 nm were grown on a Si substrate using plasma enhanced chemical vapor deposition. SiO_2 embedded CNF NEAs were then fabricated using techniques like chemical vapor deposition, mechanical polishing, and reactive ion etching, with CNF tips exposed at the final step. The effect of the interior structure of CNFs on electron transfer rate (ETR) was investigated by covalently attaching ferrocene molecules to the exposed end of CNFs. Anomalous differences in the ETR were observed between DC voltammetry (DCV) and AC voltammetry (ACV). The findings from this study are currently being extended to develop an electrochemical biosensor for the detection of cancerous protease (legumain). Preliminary results with standard macro glassy carbon electrodes show a significant decrease in ACV signal, which is encouraging.

In another study, NEA was employed to capture and detect pathogenic bacteria using AC dielectrophoresis (DEP) and electrochemical impedance spectroscopy (EIS). A nano-DEP device was fabricated using photolithography processes to define a micro patterned exposed active region on NEA and a microfluidic channel on macro-indium tin oxide electrode. Enhanced electric field gradient at the exposed CNF tips was achieved due to the nanometer size of the electrodes, because of which each individual exposed tip can act as a potential DEP trap to capture the pathogen. Significant decrease in the absolute impedance at the NEA was also observed by EIS experiments.

In a final study, we modified gold nanoparticles (GNPs) with luminol to develop chemiluminescence (CL) based blood biosensor. Modified GNPs were characterized by UV-Vis, IR spectroscopy and TEM. We have applied this CL method for the detection of highly diluted blood samples, in both intact and lysed forms, which releases Fe^{3+} containing hemoglobin to catalyze the luminol CL. Particularly, the lysed blood sample can be detected even after 10^8 dilution (corresponding to ~0.18 cells/well). This method can be readily developed as a portable biosensing technique for rapid and ultrasensitive point-of-care applications.

NANOELECTRODE AND NANOPARTICLE BASED BIOSENSORS FOR ENVIRONMENTAL AND HEALTH MONITORING

by

LATEEF UDDIN SYED

B. Tech, University of Mumbai, 2005

A DISSERTATION

submitted in partial fulfillment of the requirements for the degree

DOCTOR OF PHILOSOPHY

Department of Chemistry
College of Arts and Sciences

KANSAS STATE UNIVERSITY
Manhattan, Kansas

2012

Approved by:

Major Professor
Dr. Jun Li

Copyright

Abstract

Reduction in electrode size down to nanometers dramatically enhances the detection sensitivity and temporal resolution. Here we explore nanoelectrode arrays (NEAs) and nanoparticles in building high performance biosensors.

Vertically aligned carbon nanofibers (VACNFs) of diameter ~100 nm were grown on a Si substrate using plasma enhanced chemical vapor deposition. SiO_2 embedded CNF NEAs were then fabricated using techniques like chemical vapor deposition, mechanical polishing, and reactive ion etching, with CNF tips exposed at the final step. The effect of the interior structure of CNFs on electron transfer rate (ETR) was investigated by covalently attaching ferrocene molecules to the exposed end of CNFs. Anomalous differences in the ETR were observed between DC voltammetry (DCV) and AC voltammetry (ACV). The findings from this study are currently being extended to develop an electrochemical biosensor for the detection of cancerous protease (legumain). Preliminary results with standard macro glassy carbon electrodes show a significant decrease in ACV signal, which is encouraging.

In another study, NEA was employed to capture and detect pathogenic bacteria using AC dielectrophoresis (DEP) and electrochemical impedance spectroscopy (EIS). A nano-DEP device was fabricated using photolithography processes to define a micro patterned exposed active region on NEA and a microfluidic channel on macro-indium tin oxide electrode. Enhanced electric field gradient at the exposed CNF tips was achieved due to the nanometer size of the electrodes, because of which each individual exposed tip can act as a potential DEP trap to capture the pathogen. Significant decrease in the absolute impedance at the NEA was also observed by EIS experiments.

In a final study, we modified gold nanoparticles (GNPs) with luminol to develop chemiluminescence (CL) based blood biosensor. Modified GNPs were characterized by UV-Vis, IR spectroscopy and TEM. We have applied this CL method for the detection of highly diluted blood samples, in both intact and lysed forms, which releases Fe^{3+} containing hemoglobin to catalyze the luminol CL. Particularly, the lysed blood sample can be detected even after 10^8 dilution (corresponding to ~0.18 cells/well). This method can be readily developed as a portable biosensing technique for rapid and ultrasensitive point-of-care applications.

Table of Contents

List of Figures

List of Tables

Acknowledgements

It has been almost five years since I started my journey as a graduate student at KSU. I have been working very hard to reach my goal, and finally I am about to get it done. During this journey, I have met lots of great people who helped me improve myself professionally and contribute to the scientific community.

Among all those people, first I would like to thank my major professor, Professor. Jun Li for giving me the opportunity to be his student. I had a great PhD study in this interesting research field under his supervision. His positive and motivating attitude towards research has always helped me to feel the joy and pleasure of working with him. I would also like to thank Dr. Li for nominating my name for several awards!

Special thanks goes to all former and present Li group members: Dr. Jianwei Liu, Jeremy Essner, Qin Li, Dr. Yifen Li, Steven Klankowski, Luxi Zhang, Foram Madiyar, Dr. Caihong Chen, Yichen Zheng, and Yiqun Yang. Thank you Dr. Liu for growing numerous CNF chips and training me to use SEM, and Dr. Yifen for teaching me bacteria labeling and basic biological techniques.

I would like to thank Professors Duy Hua, Christopher Culbertson, and Vikas Berry for being in my committee, and for their valuable suggestions during PhD proporal exam. I also thank Professor. Deon Van Der Merwe for serving as a chair of my committee and conducting the final defense exam.

I really appreciate Prof. Culbertson for giving me the freedom to use several equipments in his lab. Thank you Dr. Alexander Price (former Culbertson group member) for teaching me basics of lithography and train me to use several instruments in Prof. Culbertson's lab.

I thank Prof. Hua and Allan Prior (Hua group member) for their continued support on legumain project. Thanks Prof. Deryl Troyer and Siva Sai (Troyer group member) for letting me use IVIS Lumina instrument. Thank you Prof. Judy Wu and Prof. Mark Richter for your valuable discussions and help during blood biosensor project work. Also would like to thank Dr. Dan Boyle from biology department for training me to use SEM and TEM.

I thank chemistry department for their assistance when I was TA. Also several people at chemistry department, especially, Tobe Eggers, Ron Jackson, Earline Dikeman, Jim Hodgson, Mary Dooley and Kim Ross have helped me a lot for different things, thank you all.

I would like to acknowledge the financial support for the research in my thesis from Kansas State University, Terry C. Johnson Center for Basic Cancer Research at KSU, Early Warning Inc., a NIH COBRE grant (grant number P20RRo15563 from the National Center for Research Resources, PI: B. N. Timmermann, the University of Kansas), and National Cancer Institute (grant number R15CA159250-01, PI: Jun Li). I also thank Institute of Advanced Medical Innovation (IAMI), University of Kansas for supporting Blood detection project.

I thank PLU committee for recognizing me with the classroom (2009) award. I thank Kansas-Bio for choosing me as one of winner's from KSU at Capitol Graduate Research Summit at Topeka for the year 2011. Thank you Graduate Student's Council for organizing KSU Research Forum, giving me the opportunity to present my research work, and recognizing me with a 2nd prize for my talk. Thank you Drs. Charles Chaffin and Timothy Marshall for establishing "Fateley-Hammaker Collaboration in Research" award, and selecting me as 2011-2012 recipient of this award. I thank the KSU research foundation and the committee members for recognizing me with doctoral scholarship award for the year 2011-2012.

I have been lucky to have very good friends around me all the time, without whom I feel the journey of my life would have been more difficult. Thank you Aditya, Prashant & Smita, Baliah, Pavan, Bansal, Vinod, Harsha, Balaji, Vignesh, Goli, and Arshad. Thanks Adi and Vinod for introducing me to KSU chemistry department. At KSU, I made many wonderful friends: Gali, Mustafa, Prasad, Mausam, Sreeram & Vindya, Amit & Meera, Santanu & Jhinuk, Abhinav & Uma, Vishruth, Hussain and Obair. Thank you all for the wonderful time we spent.

I thank my parents and all other family members for being with me, supporting me in all my decisions, continuously motivating, and believing that I can do it. Thanks for all your love, prayers, and support!

Finally, I would like to thank my wife Fehmida for being with me all the time. Thanks for everything! Thanks Almighty for blessing us with Alisha…her presence has made our life more beautiful. Thank you Prashant & Smita for your love and care for Alisha.

Dedication

“To all my loved ones”

List of Abbreviations

AC	Alternating Current
ACV	Alternating Current Voltammetry
Ala	Alanine
Asn	Asparagine
CE	Counter Electrode
CL	Chemiluminescence
CM	Clausius Mossotti
CNF	Carbon Nanofiber
CNT	Carbon Nanotube
CV	Cyclic Voltammetry
CVD	Chemical Vapor Deposition
DC	Direct Current
DEP	Dieletrophoresis
DI	Deionized
DNA	Deoxyribonucleic acid
E. coli	*Escherichia coli*
EDC	1-ethyl-3-(3-dimethylaminopropyl) carbodiimide hydrochloride
EIS	Electrochemical Impedance Spectroscopy
ELISA	Enzyme-linked Immunosorbent Assay
ETR	Electron Transfer Rate
Fc	Ferrocenylmethylamine
GCE	Glassy Carbon Electrode
GNP	Gold Nanoparticle
HPLC	High Performance Liquid Chromatography
ITO	Indium tin oxide
Leu	Leucine
LUM	Luminol
MES	2-(N-morpholino)ethanesulfonic acid
MS	Mass Spectroscopy

MUA	Mercaptoundecanoic acid
MWCNF	Multi-walled Carbon Nanofiber
MWCNT	Multi-walled Carbon Nanoelectrode
NE	Nanoelectrode
NEA	Nanoelectrode Array
pNEA	Patterned Nanoelectrode Array
NHS	*N*-hydrosuccinimide
NP	Nanoparticle
PBS	Phosphate Buffered Saline
PCR	Polymerase Chain Reaction
PECVD	Plasma Enhanced Chemical Vapor Deposition
RE	Reference Electrode
RIE	Reactive Ion Etching
RNA	Ribonucleic acid
SEM	Scanning Electron Microscopy
TEM	Transmission Electron Microscopy
VACNF	Vertically Aligned Carbon Nanofiber
WE	Working Electrode

Chapter 1 - Introduction

This dissertation describes the development of biosensing strategies utilizing nanoelectrode arrays (NEAs) and nanoparticles (NPs) for their applications in, pathogen and trace blood detection respectively. It also details a key finding of the unique advantage offered by nanoelectrodes made of vertically aligned carbon nanofibers (VACNFs), which can be used to build high performance electrochemical biosensors for cancerous protease detection.

In this chapter, I will begin by giving an overview on the concept of biosensors, conventional detection methods, and nanomaterials that are currently employed for biosensing. This will lead us to an introduction of NEAs and NPs based biosensing strategies. I will conclude the chapter with an outline of the dissertation.

1.1 Principles and significance of biosensors

Principle

Biosensor is a device which can be used to detect and quantify different target analytes. International Union of Pure and Applied Chemistry (IUPAC) defines a biosensor as "a device that uses specific biochemical reactions mediated by isolated enzymes, immunosystems, tissues, organelles or whole cells to detect chemical compounds usually by electrical, thermal or optical signals".[1] Several interdisciplinary researchers from areas like chemistry, physics, life sciences, electrical engineering, chemical engineering, mechanical engineering, and nanotechnology have been actively contributing towards the progress of developing biosensors for various applications. The concept of biosensors emerged due to current demand for rapid, cheap, and easy-to-use methods, for qualitative and quantitative determination of different analytes. Biosensors find their applications in fields like medicinal or clinical research, environment and food safety (meat and poultry industries), agricultural inspections, and military investigations. The function of biosensors mainly relies on the combination of two components (1) a biologically selective materials such as enzyme, antibody, or DNA, and (2) a physicochemical transducer as shown in Figure 1.1.[2] The specificity of a biosensor depends on the selectivity of the materials derived from the biological organisms. Biosensors respond selectively to the target or analyte via a specific receptor (biological material) and convert biological recognition event into an electronic signal with the help of a transducer. In general,

biosensors are expected to be advantageous compared to the traditional methods, and be able to provide reliable real time signal.[3-4] The unique combination of biological element in direct

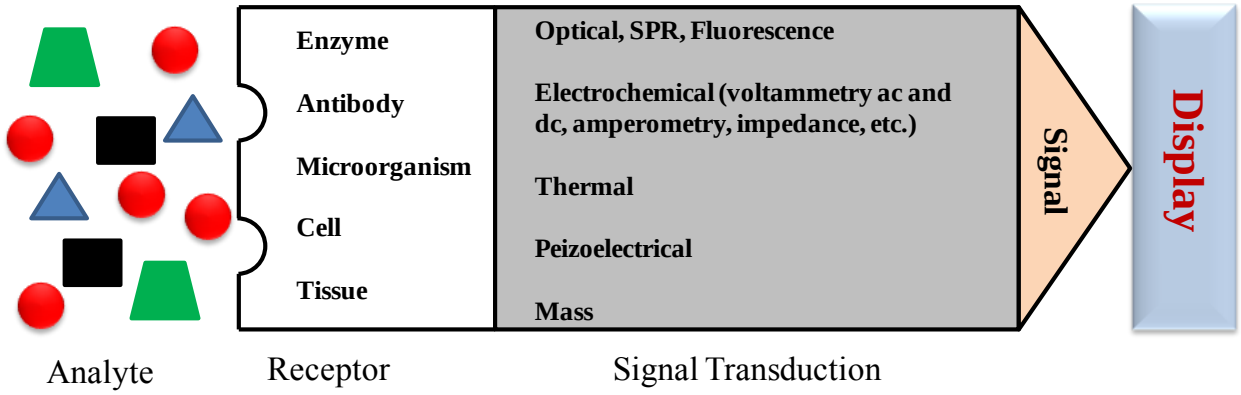

contact with a transducer makes it possible to realize these requirements.

Figure 1.1 Schematic showing the concept and different components of a biosensor.

When designing biosensors, it is essential to study and understand each component that constitutes this complex system as well as all the factors that influence its performance which in some cases might limit its use.[5-6] Though there have been a large number of reports published in the field of biosensor, several aspects require further careful optimization and improvements. Most of the developments are hindered due to inadequate or insufficient understanding of the underlying mechanism by which the material functions. Since in many cases the type of material used is related to the transducer, a considerable attention has to be paid to the type and nature of the transducer material employed for biosensing. Advancements made by the materials chemists have boosted the development of new sensing materials. This led to the use of novel materials to construct biosensors, not just to simplify the assay, but also trying to fulfilling the key requirements like reproducibility, biocompatibility, cost and large scale production capability.

One of the key requirements when constructing a biosensor is to make sure that the biological material is successfully attached to the electrode, a process governed by various interactions between the biological component and the sensor (transducer) interface. Advanced immobilization technologies capable of depositing biologically active material onto or in close proximity of the transducer surface have been reported.[7] Compared to the case where the biomolecule is physically adsorbed (via van der Waals forces, ionic binding or hydrophobic

interactions), the biosensors where the biomolecule is covalently attached to the surface of the transducer provides shorter response time and good stability, especially for long term storage.[7-8] Hence, in all our approaches we generally employ carbodiimide cross-linkers like 1-ethyl-3-(3-dimethylaminopropyl) carbodiimide hydrochloride (EDC) along with *N*-hydrosuccinimide (NHS) as a catalyst, which helps in the formation of more stable complex.[9] EDC reacts with activated carboxyl (-COOH) groups on the transducer and then with the amine group of biomolecule forming a strong amide (-CONH) bond. Several materials (as support) like noble metal nanoparticles, polymers, composites, and carbon based nanomaterials have been extensively employed for biosensing.[10-12] In this regard, the biocompatibility of the electrode material plays a critical role.

Significance

Biosensors find their applications in areas like clinical and non-clinical use, food and poultry industry, and military applications. The major clinical application so far is for blood glucose sensing because of the huge market demand. Biosensors are also popular for non-clinical applications involving environmental monitoring of bioagents like Anthrax, Plaque, etc. Another key application of biosensors is towards developing point-of-care devices, for rapid screening of certain diseases. Early detection and diagnosis has been proved to greatly reduce the direct cost of patient care associated with advanced stages of many diseases. For example, these costs have been estimated to be ı$7 4 billion[13] and $90 billion[14] for cancer and diabetes, respectively. Currently, cancer can be detected by monitoring the concentration of certain antigens or enzymes present in the bloodstream or other bodily fluids, or through tissue examinations. Correspondingly, one can develop a biosensor utilizing specific biomarkers for cancer that can save time and cost of the diagnosis. Despite their widespread clinical use, biosensors have a number of potential limitations hindering their commercial adoption. For example, biofouling and reliable functionalization strategy are some of the issues that are encountered. Therefore, there is a need to develop more efficient and reliable biosensing and detection technologies.

1.2 Traditional detection techniques: merits and limitations

1.2.1 Techniques currently used for pathogen detection

Microscopic, culture, biochemical, immunological, and genetic techniques are various commonly used pathogen detection techniques. Pathogenic bacteria cause variety of diseases

when a human being is infected. Among them, *Escherichia coli* (*E. coli*) is the most common one which can cause urinary infection, sepsis, meningitis, and most commonly, enteric diarrhea. The most devastating serotype, *E. coli* O157:H7 is an enterotoxigenic *E. coli* strain which can cause serious food borne illnesses and death in young children and elders.[15-16] Three major methodologies for pathogen detection are enrichment (a culture technique), enzyme-linked immunoassay (ELISA, an immunological technique), and nucleic acid based molecular detection (a genetic technique).

Cultural methods have been used for over a century, and are still the gold standard for bacterial detection. This method relies on inoculation of the culture medium and then incubating at optimum growth conditions, to allow cell multiplication, which results in a culture of the organism. Cultural characteristics like colony morphology, size, thickness, smoothness, color etc., can then further be used to identify particular bacteria. Since colony morphology alone cannot lead one to identify a bacterium, physiological properties of bacteria like selective media (allowing certain group of bacteria to grow), and metabolic/enzymatic characteristics are used. One of the biggest disadvantage or limitation with culture method is, it is labor intensive, takes approximately 3-7 days to complete the test, and is not suitable for rapid detection of a large number of samples.[17]

Immunoassay techniques are based on the interaction between an antigen (from pathogen) and antibody (human or animal origin), and this technique requires detection or quantification of this interaction. This specific antigen-antibody recognition mechanism has been used to develop several immunological methods for the screening or identification of pathogenic bacteria. ELISA or Enzyme-Immuno Assay (EIA) is the most popular of this category, which has been adopted to detect antigens that originate specifically from the targeted bacterial pathogen. The concept of ELISA is schematically shown in Figure 1.2.[18] Briefly, anti-bacterial antibody is attached to a solid surface, and when bacteria possessing the corresponding antigen are added, they will be captured by the antibody. The second antibody that reacts with another part of bacteria will be added, which is linked to an enzyme that will generate a measureable product when a substrate is added. Related but slightly variant techniques like immunomagnetic separation, lateral flow and latex agglutination method are also used for pathogen detection.[18-20] Immunological assays (especially ELISA), are relatively fast, sensitive, and specific.[17, 21-22] However, the disadvantages include cross-reactivity that can lead to false positive results,

susceptibility to background interference under low microbial population and lack of stable antibodies.[23-24]

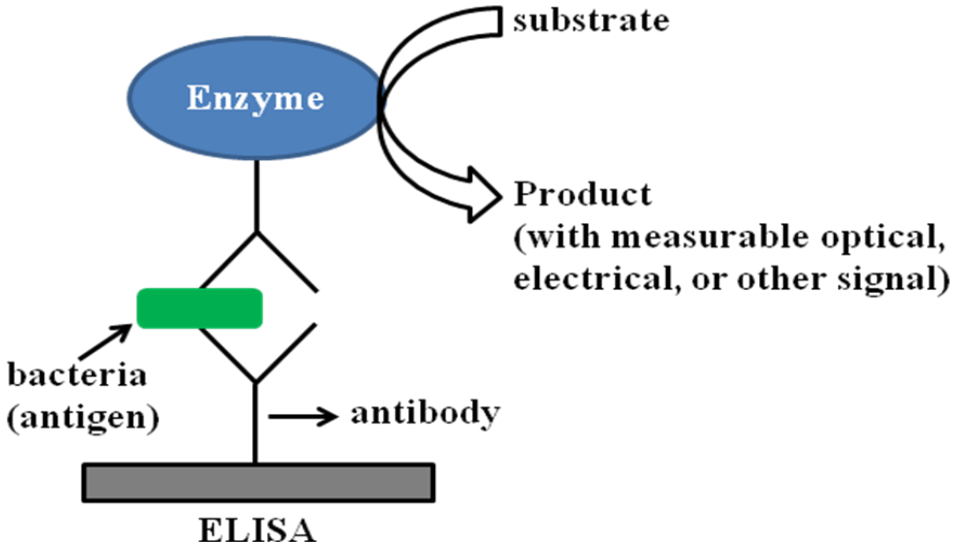

Figure 1.2 Schematic showing the concept of immunoassay technique enzyme-linked immunoassay (ELISA).

Nucleic acid based molecular detection methods can be divided into two major categories: hybridization based microarrays, and polymerase chain reaction (PCR) amplification based detections. Microarray technology was first reported in 1995 by Schena et al.[25], and Lipshutz et al.[26] Microarray refers to a checkerboard-like ordering of probe molecules on a surface. It is equivalent of a spreadsheet (on molecular level), where each cell of the spreadsheet contains a specific probe designed to detect a given target.[27] DNA microarray relies on the hybridization of complementary base-pairs of the probe and target strands. In detection arrays, sequences from multiple closely related pathogens, and in most cases, multiple sequences from a single pathogen are used. The power of microarray for pathogen detection is that through one hybridization, one can detect many pathogens at the same time, as one microarray chip can easily hold tens of thousands of DNA sequences. Disadvantage of using microarray for pathogen detection is that the sensitivity is low, it requires large amount of labeled DNA/RNA, it is expensive, and time consuming.

PCR is a molecular technique relying on in vitro amplification of a DNA fragment via enzymatic replications. Due to its exponential amplification nature, PCR is the most sensitive

detection method.[28-29] In regular PCR, products of PCR amplification (amplicons) are usually separated on agarose gel, stained and the resultant fluorescent DNA bands are detected. Regular PCR only detects after amplification, hence sometimes also referred as end-point PCR. Alternatively, real-time PCR technique allows detection of amplicons while they are formed upon each cycle of amplification, and the amount of input template can be quantified by recording the signal using a camera. Compare to regular PCR, real-time PCR provides higher specificity for the detection, requires smaller amplicon size (75 to 200 base pairs), and reactions can be done very fast, i.e., within an hour, or even shorter. However, this method involves sophisticated instrument, expensive fluorescent dyes and reagents and extensive sample preparation. Also, it restricts for sample analysis in laboratory environment.

1.2.2 Rising issues of blood contamination

Blood-borne contaminants are a major human health threat. Hepatitis is a leading cause of liver disease afflicting humans worldwide. Approximately one third of the world's population is infected with either Hepatitis B or Hepatitis C virus, the two most prevalent forms of hepatitis. Both forms are spreading rapidly. The most prevalent form in the United States, Hepatitis C, has infected at least 150 million people worldwide. One well-documented mechanism of transfer of the Hepatitis C virus from person-to-person is via transfer of serum-tainted materials such as needles and shared intravenous fluids, through improper or inadequate blood handling procedures. Indeed, major outbreaks of Hepatitis and other viral and bacterial infections have resulted from transfer of blood between patients in clinics and hospitals due to inadequate safeguards against reuse of contaminated material. Remarkably, there are no methods currently available that are sufficiently sensitive, rapid, and portable to immediately assess levels of blood and/or viral contamination of common-use materials in these settings. The research work presented in chapter 5 of this thesis details our approach towards developing a novel biosensor which can reliably detect blood which utilizes gold nanoparticles (GNPs) and luminol. We performed some preliminary experiments, the results of which indicate that low levels of DNA or RNA can be detected with our approach.

1.2.3 The luminol test for blood detection

Luminol test is a chemical test used to detect the presence of blood. This method depends on the presence of haemoglobin. Luminol when reacts with appropriate reagents generated blue

colored light. The mechanism of light production is shown in Figure 1.3.[30-34] The chemiluminescence (CL) reaction of luminol generally utilizes Fe^{3+} from heme as a catalyst and requires two equivalents of base to deprotonate the nitrogen protons, leaving a negative charge which then undergoes resonance to form an enolate ion.[30] Then a cyclic addition reaction of the oxygen at the two carbonyl carbons takes place with the oxygen provided by peroxide (with Fe^{3+} catalyzing the breakdown of peroxide into oxygen and water), leading to the expulsion of N_2 in the gaseous form. This step leads to the formation of 3-aminophthalate (an excited form of luminol). Light emission peaked at the wavelength of λ_{max} = 425 nm is generated while electrons return to the ground state.[30-31]

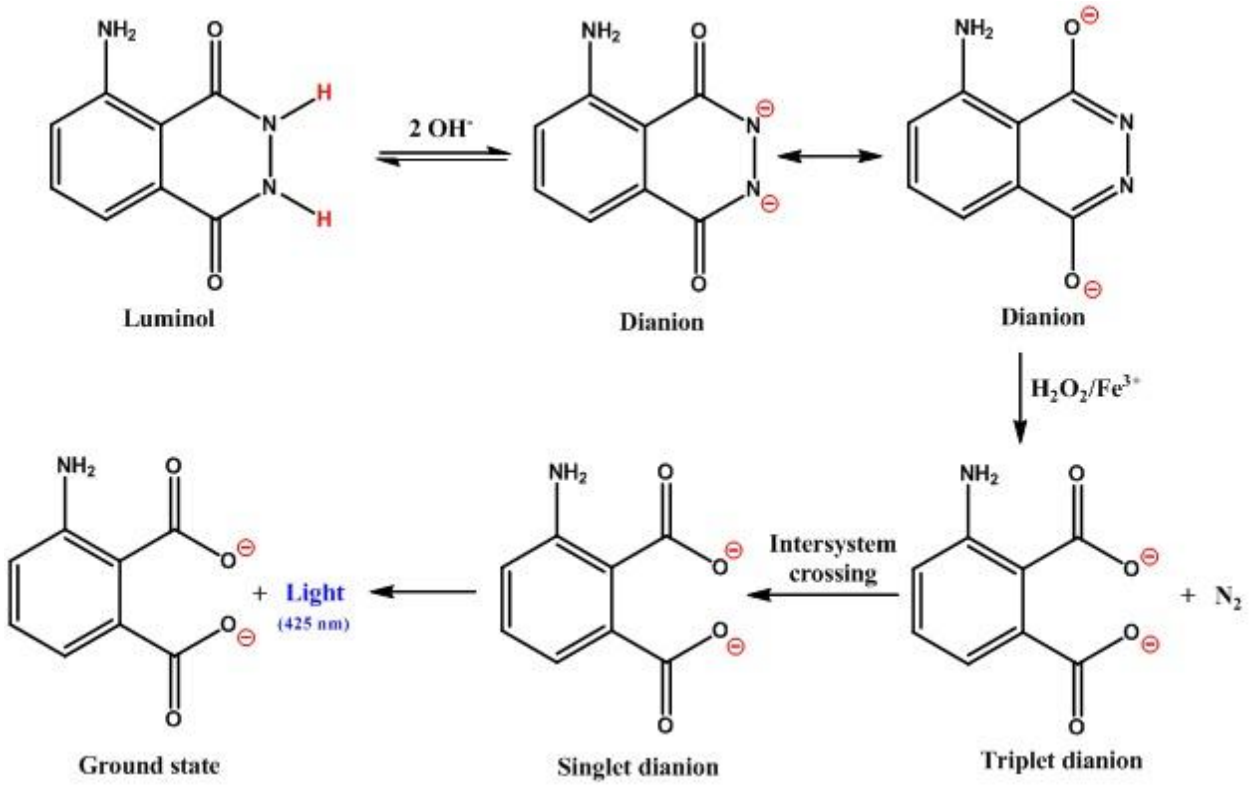

Figure 1.3 The reaction and mechanish involved in the generation of blue colored chemiluminescence by luminol in presence of reagents NaOH, H_2O_2, and Fe^{3+} containing analytes.

1.3 Nanomaterials for biosensing: advantages and challenges

Nanotechnology, the creation of functional materials, devices, and systems through the control of nano scale materials,[35] has recently become one of the most influential fields at the fore front of analytical chemistry.[35-36] In recent years there has been a tremendous growth towards application of nanomaterials in biosensors. Nanomaterials like carbon nanotubes, gold nanoparticles, nano magnetic beads, nanocomposites, and quantum dots in particular, have been widely used for biosensing. The materials mentioned are attractive probe candidates because of their (1) small size (usually 1 to 100 nm) and correspondingly large surface-to-volume ratio, (2) chemically tailorable physical properties, which relate directly to size, composition, and shape (3) unusual target binding properties, (4) over all structural robustness, (5) provide unique optical or electrical properties, and, (6) minimizes surface fouling of the sensing systems.[37]

Improving the current bioanalytical techniques and methodologies and finding novel concepts and applications in bioanalysis are the two areas where more and more nanotechnology and nanoscience studies are focused. Advances in nanotechnology affect existing technologies and lead to the development of novel bioanalytical tools and techniques through improvements in speed of analysis, lower sample requirements, and the ability to perform multiple detections in smaller devices. Novel biosensing systems that require less sample material are being developed so as to perform sophisticated tests at the point of care (for example detection of blood glucose level using a hand held device within fraction of seconds) and make possible the multiplex analysis. *The comparable size of nanomaterials and biomolecules has allowed the integration of biological systems with nanometer sized structures, building novel hybrid nanobiosensors with excellent properties and functions*.[37]

Though nanomaterials proved to be advantageous, in numerous ways for the development of novel hybrid biosensors, they face many challenges. One of the major challenge is to reliably fabricate nanoelectrodes or synthesize nanoparticles, with higher degree of control in physical (size, and morphology), and chemical (type of ligand, and ligand exchange) properties of the nanomaterials. In some cases functionalization may pose a bigger challenge, mostly due to insufficient understanding of the surface chemistry. In this case, it may be necessary to carry out multiple-step reactions to functionalize and also it might be necessary to do passivation of the electrode surface to prevent non-specific adsorptions.

1.4 Nanoelectrode array (NEA) for biosensing

Since Iijima discovered carbon nanotubes (CNTs) in 1991, CNTs have attracted enormous interest due to high electron transfer rate,[38] and high electroactivity.[39-40] CNTs have great potential in applications such as nanoelectronics, biomedical engineering, and biosensing and bioanalysis.[41] It has been reported that CNTs have better compatibility with biomaterials, leading for the development of new carbon based nanoscale devices.[42-43] Several research groups have employed bundles of CNTs,[44-45] CNT membranes,[46] polymer-CNT composites,[47] and CNT-modified electrodes as effective electrochemical biosensors[39, 48-50]. Aligned CNT arrays are also used for RNA, DNA, enzyme, and protein sensing.[48, 51-54] Previously, several research groups have used aligned CNT array to fabricate NEA for several biosensing strategies (including Prof. Jun Li). Some of the key applications employing CNT NEA are discussed below.

1.4.1 Glucose sensing

There is a huge demand for blood glucose monitoring, because of which considerable effort has been made by several researchers to build a reliable glucose biosensor. The measurement principle relies on immobilization of oxidase enzyme to the surface of different electrodes and detect the signal (current) associated with the redox biological reaction. Selectivity and sensitivity can be usually enhanced by using artificial mediators and selective membranes. A mediator and membrane free strategy was then reported by Lin et al.[55] using low site density CNT NEA for glucose detection.

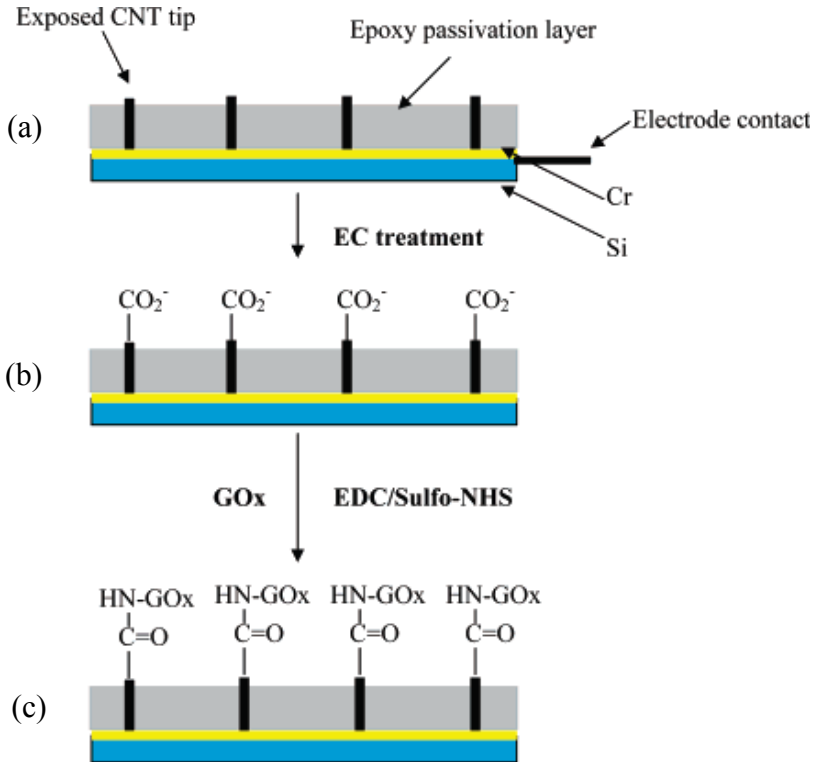

Figure 1.4 Glucose biosensor based on CNT NEAs. (a) Embedded CNT NEA with exposed CNT tips. (b) Electrochemical treatment of the CNT NEAs for functionalization. (c) Coupling of the enzyme (GO*x*) to the CNT NEAs. (Adapted with permission from ref. 55. Copyright © 2004, American Chemical Society.)

A low density CNT NEA embedded in a polymer (epoxy) matrix with only the very end tips exposed was used. The CNT NEA was then electrochemically treated in 1.0 M NaOH at 1.5 V for 90 s to generate carboxyl functional groups at the exposed tips. Then enzyme glucose oxidase (GO*x*) was functionalized with the assistance of 10 mg/ml aqueous solution of EDC and NHS. The electrochemical (amperometric) experiments were performed in a standard 3-electrode set-up, where NEA serves as working electrode (WE), Ag/AgCl as reference electrode (RE), and a platinum wire as auxiliary or counter electrode (CE). Amperometric signal for the calibration plot was recorded under steady-state conditions in a 0.1 M phosphate buffer (pH 7.4) by applying a potential of -0.2 V to the WE. Amperometric response at the NEA glucose biosensor was measured by adding 2 mM glucose solution. The response upon successive addition of glucose solution is shown in Figure 1.5. The inset shows the calibration plot. The linear response

of the current signal was observed up to 30 mM glucose concentration, higher than the value (15 mM) required for practical usage.

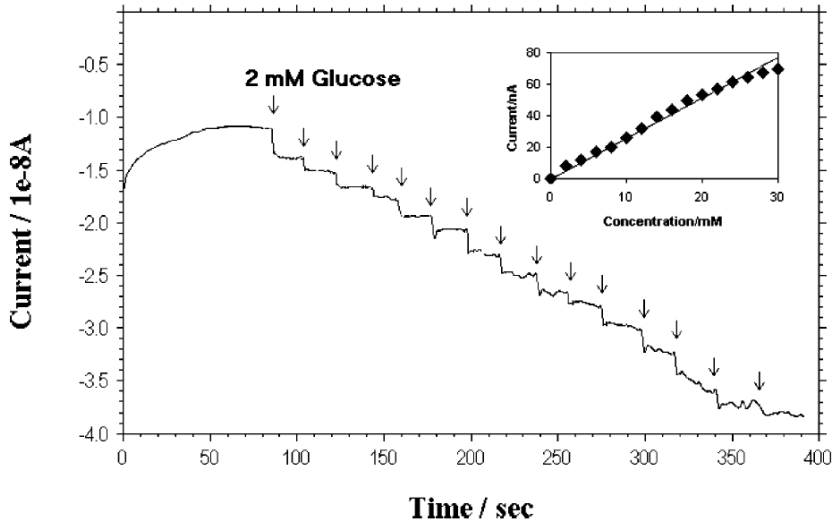

Figure 1.5 Amperometric response of a CNT NEA biosensor to successive additions of 2 mM glucose. (Adapted with permission from ref. 55. Copyright © 2004, American Chemical Society.)

1.4.2 DNA sensing

Functionalized CNTs and carbon nanofibers (CNFs) with a specific probe of DNA have been employed as DNA sensors (see Figure 1.6a).[56-59] Each individual CNT acts like an individual nanoelectrode and the smaller diameter (10-100 nm) is close to the size of DNAs which makes the CNT NEAs very sensitive. For example, Li et al.[57, 60] and Koehne et al.[51-52, 58] have demonstrated ultrasensitive DNA detection using CNT NEA based on mediator amplified guanine oxidation, as shown in Figure 1.6b. DNA probe was directly attached to the exposed CNT tips by forming an amide bond using EDC and NHS. Extremely high sensitivities were achieved, with a CNF NEA on a 20 x 20 μm^2 microcontact, an estimated <1000 hybridized targets could be easily detected.

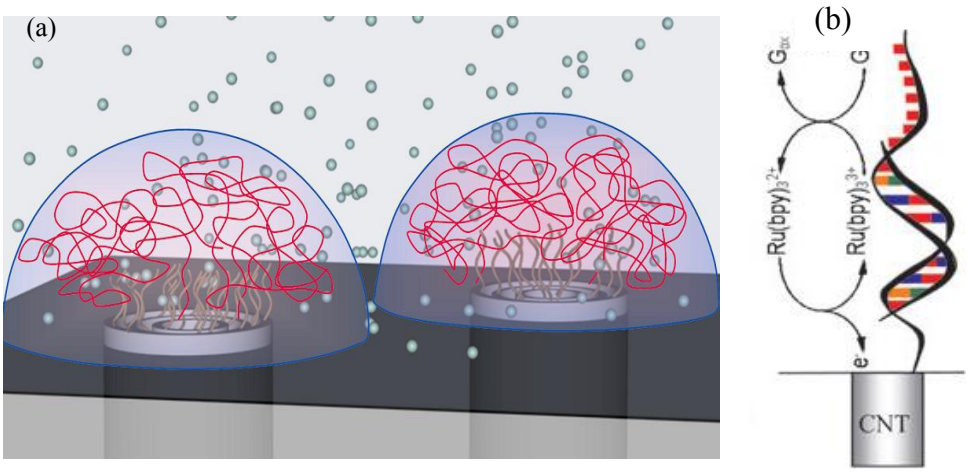

Figure 1.6 Schematic of NEA for ultrasensitive DNA detection based on mediator-amplified guanine oxidation. (a: Adapted with permission from ref. 51. Copyright © 2003, IOP Publishing Ltd; b: Adapted with permission from ref. 57. Copyright © 2003, American Chemical Society.)

Figure 1.7a shows SEM images of a DNA sensor consisting of a 3 x 3 array of individually addresses CNT electrodes on a silicon wafer covered with a 500 nm thick thermal oxide. The electrodes and contact lines are 200 nm thick Cr patterned with UV-lithography. Each electrode can be varied from 2 x 2 to 200 x 200 μm^2 (Figure 1.7b), consisting of a vertically aligned multi walled CNT (MWCNT) array grown by plasma enhanced chemical vapor deposition (PECVD) from 10 to 20 nm thick Ni catalyst films. Figure 1.7c and Figure 1.7d shows MWCNT arrays grown on 2 μm and 200 nm diameter Ni catalytic spots prepared by UV and e-beam lithography, respectively. The spacing and spot size can be precisely controlled in both the techniques while designing the masks. The diameters of the MWCNTs can be controlled between 30 and 100 nm during the PECVD growth process. Also, the density of the CNTs at each spot can be varied by changing the thickness of the Ni film. A tetraethoxysilane (TEOS) chemical vapor deposition (CVD) process is employed to encapsulate each CNT and the substrate surface with a conformal SiO_2 film. This is then mechanically polished to planarize and expose the tips of the CNTs. Figure 1.7e and Figure 1.7f shows the embedded CNT array with different patterns after polishing. The aligned MWCNT NEAs shown in Figure 1.7 can detect DNA down to few attomoles providing faster, cheaper, and simpler solutions for molecular diagnosis particularly for early cancer detection, point-of care uses.

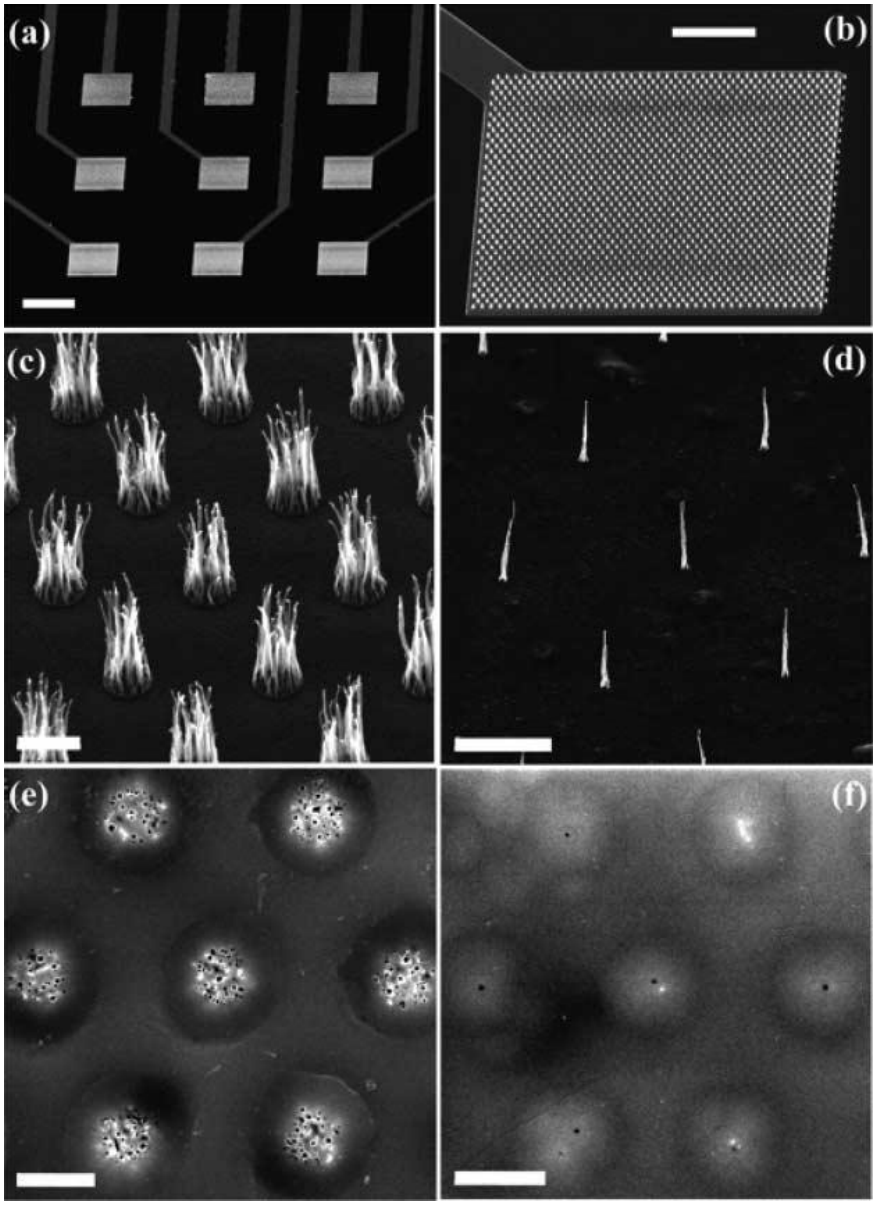

Figure 1.7 SEM images of (a) 3 x 3 CNF electrode arrays. (b) Arrays of MWCNT bundles on one of the electrode pads. (c, d) Array of MWCNTs grown from UV-lithography and e-beam patterned Ni catalytic spots, respectively. (e, f) Surface of polished MWCNT electrode arrays grown on 2 μm and 200 nm catalytic spots, respectively. Panels (a-d) are 45^{o} perspective views and panels (e and f) are top views. Scale bars: (a) 200 μm, (b) 50 μm, (c) 2 μm, (d) 5 μm, (e) 2 μm, and (f) 2 μm. (Adapted with permission from ref. 57. Copyright © 2003, American Chemical Society.)

1.4.3 Importance of rapid bacteria detection

As discussed above (in section 1.2.1), the gold standard traditional cultural bacterial identification methods are too laborious and time consuming. Immunological methods though widely used they suffer from sensitivity and specificity issues. Microarray, a molecular detection technique is a very powerful tool, but it is very expensive, time consuming, and not very sensitive. So far, PCR-based methods are most promising as they are very sensitive, can be multiplexed, and very reliable. However, PCR reactions require a special machine, thus is not portable, most procedures takes 1-2 hours, pre-PCR sample preparations also takes times. The research work presented in chapter 4 of this thesis explores the possibility of developing a label-free electronic detection of pathogens. The concept relies on using NEAs (see Figure 2.1), and we demonstrate that we can successfully manipulate single *E. coli* cell electronically. NEA consists of millions of VACNFs, free standing on Si substrate and embedded in SiO_2 (see Figure 2.1). Electronic techniques have been long recognized for their potential in quick biomolecular analysis.[61-62] Individually addressed microelectrode arrays (MEAs) have been commercialized for molecular diagnosis.[63-67] Microelectrodes in interdigitated arrays (IDAs)[68-70] or other configurations[71] have also been used for capture and manipulation of cells or charged biomolecules using electrical forces. Though it has not been realized yet, the sample preparation and sensing microdevices can be integrated through microfluidic interconnects into a single chip for highly miniaturized and automated multiplex detection. The concept of electronic biochips is attractive for point-of-care and field-deployable portable systems.

1.5 Nanoparticles based biosensing

Nanoparticles, with sizes falling in the range 1 to100 nm, behave differently from bulk materials with respect to their physical, chemical, and electronic properties. This can be associated with unusual phenomena such as quantum size effects, surface effects and macro-quantum tunneling effects.[72] Further, it is observed that the unique catalytic properties offered by such nanomaterials can lead to substantial signal amplification for the transduction of biomolecular recognition event of a biosensor.[73] Therefore, with the integration of nanoparticles in to their construction, the analytical performance of biosensors has shown remarkable improvement. The use of nanoparticles has also facilitated the effective utilization of existing detection methods and provided many new signal transduction schemes, with excellent

sensitivity, high selectivity, and long-term stability. The research work discussed in chapter 5 of this thesis utilizes gold nanoparticles (~8-12 nm) to build biosensor for the detection of blood. Let us look at some of the studies done by other researchers, who utilized GNPs for various biosensing applications.

1.5.1 Gold nanoparticles based biosensors

Gold nanoparticles (GNPs) show strong absorption in the visible region due to a phenomenon termed as surface plasmon resonance (SPR). SPR is the collective oscillation of conduction band electrons with visible frequencies of light within metal nanoparticles. When the size of the nanoparticle is much smaller than the wavelength of incident light, at any given point the nanoparticle experiences a relatively uniform electric field. This "uniform" electric field pushes the electrons all together to one side of the particle. The movement of conduction electrons upon light excitation leads to a buildup of polarization charges on the particles surface which acts as a restoring force, allowing a resonance to occur at a particular frequency, which is known as the SPR frequency.[74-75] Factors such as size, shape, surface charge, and the dielectric constant of the surrounding medium influence the SPR frequency. It is well known that well dispersed GNPs display different color at different size, as shown in Figure 1.8.[76] Colloidal gold of different shape and size displays different color due to the dependence of absorption at different wavelengths. For example, larger and asymmetric GNPs absorb longer wavelengths whereas the smaller and spherical GNPs absorb shorter wavelengths.

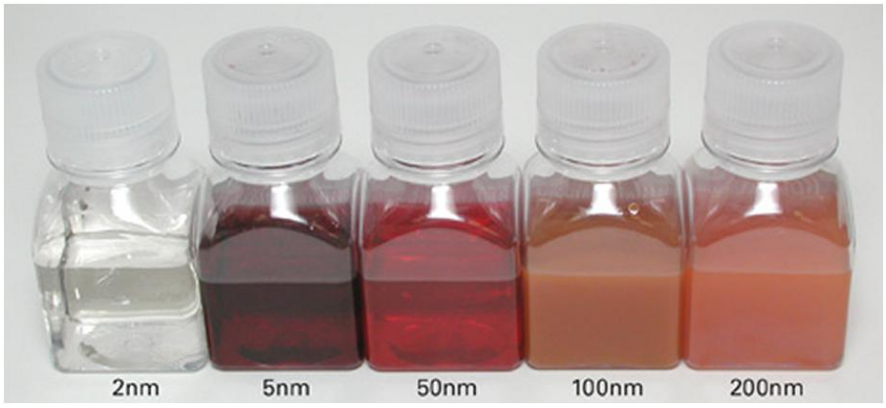

Figure 1.8 Nanometersized monodispersed gold colloids of different sizes in water, with trace amounts of citrate, tannic acid and potassium carbonate (http://www.tedpella.com/gold_html/goldsols.htm).

GNPs based colorimetric biosensors

On one hand the well-dispersed GNPs display red color (5-100 nm), but on the other hand aggregate GNPs appear blue in color. Taking this phenomenon as the base, along with some other minor strategies, several facile GNP-based colorimetric biosensors have been developed.[77-78] By merely looking at the change in the color by naked eye or by measuring the UV-visible absorbance of the solution one can predict the presence or absence of a particular analyte. For example, Jena et al.[79] developed a GNP-based biosensor to quantitatively determine the polyionic drugs such as protamine and heparin as shown in Figure 1.9.

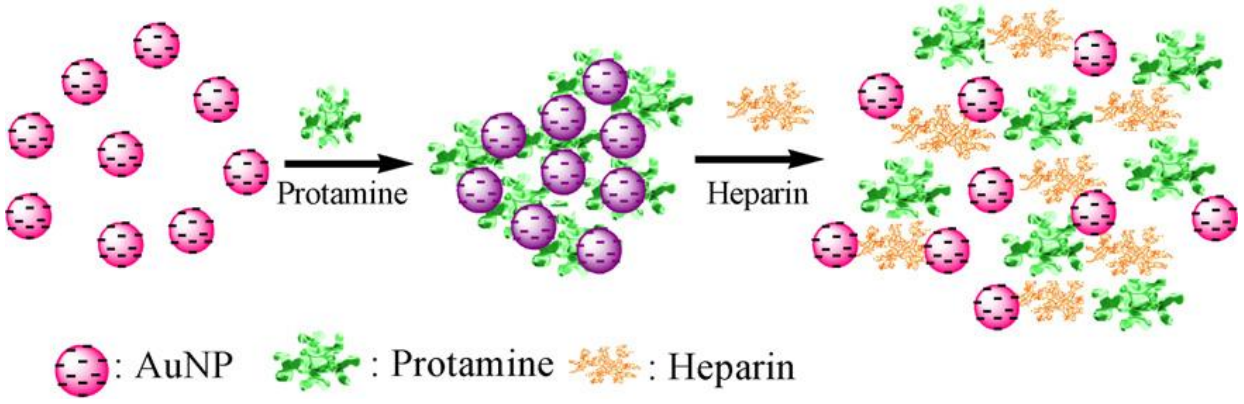

Figure 1.9 Schematic showing protamine-induced aggregation of gold nanoparticles and heparin driven de-aggregation of gold nanoparticles. (Adapted with permission from ref. 79. Copyright © 2007, with permission from Elsevier.)

Figure 1.9 illustrates the reversible aggregation/de-aggregation concept used for the sensing of polyionic drugs, protamine and heparin. In this study, citrate stabilized GNPs (5 nm) were synthesized in-house using standard sodium boron hydride ($NaBH_4$) reduction method. Protamine aggregation experiments were done by gradually adding fixed volume of certain concentration protamine to the native GNP solution, and the absorption spectra was recorded after each addition. All experiments were carried out in both de-ionized water (pH 6.8) and PBS (pH 7.4), and in both the cases the results were the same.

The as-synthesized GNP colloidal solution displays an intense SPR absorption (see curve a in Figure 1.10) in the visible region of the electromagnetic spectrum, giving red color to the GNP solution. Once the protamine solution is added aggregation GNPs occurs, which results in change of color from red to blue. This is also evident by the red shift in the absorption curves

from 514 nm to 550 nm, as shown in curves b and c in Figure 1.10. The color change can be readily reversed from blue to red by de-aggregating the GNPs by using a suitable reagent, which in this case is heparin. The absorption curve was blue shifted when heparin was added to the protamine-GNP mixture (curve d in Figure 1.10).

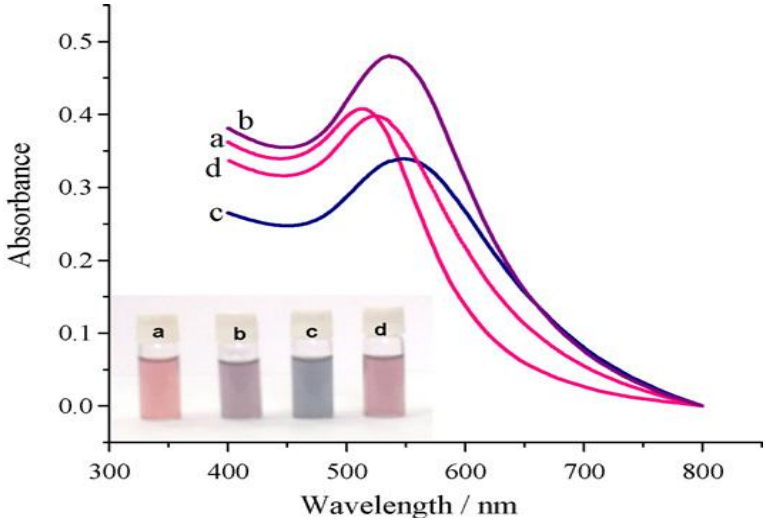

Figure 1.10 Absorption spectra illustrating the protamine-induced aggregation and heparin-driven de-aggregation of GNPs. (a) GNPs alone, (b, c) after the addition of protamine 0.7 µg/ml (b) and 1.6 µg/ml (c), (d) after the addition of heparin (10.2 µg/ml). Inset shows the corresponding colorimetric response. (Adapted with permission from ref. 79. Copyright © 2007, with permission from Elsevier.)

Another interesting approach is to covalently attach a specific sequence of DNA (probe) to the GNPs and then perform hybridization with the target on the lateral flow strips (as shown in Figure 1.11). When the GNP-probes are captured at the test zone and control zone of the biosensor, characteristic red bands can be observed enabling one to visually detect DNA, which can be further quantified by measuring the intensities with a portable strip reader.

Based on this concept, Mao et al.[80] successfully developed a rapid, and sensitive disposable nucleic acid biosensor (DNAB). The biosensors response was linear over the range of 1-100 nM target DNA under optimum conditions and under enhanced conditions the biosensor was capable of detecting minimum of 50 pM target DNA. However, the colorimetry based detection requires that there are sufficient GNPs, i.e. the number of GNPs required for reliable detection is usually large. In other words, we need more probe labeled GNPs at the test and

control zone. We address this issue in chapter 5, where we demonstrate that this problem can be overcome with a more sensitive chemiluminescent method.

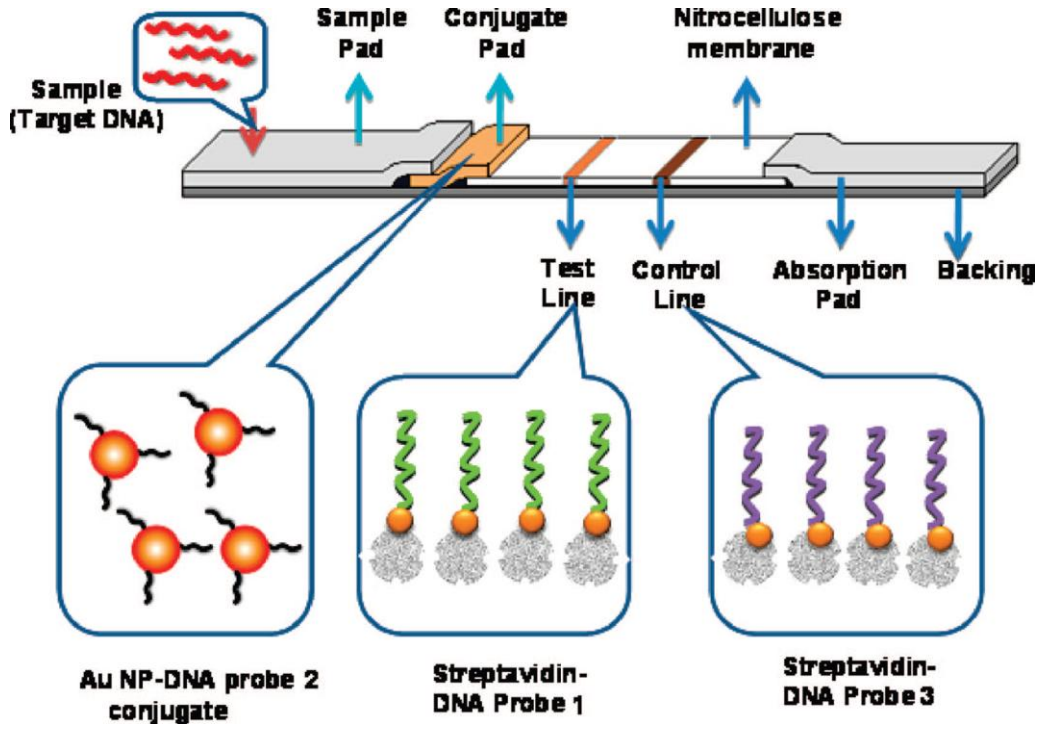

Figure 1.11 Schematic illustration of the disposable lateral flow nucleic acid biosensor based on gold nanoparticles labeled with probes. (Adapted with permission from ref. 80. Copyright © 2009, American Chemical Society.)

1.6 Dissertation outline

The dissertation comprises of the following major sections:

Chapter 1 – gives a brief introduction about the concept of biosensors and role of nanotechnology for the development of high performance biosensors. Following which some of the current approaches by researchers using NEAs and NPs for various biosensing applications is discussed. This forms the basis and motivation to use NEAs and GNPs for biosensing.

Chapter 2 – explains a brief procedure and experimental details about the fabrication of NEA, which is followed by the details of materials and methods used for the research work

presented in chapter 2 and chapter 3. At the end of this chapter, electrochemical characterization of macro glassy carbon electrode (GCEs) and NEAs is discussed.

Chapter 3 – an accepted paper, published in *Electroanalysis*.[81] This chapter describes an extensive electrochemical study done on NEAs to address the issue of slow electron transfer rate offered compared to the GCEs by NEAs when we use DC voltammetry. It also discusses on how to overcome this issue by using AC voltammetry instead of DC voltammetry. With our results we prove that if appropriate electrochemical technique is used NEA may prove to be advantageous, especially for the development high performance biosensors for cancerous protease detection.

Chapter 4 – an accepted paper, published in *Electrophoresis*.[82] This study is about using NEA for electronic manipulation of pathogens and measuring impedance change at the NEAs. To achieve this goal, a microfluidic device was constructed using UV-photolithography. After a reliable device fabrication method was established, that device was used to electronically capture pathogenic *E. coli* cells using a phenomenon called dielectrophoresis. Also, change in the impedance at the NEA was recorded during the capture and release of *E. coli*.

Chapter 5 – provisional patent application has been filed and manuscript in preparation. In this study we explore the possibility of using modified GNPs for different applications like blood, and DNA (future study) detection. GNPs were functionalized with luminol, which when reacts with appropriate reagents and blood as a catalyst will generate CL signal. A detailed optimized procedure for the functionalization, and then the characterization of GNPs at different steps is given. This chapter also discusses the results of lysed and unlysed sheep blood detection. Also, towards its use for DNA biosensing we discuss key preliminary results.

Finally, Chapter 6 summarizes the major findings of this work and explains the future research directions.

Chapter 2 - Fabrication and Characterization of Vertically Aligned Carbon Nanofiber (VACNF) NEA

Reproduced in part by permission of the John Wiley and Sons.

Published as: Syed, L. U.; Liu, J.; Prior, A. M.; Hua, D. H.; Li, J. *Electroanalysis* **2011,** *23*, 1709-1717.

2.1 Introduction

CNFs are a subgroup of MWCNTs, which are grown by PECVD.[20, 83-84] Though CNFs and MWCNTs share some common properties such as high aspect ratio, superior mechanical strength, and high electrical conductivity along the axial direction, it is noteworthy that PECVD process produces conical graphitic layers stacked on top of each other forming bamboo-like structure as shown in Figure 2.1.[20, 85] It is well known that there are several advantages offered by nanoelectrodes (NEs) in the NEA (Figure 2.1) form for sensitive electroanalytical applications.[86-89] But the development in this area has been limited because of the difficulties involved in the fabrication procedure. So far, Prof. Jun Li's group has demonstrated a reliable means to fabricate randomly grown free standing VACNF NEA embedded in dielectric silicon dioxide (SiO_2).[51-52, 57-58, 81-82, 90]

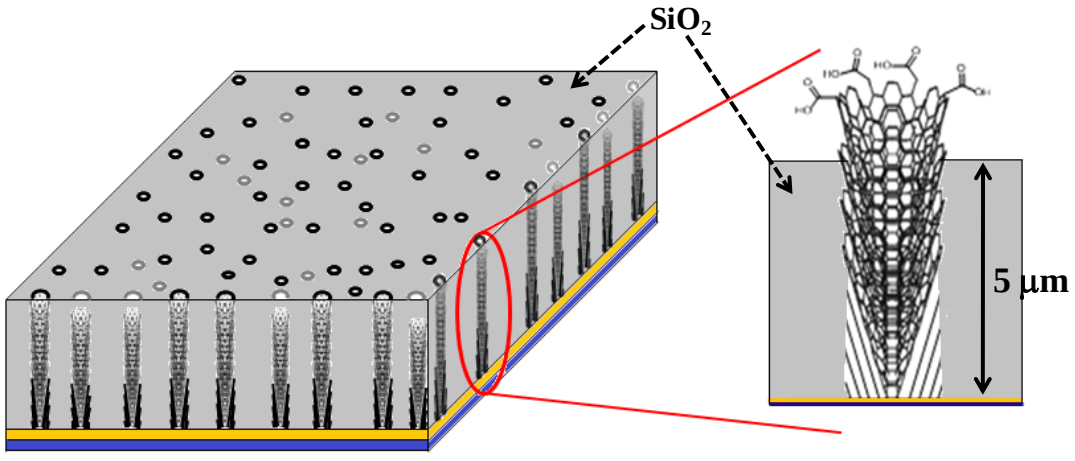

Figure 2.1 Schematic of nanoelectrode array fabricated with vertically aligned carbon nanofibers (VACNFs) embedded in SiO_2 matrix. The dark black colored circle indicates it is the tip of the exposed CNF, and the grey circle indicates unexposed CNF.

2.2 Fabrication of NEA

Fabrication of CNF NEA involves four major steps: (1) Contact metal (chromium, Cr) and catalyst (nickel, Ni) deposition on a silicon (Si) (100) substrate, (2) PECVD based growth of vertically aligned CNFs, (3) SiO_2 encapsulation, (4) planarizing and reactive ion etching (RIE) to expose the tips of embedded CNFs. The sequence of steps involved in fabrication process is shown in Figure 2.2a. The experimental details of each step are discussed below.

2.2.1 Contact metal and catalyst deposition

The first step in the fabrication process is sputter coating a 1 cm × 2 cm Si substrate with Cr and Ni. This is accomplished with a Gatan ion beam sputter coater. Clean Si substrate is coated with 100 nm of Cr and 22.5 nm of Ni using an ion beam with energy of 10.0 keV. During the deposition the sample is rotated at 35 rpm, tilted at 5^o and rocked at a rate of 12 ^{o}/s. This produces a coating rate of 1.2 Å/s for Cr and 0.6 Å/s for Ni. Cr acts a common metal contact layer which connects millions of NEs and Ni acts as a catalyst for the growth of CNFs.

2.2.2 Plasma enhanced chemical vapor deposition (PECVD) for VACNF growth

After the metals are deposited, forest like VACNFs can be grown on the coated silicon wafer using a custom made Aixtron Black Magic PECVD system. First, the Ni catalyst coated in the previous step is annealed at 500 ^{o}C for 60s in the vacuum with a base pressure of ~0.11 mbar. Then, the wafer is exposed to acetylene (C_2H_2) and ammonia (NH_3) with flow rates of 63 and 250 sccm, respectively and 5.48 mbar processing pressure. The sample is then heated to 800 ^{o}C while the DC plasma is started (520 V and 40 W drive). At this temperature and plasma conditions, a 20 min deposition yields a VACNF array with fiber diameters of 50–100 nm and lengths of ~5 μm, as verified by SEM (Figure 2.2b). Each CNF is vertically aligned and freestanding on the surface of Si substrate.

2.2.3 Silicon dioxide (SiO_2) encapsulation

In order to provide mechanical stability to the array and to insulate the bottom Cr layer, and CNFs, the as-grown CNF substrate is coated with SiO_2 using CVD system in a home built tube furnace from Thermo Electron Corporation. After evacuating the chamber to a base pressure of <100 mTorr, the chamber (with as-grown CNF chip) is heated to 730 ^{o}C. Tetraethyl orthosilicate (TEOS, a precursor for SiO_2) is then deposited at a vapor pressure of ~350 mTorr

for 4 hrs and ~400 mTorr for 3 hrs. SiO_2 forms a conformal film, filling the free space between the individual fibers as well as the substrate. A 7 hr deposition ensures complete coverage of the CNFs, as confirmed by SEM (Figure 2.2c).

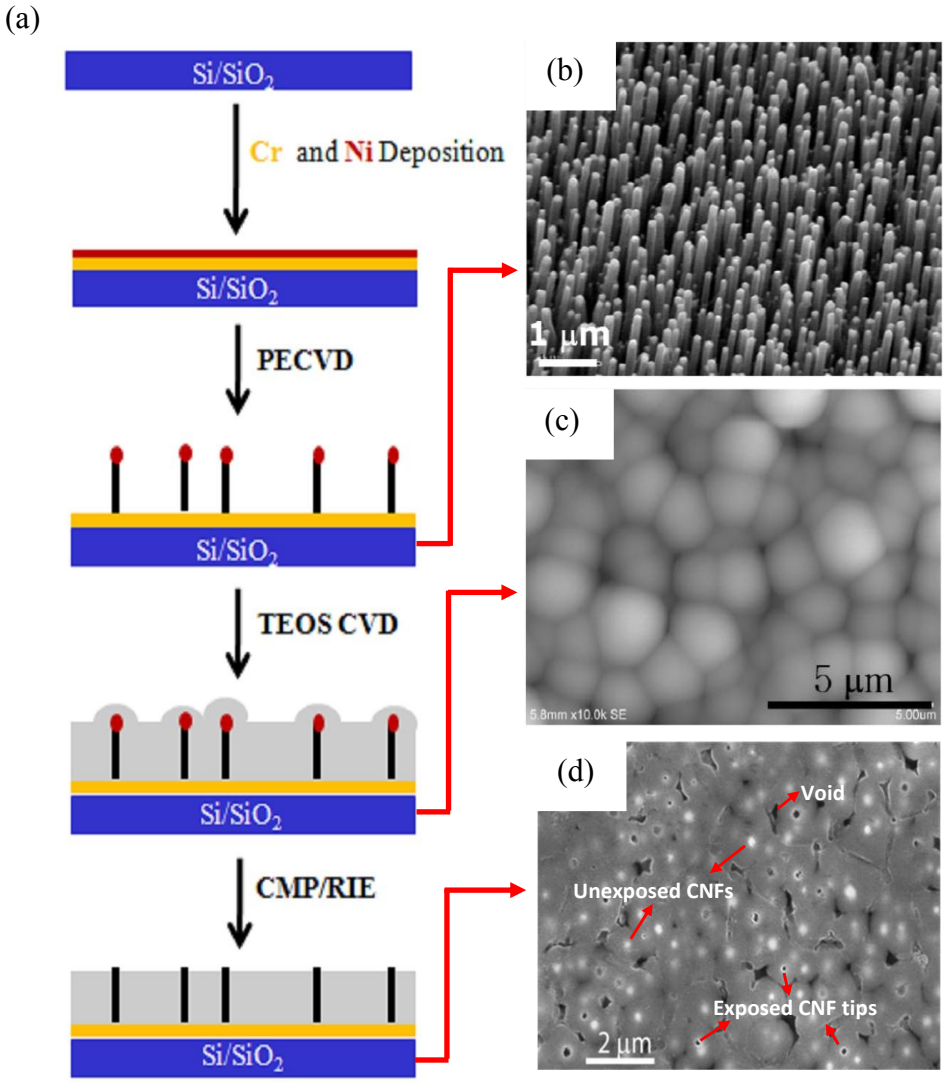

Figure 2.2 (a) Different steps involved in the fabrication process of VACNF NEA fabrication are shown in sequential manner. (b) SEM image of freestanding as-grown vertically aligned CNFs (45° view) after PECVD. (c) SEM image (top-down view) of CNFs after being encapsulated with SiO_2 using TEOS-CVD. (d) SEM image (top-down view) of the surface of an embedded CNF NEA after reactive ion etching and mechanical polishing with arrows indicating different features, and the diameter of exposed CNF is ~100-150 nm. The scale bars for (b), (c), and (d) are 1, 5, 2 µm respectively.

2.2.4 Planarization and reactive ion etching (RIE)

The excess SiO_2 and part of the CNFs were removed by the combination of mechanical polishing to planarize the substrate and RIE techniques. Planarization was done manually using 0.3 μm Alpha micropolish alumina (Buehler, Lake Bluff, IL) for 2 hrs to planarize the surface. RIE (Nano-Master, NRE3000) was then used to etch away SiO_2 from top and expose the tips of CNFs (see Figure 2.2d). Oxygen (10 sccm) and CHF_3 (2 sccm) gases at 200 W and 250 mTorr were used to etch the dielectric. The density of exposed CNF tips can be easily controlled by the etching time. Electrical resistance at the surface of the NEA chip was measured using two point probes of a hand held multimeter to monitor the progress of the etching and the number of exposed CNFs. After RIE, a planarization step was performed using 0.05 μm Alpha micropolish alumina to remove the debris from NEA chip. Routine practice is to repeat the polishing/etching procedure with the NEA chip until the resistance measured using multimeter is between 500-1000 Ω.

2.3 General experimental details for chapter 2 and chapter 3

2.3.1 Materials

The following reagents were used as received: EDC, NHS, sodium hydroxide, potassium chloride (all from Fisher Scientific, Inc) and potassium ferrocyanide (Acros Organics). Aminomethylferrocene ($FcCH_2NH_2$) was prepared by a modification of the reported procedure[91] from the treatment of ferrocenecarboxaldehyde with hydroxylamine and sodium acetate trihydrate in refluxing ethanol and water for 6 h followed by reduction of the resulting oxime (a mixture of cis- and trans-isomers) with lithium aluminum hydride by refluxing in tetrahydrofuran for 2 h. All solutions were made using 18.2 MΩ-cm resistivity deionized (DI) water.

2.3.2 Preparation of Fc-CH_2-NH_2 modified glassy carbon electrode (GCE) and NEA

The WE, which in most of the case is either commercial macro GCE or CNF NEA was first electrochemically etched in 1 M NaOH to introduce carboxylic groups. This helps to selectively functionalize Fc moiety Fc-CH_2-NH_2 by forming an amide bond facilitated by EDC and NHS. Functionalization was done in two steps. In the first step both GCE electrode and NEA were incubated for 2 hrs at room temperature (RT) in aqueous solution of 1.0 mM EDC and NHS, and rinsed with DI water. In the second step, electrodes were incubated with ethanolic

solution of 1.0 mM Fc-CH_2-NH_2 for ~16 hrs at RT. After the incubation, both electrodes were rinsed with ethanol and then dried in a stream of N_2.

2.3.3 Electrochemical measurements

Electrochemical experiments including direct current (DC) cyclic voltammetry (CV), alternating current (AC) voltammetry (ACV) were done using CHI440A (CH Instruments) and electrochemical impedance spectroscopy (EIS) was performed using PARSTAT 2273 (Princeton Applied Research) in a standard 3-electrode set-up using a Teflon cell with a 3 mm diameter O-ring which makes seal with working electrode (WE). A typical electrochemical experimental set-up is shown in Figure 2.3. GCE or NEA serves as WE, Pt wire as CE and Ag/AgCl (sat'd KCl) as RE.

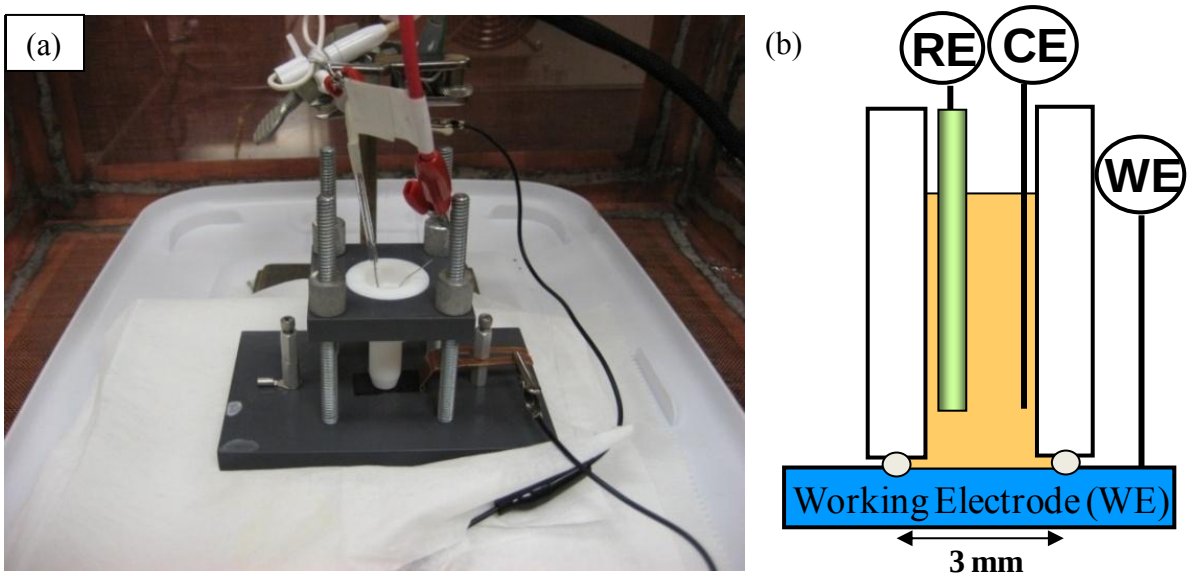

Figure 2.3 (a) Shows 3-electrode set-up using a teflon cell with working electrode at the bottom. (b) Cross-sectional schematic of the same cell is shown.

DC CV of redox species in bulk solution

CV experiments with redox species in bulk solution were performed to characterize the electrochemical behavior of the CNF NEA using 1 mM $K_4Fe(CN)_6$ in 1.0 M KCl solution. CV was recorded by ramping the potential (of the WE) from -0.25 to +0.75 V (vs RE) at different scan rates and the resultant current is plotted vs. potential.

DC CV of surface-attached redox species

After functionalization of GCE and NEA with Fc-CH_2-NH_2, CV experiments were carried out in 1.0 M KCl solution (i.e. without any electroactive species in solution) and potential at the WE was ramped from -0.05 to +0.65 V at different scan rates and the resultant current is plotted vs potential.

ACV experiments

ACV experiments were carried out before and after functionalization in 1.0 M KCl solution. The electrode potential (DC) was ramped from -0.05 to +0.65 V at a scan rate of 10 mV/s and an AC voltage with an amplitude of 25 mV was applied to the DC potential ramp (as shown in Figure 2.4).

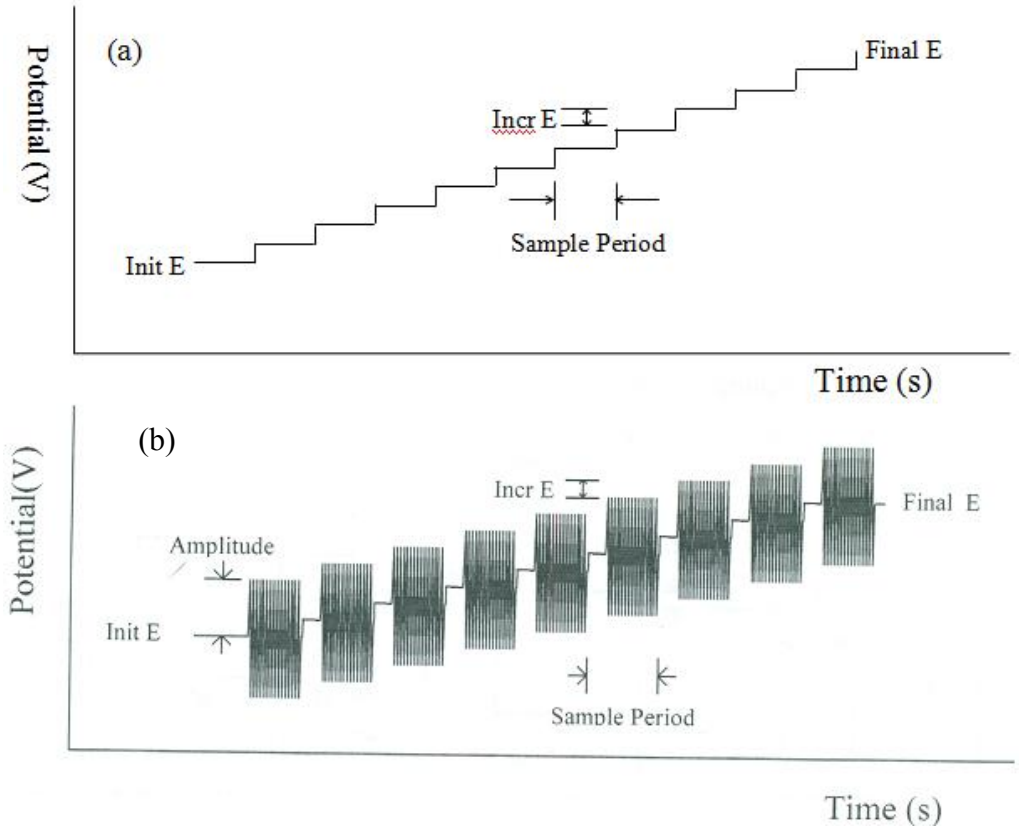

Figure 2.4 (a) The waveform of the staircase DC potential ramp; (b) Schematic of the AC sinusoidal wave of certain amplitude and frequency superimposed on the staircase DC potential ramp (adapted from CHI440A user manual at Li Lab).

The AC frequency was varied from 10-10,000 Hz. The electrode potential was varied as a staircase waveform from the initial potential (-0.05 V) to the final potential (+0.65 V) with an increment of 5 mV at each step. The step width (i.e. Sample Period) was fixed at 0.5 s. The AC sinewave of 25 mV amplitude was superimposed on the DC staircase ramp and the phase-sensitive response of AC signals (current and phase angles) were recorded. The resultant amplitude of the AC current was plotted vs. the electrode potential at each step as AC voltammogram.

Electrochemical impedance spectroscopy (EIS) experiments

EIS is also called AC impedance spectroscopy. In this technique, we apply a potential perturbation (usually a sine wave) and observe the current response, which is also a sine wave of the same frequency, but with a different amplitude and phase than the applied potential wave (as shown in Figure 2.5). During this process, the impedance of a cell or electrode is continuously measured as a function of frequency. In contrast to the techniques like CV, where a large perturbation is used to drive the electrode reaction, EIS uses small AC excitation signal (usually 5-25 mV_{pp}) to study the behavior of an electrochemical set-up. EIS has been very commonly employed by researchers to understand the underlying electron transfer mechanism, both in aqueous and organic mediums.[92-94] For the research work that is described in this thesis, EIS has been used mainly for two purposes, 1) to understand the mechanism of electron transfer phenomenon at the NEA and GCE functionalized with redox functional moiety, and 2) to measure the change in the net impedance value after a pathogen has been captured using a phenomenon called dielectrophoresis.

The impedance (Z) of an electrochemical system can be measured by applying a sinusoidal potential over a large frequency range (1 MHz to 1 mHz) of small sinusoidal potential $E = E_0 \sin(\omega t)$. The resultant current will also be a sine wave with a phase shift of φ and a value $I = I_0 \sin(\omega t+\varphi)$. The ratio of the amplitude of the applied voltage and resulting current in an ac circuit is known as impedance ($Z_0 = E_0/I_0$), which is a frequency-dependent quantity consisting of a real part (Z_{Re}) and an imaginary part (Z_{Im}) as given by the Equation 2.1.

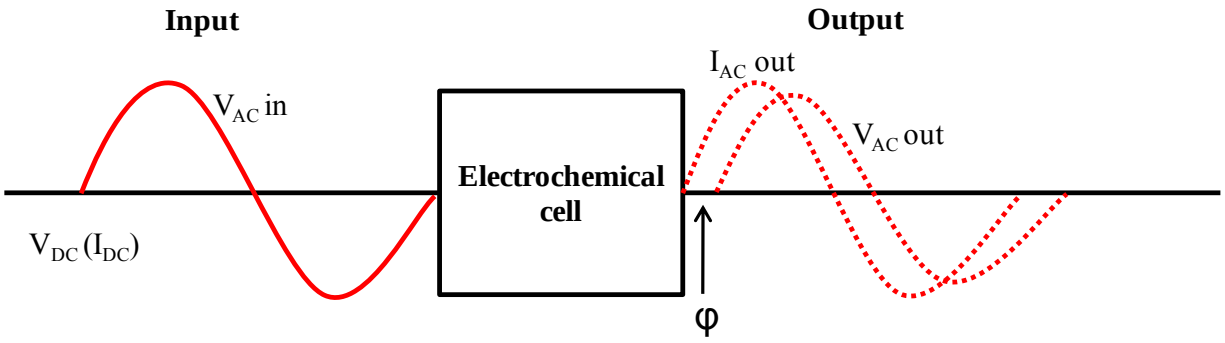

Figure 2.5 Principle of electrochemical impedance spectroscopy. The electrochemical cell is excited by an sinewave of AC voltage and the resultant output AC current is obtained.

$$Z(\omega) = Z_{Re} - j\, Z_{Im} = Z_0 \cos\varphi - j\, Z_0 \sin\varphi \qquad \textbf{(2.1)}$$

Commonly, EIS data is plotted as a Nyquist plot (the imaginary impedance vs. real impedance at discrete frequencies) or Bode plots (the absolute impedance or phase vs. logarithm of frequency). The EIS is usually modeled with an equivalent circuit which mainly contains 4 major components, resistor (R), capacitor (C), constant phase element (CPE) and warburg impedance (Z_w). When a sinusoidal potential is applied through a pure resistor with a value of R, it will result in an impedance value equal to the resistance of R, and a phase shift 0 at all frequencies. This indicates that a pure resistor will not have an imaginary part, thus the current resulting through the resistor will be in phase with the applied voltage across the resistor. When a pure capacitor is used in place of resistor, the resulting impedance is equal to 1/ jωC and the phase angle will be -90° (-π/2). Unlike a resistor, a capacitor will have only an imaginary component. It is dependent on frequency and the output current through the capacitor is phase shifted by -90° with respect to the applied voltage.

EIS experiments were performed in 1 M KCl solution by applying an AC amplitude 20 mV and frequency scanned from 100 kHz to 100 mHz. During the EIS measurement, the working electrode was held at a DC bias of +0.275 V (vs. Ag/AgCl(sat'd KCl) reference electrode). Once the impedance spectra of the system under study were obtained, parameters governing the electrochemical processes were extracted by fitting the data first according to Randle's equivalent circuit and if necessary the circuit has to be modified to justify the system

under investigation. In these circuits, resistors and capacitors are connected in parallel or in series depending on the physical model of the electrochemical cell. The fitting parameters obtained were then used for the calculation of electron transfer rate (ETR) constant by AC method.

2.4 Electrochemical characterization of GCEs and NEAs

After the RIE step in fabrication of NEAs, they were treated with 1 M HNO_3 to dissolve the Ni catalyst at the exposed CNF tips, followed by chronoamperometry treatment in 1.0 M NaOH by holding the potential at 1.2 V for 20-30 s.

Two probe current-voltage (*I-V*) measurement of VACNF NEAs

I-V measurement of the CNF NEA was done in two-point contact fashion. The two-point contacts were made using spring loaded gold pins, as shown in Figure 2.6a. Figure 2.6b shows a typical two terminal *I-V* curve of CNF NEA. The *I-V* curve is linear, consistent with earlier published reports.[85, 95]

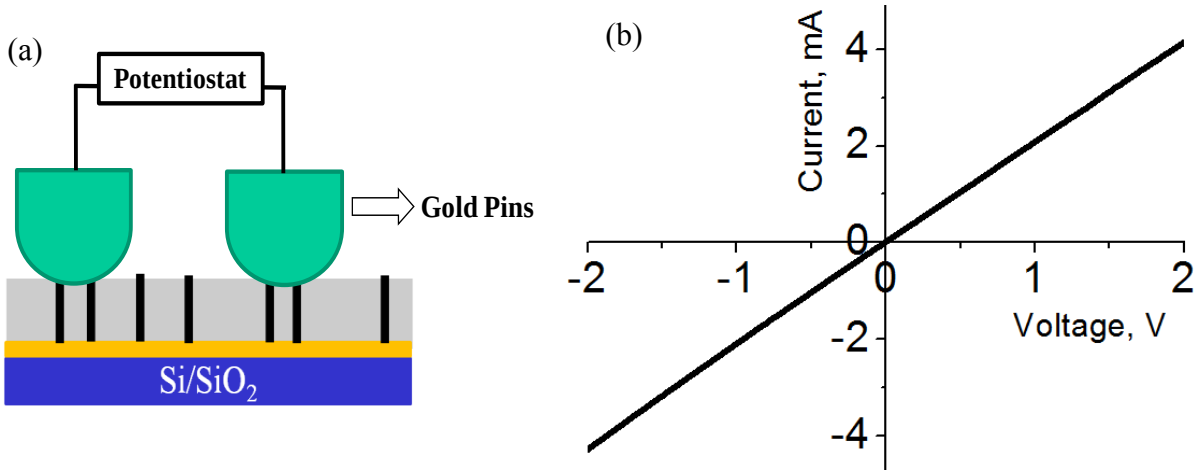

Figure 2.6 (a) Schematic showing the two-terminal experimental set-up for *I-V* measurement. (b) The *I-V* curve of embedded vertically aligned carbon nanofiber nanoelectrode arrays.

CV characterization of GCEs and NEAs

CV with redox species dissolved in bulk solution is commonly used to characterize the electrochemical properties of the WE. CV is a potential sweep method where potential is repeatedly varied linearly with time at a constant sweep rate between two potential limits, to obtain a current-potential (*i-E*) curve. This technique is very useful in illustrating the reversibility

of a reaction, diffusion mode (linear or radial) of the redox species at the electrode surface, diffusion constant (D_0) for a reactant, and to estimate the number of electrons (n) involved in a particular electrochemical reaction.[86] Typical CV obtained for a reversible, one electron reaction (Equation 2.2) at different scan rates with standard macro GCE and NEA with redox species (1.0 mM $K_4Fe(CN)_6$ in 1.0 M KCl) in bulk solution are shown in Figure 2.7. Commonly, the experimental conditions during CV measurement are such that the capacitive current is small compared to the faradaic current (current due to electron transfer). Also, in case of redox couple $Fe(CN)_6^{3-/4-}$ the concentration of $Fe(CN)_6^{3-}$ ("O") and $Fe(CN)_6^{4-}$ ("R") can be readily described by the Nernst Equation 2.3.

$$O + e \longrightarrow R \qquad \textbf{(2.2)}$$

$$E = E^{0'} - 0.0592 \log\left(\frac{[Fe(CN)_6^{4-}]}{[Fe(CN)_6^{3-}]}\right) \qquad \textbf{(2.3)}$$

where E is the applied potential and $E^{0'}$ is the formal electrode potential.

As seen in Figure 2.7a, in case of GCE, when the scan begins at a positive potential, capacitive current flows for a certain time and when the potential is near $E^{0'}$, faradaic current begins to flow due to reduction of the species "O". As the potential become more negative (closer to $E^{0'}$) the reduction current increases. But as E is more negative than the $E^{0'}$, the reduction reaction leads to the drop in the surface concentration of "O". This results in the drop in the current which is limited by the diffusion flux of "O" from the bulk solution. The peak around $E^{0'}$ is thus observed for the reduction of "O" near the electrode surface. All this will result in an *i-E* curve which looks like the scan toward negative potential in Figure 2.7a. When the potential scan is reversed towards a positive potential, the "R" begins to get oxidized. As the potential approaches $E^{0'}$, a peak is emerged due to the oxidation of "R" giving rise to an anodic current. This results in a peak with the opposite current comparing to the forward scan in the *i-E* curve in Figure 2.7a. The choice of initial and switching potential depends on the electroactive (redox) species employed. The switching potential should be at least 35/n mV beyond the peaks in order to observe a clear peak in the reverse direction[86] and the initial potential has to be chosen in such a way that there are no interfering electrode reactions occurring at that potential.

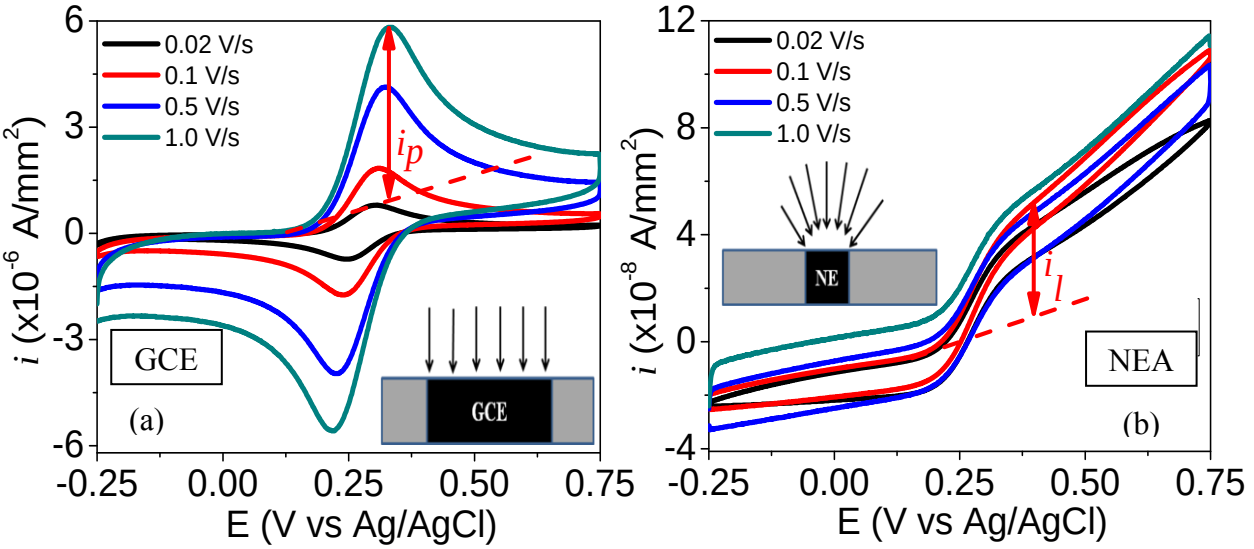

Figure 2.7 Cyclic voltammetry measurements in 1.0 mM K4Fe(CN)6 and 1.0 M KCl performed on the GCE (a) and CNF NEA (b) respectively. Each set of measurements was performed at a series of scan rates of 0.020, 0.10, 0.50, and 1.0 V/s.

For a macroelectrode like GCE, a reversible redox reaction gives a peak-shaped CV, regardless of the scan rate. This is due to the linear diffusion of the analyte to the electrode surface. The peak current (i_p) is given by the Equation 2.4 at 25 ^oC.[86] It is important to note that the i_p is directly proportional to the $\upsilon^{1/2}$, where υ is the scan rate in V/s.

$$i_p = 0.446nFAC_o^* \sqrt{\frac{nFD_0\upsilon}{RT}} \qquad \textbf{(2.4)}$$

In the above equation n is the number of electrons transferred, A is the area of the electrode (cm^2), D_0 is the diffusion coefficient (cm^2/s) of the species, and C_0^* is the bulk concentration of the species (mol/cm^3).

For an embedded disk electrode (NEA), non-linear radial diffusion from the edge starts to dominate over planar diffusion due to the fact that the electrode radius (r) is reduced below the thickness of the diffusion layer. Correspondingly, the CV curve changes from a pair of peak-shaped redox waves to a sigmoidal shape (as seen in Figure 2.7b), indicating the formation of a steady state which has the fixed diffusion layer thickness. The sigmoidal shape also indicates that the NEs are well separated with each other, indicating that the density of exposed CNFs is low. This is necessary for biosensing because, with high density of exposed CNF chips, the diffusion

layers of adjacent NEs will overlap, leading to peak shaped CV curve.[57, 90] The CV signal in case of embedded disk-like NEs can be represented by the height of the sigmoidal curve (i.e. the steady state or limiting current, i_{ss} or i_l) which is given by the Equation 2.4.[60, 86, 96-97]

$$i_l = 4nFC_0^*D_0r \qquad \textbf{(2.5)}$$

Unlike for a macro electrode such as GCE where i_p is proportional to $\upsilon^{1/2}$, the i_l at the NEs is independent of the scan rate. This can be further confirmed by analyzing the CV data at different scan rates shown in Figure 2.7.

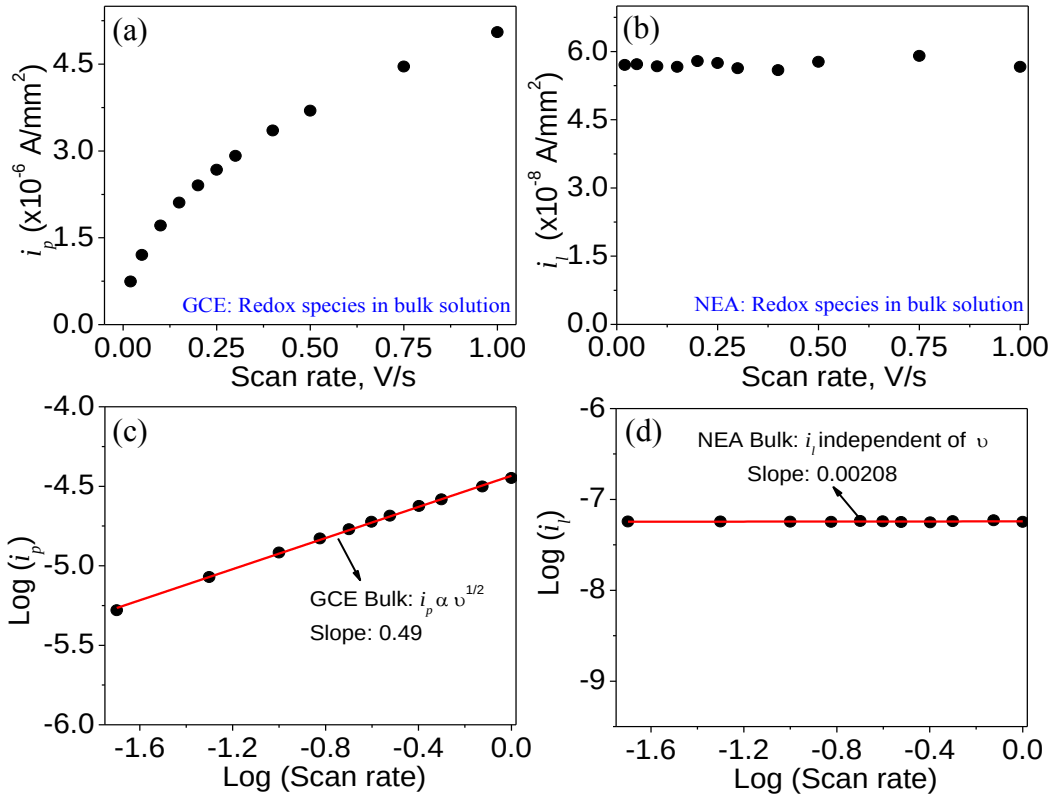

Figure 2.8 (a) and (b) are the plots of background corrected peak currents (i_p or i_l) from cyclic voltammograms plotted as a function of the scan rate for GC and NEA, respectively; (c) and (d) are the plots of Log(i_p) vs Log(scan rate), the solid line is the fitting curve of GC and NEA respectively.

Figure 2.8a and Figure 2.8b summarize the dependence of background-corrected amplitude (i_p or i_l) with respect to the υ for GCE and CNF NEA with bulk $K_4Fe(CN)_6$ solution.

The plots of the same data in log-log scale are shown in Figure 2.8c and Figure 2.8d. As we discussed above, the macro-sized GCE gives reversible waves for redox species in bulk solution with $i_p \alpha \upsilon^{1/2}$. The fitted slope in the log scale plots in Figure 2.8c for the GCE is 0.49, in good agreement with the theory. In contrast to the macro-GCE, a well-separated NEA is expected to show a limiting current i_l in CV with an invariant amplitude vs. υ for redox species in bulk solution.[90] This is exactly what we observed with the low-density CNF NEA as shown in Figure 2.8b. When we plot the data shown in Figure 2.8b in log-log scale, a slope 0.00208 was obtained, which is expected for NEA (see Figure 2.8d).

2.5 Conclusions

To summarize, a reliable procedure for the fabrication of vertically aligned carbon nanofiber nanoelectrode array has been discussed. The SEM data clearly confirms conformal deposition of SiO_2 insulating each individual CNF. Electrochemical characterization of GCE and NEA reveals totally different diffusion mechanism of the redox species at both the electrodes. In case of GCE due to the linear diffusion of redox species, a peak shaped oxidation and reduction signal is obtained and the peak current is proportional to the square root of the scan rate. Whereas NEA displays a sigmoidal shaped curve in cyclic voltammetry, indicating that the diffusion mechanism is radial, and the peak current is invariant of scan rate.

Chapter 3 - Understanding the Electron Transfer Rates (ETRs) at NEAs and GCEs by AC and DC Voltammetry

Reproduced in part by permission of the John Wiley and Sons.

Published as: Syed, L. U.; Liu, J.; Prior, A. M.; Hua, D. H.; Li, J. *Electroanalysis* **2011,** *23*, 1709-1717.

3.1 Introduction

The reduction in electrode size down to nanometers dramatically enhances the detection sensitivity and temporal resolution.[98-99] Various applications with CNF NEAs have been demonstrated earlier for DNA hybridization analysis,[57] glucose detection,[55] neural recording,[100] and gene delivery.[101] CNF NEAs have shown characteristic sigmoidal curve in cyclic voltammetric (CV) measurements of bulk redox species, which is consistent with the expected nonlinear radial diffusion (see the discussion in section 2.4). However, high-performance electrochemical properties with high electron transfer rate (ETR) have not been achieved. CV measurements typically show a large separation in redox peak potentials, i.e. with $\Delta E_p > 100$ mV (in case of NEA, see Figure 3.4b),[57, 81] qualitatively indicating the low ETR at these electrodes. Little is known whether the ETR is limited by the electrolyte/electrode interface or the intrinsic graphitic microstructure of CNFs. To explore more in this area a detailed electrochemical investigation with redox active ferrocene (Fc) molecules attached to the exposed end of CNFs in an embedded NEA has been carried out, as shown in Figure 3.1. Also, same experiments were performed on a standard GCE, for direct comparison of the results.

We employed DC and AC voltammetric techniques to first understand the ETR phenomenon at GCE and NEA. Our study has revealed a striking difference between DC and AC voltammetric results, revealing anomalous ETRs at CNF NEAs, which is likely defined by the intrinsic properties of CNFs rather than the faradaic process at the electrode surface. Our hypothesis to this anomalous behavior is due to the unique conically stacked graphitic structure of the CNF, which behaves as a microstructural electrical network consisting of both capacitive and conductive pathways. High ETR at CNF NEAs can be achieved with high-frequency AC voltammetry (ACV) due to the additional capacitive admittance.

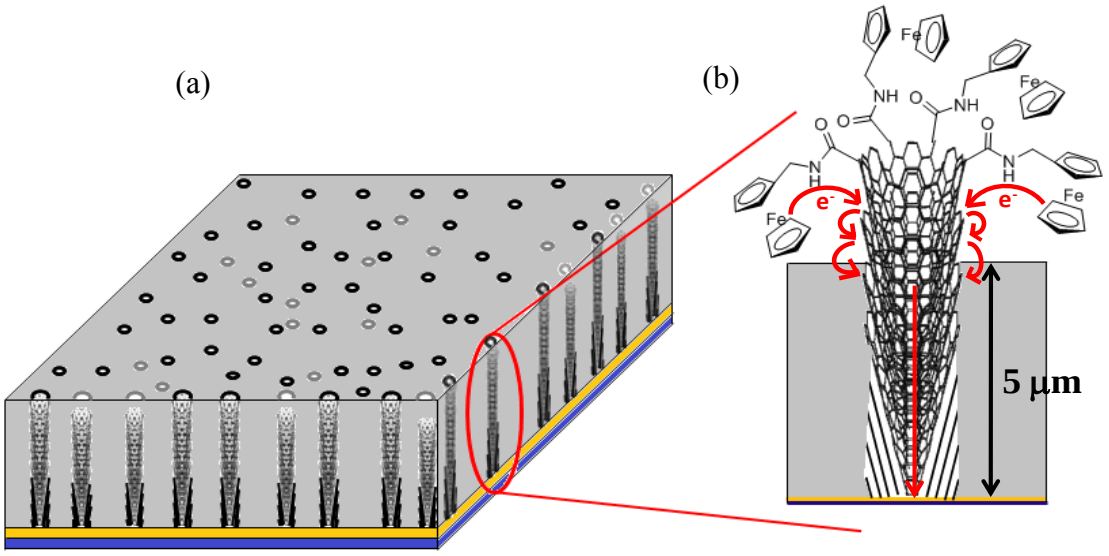

Figure 3.1 (a) Schematic of a nanoelectrode array fabricated with vertically aligned carbon nanofibers embedded in SiO_2. (b) Enlarged to show the redox species (Fc-CH_2-NH_2) covalently attached to the exposed tips of CNFs through an amide bond.

Fc molecules attached to the distal end of molecular wires are commonly used to study electron transfer properties through a molecule for fundamental electrochemistry and potential applications in molecular electronics.[93-94, 102-104] Conjugated molecular wires are normally dispersed in a non-conducting matrix of a self-assembled alkane thiol monolayer on Au electrodes.[93, 104] For short molecular wires less than ~3 nm in length, electron transfer from Fc to the Au electrode was found to be very fast and based on a tunneling mechanism with the resistance scaling exponentially with the length.[93, 104-105] For longer molecular wires, electron transfer changes to a hopping mechanism with a linear relationship between the resistance and the length.[105] Structurally, the CNF NEA embedded in insulating materials is similar to the molecular wires in self-assembled alkane thiol monolayers, though it is ~100 folds in diameter and ~1000 folds in length. CNFs are highly conductive semimetal nanowires with linear I-V characteristics.[85, 95] The resistivity is ~$5x10^{-5}$ to ~$7x10^{-3}$ Ω-cm by measurements from two ends[85] and $4.2x10^{-3}$ Ω-cm by four-probe measurements with side contacts.[95] Previous studies have ignored the intrinsic molecular structure of the CNFs and treated them similar to solid metal wires.

The results presented in this chapter demonstrate that this is insufficient. The unique structure of cup-like graphitic stacking interior of CNFs critically defines their electrochemical properties. Distinct electron transfer mechanisms were found for DC and AC currents. ACV provides ~100 times higher ETR than DC CV at CNFs, which is drastically different from macro-sized glassy carbon electrodes (macro-GCEs). Particularly, the AC frequency that gives the maximum AC current was found to increase from ~75 Hz in the macro-GCE to ~3,500 Hz in the CNF NEA. Thus high-frequency AC technique can cope with the molecular structure of the CNF to open a capacitive admittance route so that ultrahigh detection sensitivity and temporal resolution can be achieved. The understanding of these phenomena is not only critical for electrochemistry and biosensors, but also provides new insights into the fundamental properties of carbon nanomaterials such as carbon nanotubes[50] and graphenes[106] in developing molecular electronics and nanoelectronics.

3.2 ETR at NEA with redox species in bulk solution

As a first step to understand the electrochemical properties of the CNF NEA, DC cyclic voltammetry with non-functionalized CNF NEA at a series of scan rates (υ) in a bulk redox solution, i.e. 1.0 mM $K_4Fe(CN)_6$ in 1.0 M KCl solution, in comparison with a macro-GCE was performed. As seen in Figure 2.7a, the GCE displays a pair of redox waves with a cathodic and anodic peak separation (ΔE_p) of ~57 mV at 20 mV/s scan rate, indicating an ideal reversible redox reaction. The peak current (i_p) increases with the scan rate. In contrast, the CNF NEA displayed sigmoidal features (see Figure 2.7b) indicating the formation of a steady diffusion layer. The density of exposed CNF tips calculated using SEM images is ~1.3×10^6 CNFs/cm^2, indicating that it is a NEA with low density, which is consistent with CV results.

3.2.1 Modified Butler-Volmer model for ETR measurement

One important observation on CNF NEAs is that the CV curves at the high potentials are notably tilt from the horizontal line (see Figure 2.7b). Using the method in the study of bulk redox reactions at an individual single-walled CNT,[107] a modified classic Butler-Volmer model was used to fit the CV curve which revealed that the tilt feature is attributed to a very slow electrode kinetics. The fitting equation for a one-electron process is given as:

$$i_{BV} = \left(\frac{i_{mt}}{1 + e^{-F(E-E^{0'})/RT} + \left(\frac{i_{mt}}{FACk^0} \right) e^{-F(1-\alpha)(E-E^{0'})/RT}} \right) + \left(a(E - E^{0'}) + b \right) \quad \textbf{(3.1)}$$

where i_{BV} is the oxidative current, i_{mt} is the theoretical mass-transport-limited current, F is the Faraday constant, R is the molar gas constant, T is absolute temperature, E is the applied potential, $E^{0'}$ is the formal potential, α is the transfer coefficient, A is the surface area of the electrode, C is the bulk concentration of the redox species, and k^0 is the standard heterogeneous rate constant. The linear term $a(E-E^{0'})+b$ was added to correct the capacitive charging/discharging baseline and the reduction current of residual oxidized $Fe(CN)_6^{3-}$ in the solution. Figure 3.2 shows the fitting line on top of the experimental oxidation CV curve with k^0, α, and i_{mt} as fitting parameters. The area A is fixed at 3.83×10^{-4} cm^2 by summing the exposed area from 1.3×10^6 CNF tips where each tip is approximated as a rod of ~100 nm in diameter and ~75 nm in length, with a 50 nm diameter insulated circular area at the top surface. The fit values are $k^0 = (1.20 \pm 0.056) \times 10^{-2}$ cm/s, $\alpha = 0.820 \pm 0.001$, and $i_{mt} = 0.4630 \pm 0.0027$ μA. The value of k^0 for the CNF NEA is slightly lower than the reported value for $Fe(CN)_6^{3-/4-}$ at HOPG edge plane (0.06-0.1 cm/s)[108] but significantly higher than that at HOPG basal plane ($<10^{-7}$ cm/s).[108] It is within the range for most GCEs (0.005-0.5 cm/s).[108]

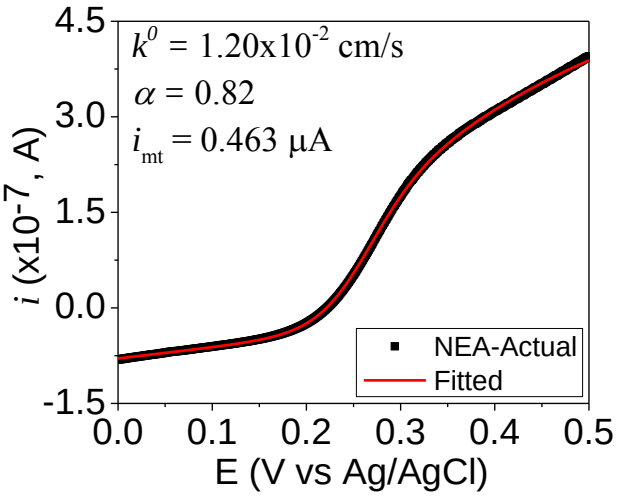

Figure 3.2 The oxidation curve of the cyclic voltammogram of a CNF NEA in 1.0 mM $K_4Fe(CN)_6$ and 1.0 M KCl which is fit with a classic Butler-Volmer model presented in Equation 3.1.

Also, in a recent study S. W. Feldberg discussed the implications of Marcus-Hush theory for steady-state heterogeneous electron transfer at an inlaid disk electrode.[109] It pointed out that Marcus-Hush theory may be more precise than Butler-Volmer formalism by applying reduced operative heterogeneous rate constant k_{ox} at large (E-$E^{0'}$) to account for the diffusion-limited steady-state current. This could be applied on the CNF NEAs. However, the value of the index ($k^0 r_0/D$) is 1.66×10^{-2} with $k^0 = (2.52 \pm 0.012) \times 10^{-2}$ cm/s, $r_0 = 50$ nm, and $D = 0.76 \times 10^{-5}$ cm^2/s for $Fe(CN)_6^{4-}$. At this condition, as pointed by Feldberg, it is not expected to show significant difference between the two formalisms. It would be interesting to investigate this in the future by reducing ($k^0 r_0/D$) below 10^{-3} where the two formalisms are clearly distinguishable,[109] by using smaller CNF ($r_0 < 5$ nm) or redox species with much smaller k^0.

The magnitude of the steady state current (i_{ss}) can be calculated theoretically by making an approximation that each tip is a hemisphere of radius (r) ~50 nm (50×10^{-7} cm) using the Equation 3.2:[86]

$$i_{ss} = N^* 2 \pi F r C D \qquad \textbf{(3.2)}$$

where N is the density of exposed CNF tips (1.3×10^6 CNFs/cm^2), F is Faraday's constant (96485 C/mole), D is diffusion coefficient (~1×10^{-5} cm^2/s) and C is the concentration of the redox species (1×10^{-6} moles/cm^3). The theoretically predicted value of i_{ss} is 2.78×10^{-6} A in the 3 mm dia. geometric area (~3.03×10^{-11} A/CNF), which is ~7 times less than the experimental value of ~4×10^{-7} A (4.36×10^{-12} A/CNF). There are several possibilities that could lead to this small discrepancy. First, the density of exposed CNFs was calculated using SEM images, which only probes a very smaller area (only few μm^2) of NEA substrate. Moreover, the density of exposed CNFs is not the same through-out the chip, since a continuous Ni catalyst film was used which leads to a randomly grown CNF substrate. So, there might be some error associated with SEM based calculations. Secondly, most of the surface of NEA substrate is occupied by SiO_2 which may contain –OH groups from Si-OH and a pH value of as low as 7.5 can deprotonate some of the Si-OH groups to form negatively charged Si-O$^-$ at the interface of the electrolyte and SiO_2 surface.[110-111] This might lead to repulsion of negatively charged $[Fe(CN)_6]^{4-}$ redox species at the interface leading to slightly lower i_{ss}. A more careful study needs to be done in future to account for all the possibilities discussed above. The problem with SEM based density of exposed CNFs

measurement can be easily overcome by using electron-beam patterned NEAs (pNEAs), where density and distance between each CNF can be readily controlled (see the discussion below). The issue of surface charge can be solved by passivating the surface of SiO_2 with inert short polymers/molecules, and with a more careful choice of redox moiety. Lastly, it is to be noted that the Equation 3.2 used for the calculation of i_{ss} is for ideal electrodes. In case of embedded VACNF NEAs we have seen that the ETR is slow, this might also contribute for the low value of experimental i_{ss} compared to the theoretical value.

To eliminate the possibility of error in predicting the density of exposed CNFs using SEM in a random NEA, which leads to the discrepancy between i_{ss} experimental and theoretical, similar kind of study (i.e. ETR with redox species in bulk solution) was carried out using multiplex (3x3) individually addressed "array-in-array" pNEAs. The pNEA chip was provided by Early Warning Inc. and the electrochemical cell shown in Figure 3.3a was constructed by Dr. Bruce Gale's group at the University of Utah through a grant provided by Early Warning Inc.[112]

The patterned CNF array chip consists of a 3x3 array which are individually addressed electrode pads of 200 μm x 200 μm size (Figure 3.3b). SEM images of one such pad is shown as an inset in Figure 3.3c. CNFs are well exposed out of SiO_2 surface (see inset Figure 3.3c). CNFs are patterned into a regular array with a spacing of 1 μm between each fiber. This corresponds to ~40000 CNFs exposed at each pad. The 3x3 electrode pads were connected with 9 external contact pads (1 mm x 1mm) through the metallic line underneath the SiO_2 layer. The bottom part of the electrochemical cell has a reservoir to place the chip at a fixed position, and the top part has a print circuit board with 9 small spring-loaded copper pins that aligns with the 9 contact pads for electrical connections. The cell seals against the CNF array chip through an O-ring of ~1 cm diameter.

The pNEA was given a 10 s of electrochemical treatment in 1.0 M NaOH and then the CV measurements were done using 1.0 mM $K_4Fe(CN)_6$ and 1.0 M KCl solution. The pNEA displayed a sigmoidal shape CV, as expected, but the peak separation still is >150 mV, as seen in Figure 3.3c. The expected magnitude of i_{ss} calculated using Equation 3.2 is ~$1.1x10^{-5}$ A ($3.06x10^{-11}$ A/CNF), which is one order of magnitude higher than the experimentally measured value of ~$1.1x10^{-6}$ A ($3.06x10^{-12}$ A/CNF).

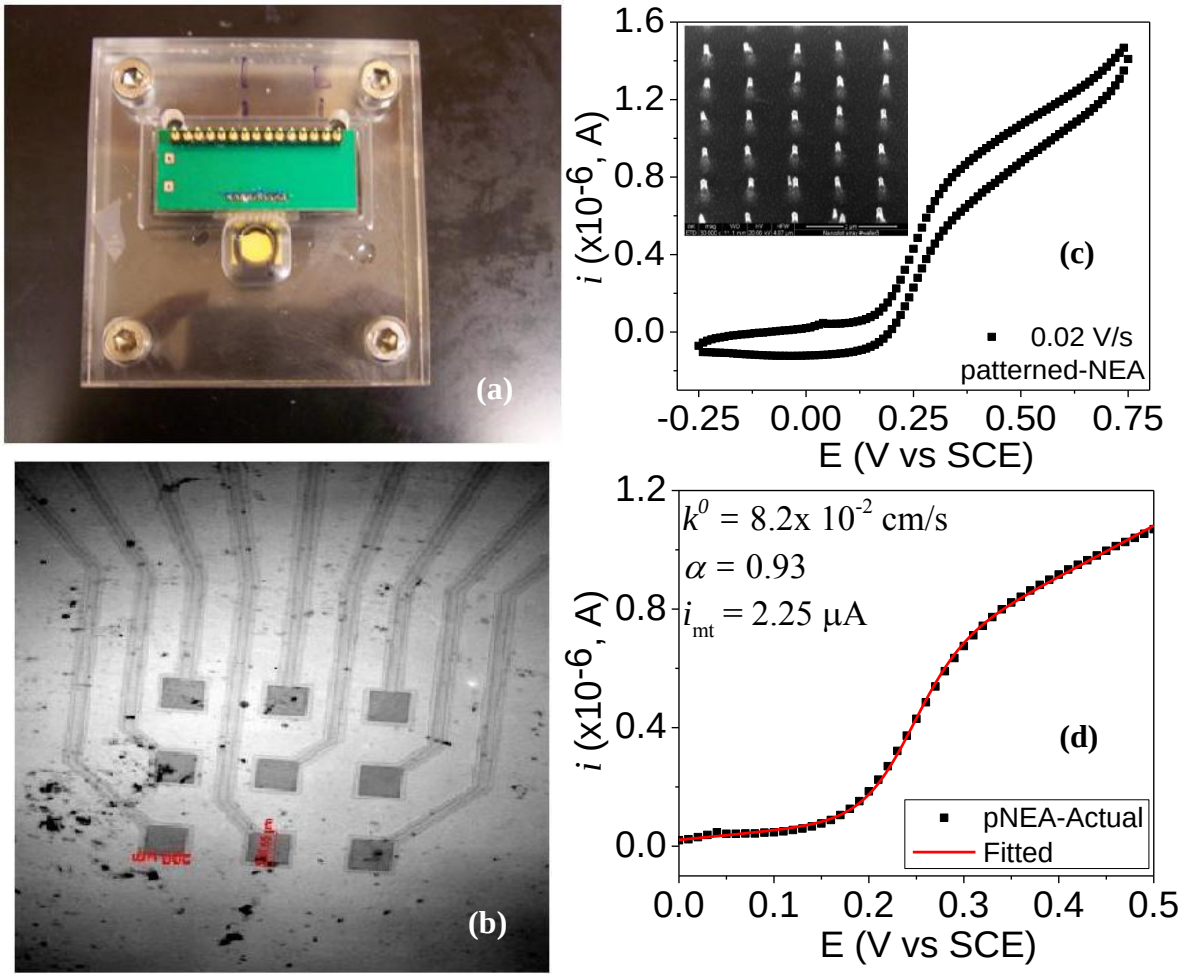

Figure 3.3 (a) Photograph of the electrochemistry cell fabricated by the University of Utah specifically used for testing patterned CNF arrays. (b) A brightfield image showing the 3x3 electrode pads and the metal lines for electrical connection. Each pad is 200 μm x 200 μm. (c) Cyclic voltammogram obtained with pNEA using 1.0 mM K4Fe(CN)6 in 1.0 M KCl solution at a scan rate of 0.02 V/s. Inset shows SEM image of exposed CNFs at one of the pads of pNEA. A SEM image of one electrode pad. The brighter materials are the exposed CNFs. All CNFs are well encapsulated by SiO2 except the exposed tips. The scale bar is 2 μm. (d) The oxidation curve of the cyclic voltammogram of pNEA which is fitted with a classic Butler-Volmer model presented in Equation 3.1. (Figure 3.3a, Figure 3.3b, and inset of Figure 3.3c were adapted from Ref. 112).

Butler-Volmer model was used to fit forward scan of the CV data of pNEA to find the ETR. Figure 3.3d shows the fitting line on top of the experimental oxidation CV curve with k^0, α, and i_{mt} as fitting parameters. The area A is fixed at 1.06×10^{-4} cm^2 by summing the exposed area from $9 \times 40000 = 3.6 \times 10^5$ CNF tips where each tip is approximated as a rod of ~100 nm in diameter and ~75 nm in length, with a 50 nm diameter insulated circular area at the top surface. The fit values are $k^0 = (8.20 \pm 0.001) \times 10^{-2}$ cm/s, $\alpha = 0.930 \pm 0.001$, and $i_{mt} = 2.25 \pm 0.0094$ μA. The value of k^0 for the pNEA is ~7 times higher than random NEA.

3.3 ETR at Fc-CH_2-NH_2 modified GCE and NEA using DC cyclic voltammetry (CV)

To further understand the ETR, we measured DC CVs at various scan rates with a GCE and a CNF NEA in 1.0 M KCl (experimental details can be found in section 2.3) after Fc-CH_2-NH_2 was covalently attached to the carboxylic acid groups at the carbon surface (functionalization procedure is described in section 2.3.2). Since the redox species is covalent attached to the surface of the working electrode, the shape of the CV curves changes completely, when compared to bulk DC CV data, as shown in Figure 3.4.

As shown in Figure 3.4a, a set of redox waves on top of the flat non-faradic background currents are obtained with the GCE. The peak separation ΔE_p was ~29 mV at 20 mV/s scan rate, indicating a quasi-reversible surface redox reaction with a relatively high ETR. The CV of Fc-functionalized CNF NEA demonstrated similar features but with a much larger peak separation ΔE_p= ~81 mV at 20 mV/s scan rate (Figure 3.4b). Apparently, the ETR of Fc at CNF NEA is much lower than that at GCEs, consistent with the measurements with bulk $Fe(CN)_6^{3-/4-}$ solutions. Despite the difference in ETR, the peak current increases as the scan rate rises for both GCE and CNF NEA.

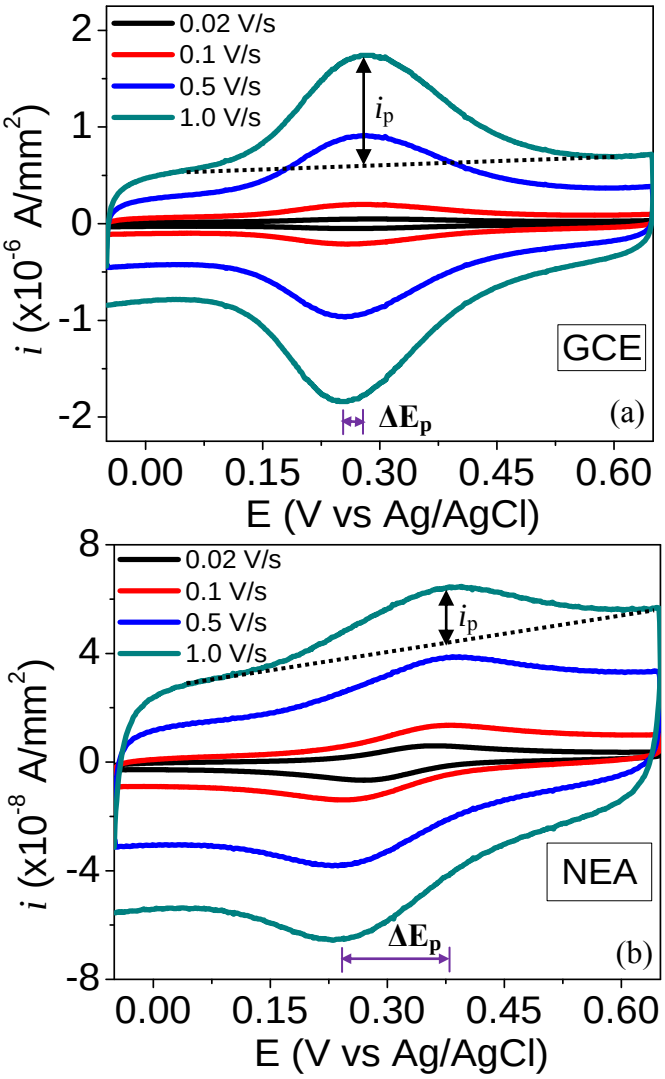

Figure 3.4 (a) and (b) Cyclic voltammetry measurements of Fc-functionalized GCE and NEA in 1.0 M KCl, respectively. Each set of measurements was performed at a series of scan rates of 0.020, 0.10, 0.50, and 1.0 V/s.

3.3.1 Surface coverage and scan rate dependence

The surface coverage (Γ_o) of Fc on GCE and CNF NEA using DC CV data (Figure 3.4a and Figure 3.4b) can be calculated by the Equation:

$$Q = \Gamma_o nFA \qquad \textbf{(3.3)}$$

where, Q is the integrated charge under the peak area of the anodic or cathodic wave and n=1 is the number of electron involved in the redox reaction of each Fc.[86] The derived surface coverage of Fc is Γ_o=1.1 x 10^{14} Fc/cm^2 for GCEs, corresponding to 0.22 closely packed monolayer.[103] At the CNF NEA, it drops to 9.21x10^{11} Fc/cm^2, ~120 times lower than that on the GCE, which corresponds to ~4.9x10^4 Fc/CNF. The number of Fc molecules at each CNF is ~4.5 times higher than that in our previous study[57] due to the longer exposed CNF tip by selective RIE. Reliable signals were obtained even though the Fc coverage was only ~0.0018 monolayer of the geometric surface area.

The scan rate dependence of the peak current further reveals distinct reaction kinetics between the bulk (discussed in section 2.4) and surface-attached redox species. Figure 3.5a and Figure 3.5b summarize the amplitude of background-corrected peak current (i_p) vs. the scan rate of the GCE and CNF NEA with surface-attached Fc, respectively. The plots of the same data in log-log scale are shown in Figure 3.5c and Figure 3.5d. The macro-GCE gives reversible waves with $i_p \alpha \upsilon$ for surface-attached redox Fc, which is evident from a fitted slope value of 0.95 (~1) in the log scale plot in Figure 3.5c for the GCE. In case of Fc-functionalized CNF NEA, the peak current i_p should be linearly proportional to υ, similar to that of the GCE. However, to our surprise, the slope rate of the log (i_p) vs log (υ) curve in Figure 3.5d is only 0.38, much lower than 1. This anomalous behavior in CV of Fc-functionalized CNF NEA is likely attributed to the slow ETR which cannot catch up with the high scan rate, and would thus severely limit CNF NEAs for ultrahigh sensitivity and temporal resolution. This triggered us to explore deeper and to quantitatively determine the ETR for Fc-CH_2-NH_2 attached GCE and NEA. One important parameter necessary to calculate ETR using DC CV technique is the peak separation (ΔE_p) at different scan rates.

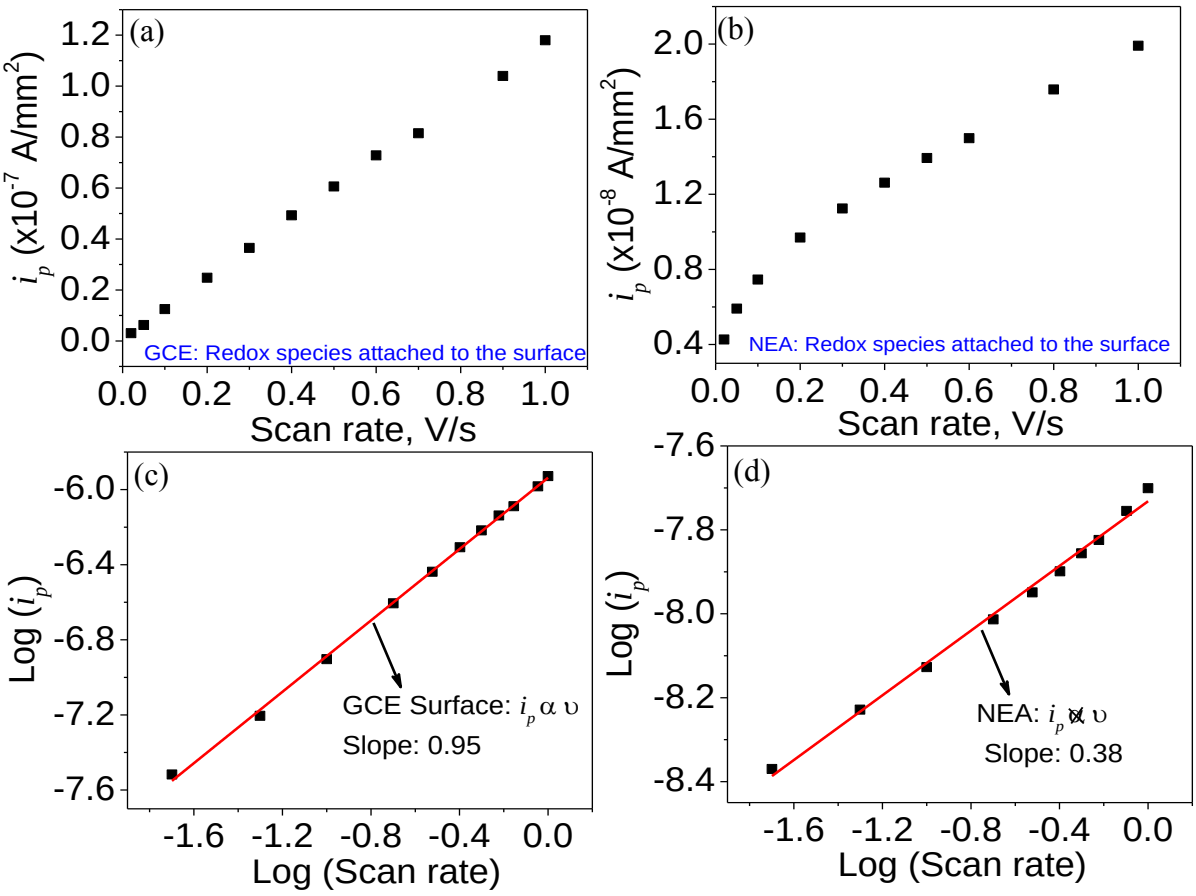

Figure 3.5 (a) and (b) The plots of background corrected peak currents (i_p) derived from the CVs in Figure 3.2 of Fc-functionalized GCE and CNF NEA in 1.0 M KCl respectively. (c) and (d) are the plots of logarithm of (i_p) vs. logarithm of the scan rate, the solid line is the fitting curve of GCE and NEA respectively.

3.3.2 Laviron's approach for ETR calculation using CV data (DC Method)

The ETR constant k^o in literature is generally calculated from the DC CV data by a method described by Laviron,[113] where the peak separation ΔE_p at different scan rates (υ) from CV curves is correlated by a dimensionless rate constant m=(RT/F)(k^0/nυ). For reactions with ΔE_p below 200 mV, m can be readily derived from experimentally measured ΔE_p from Laviron's working curve between m^{-1} and nΔE_p.[114]

Figure 3.6 summarizes a plot of ΔE_p of oxidation and reduction peaks obtained from the CV data of Figure 3.4 as a function of scan rate. It can be observed that, at scan rates less than 0.10 V/s, the increase in the value of ΔE_p for Fc-functionalized CNF NEA is much larger than the

GCE. Whereas, the ΔE_p value on both electrodes is apparently limited by some other processes at DC scan rate larger than 0.10 V/s.

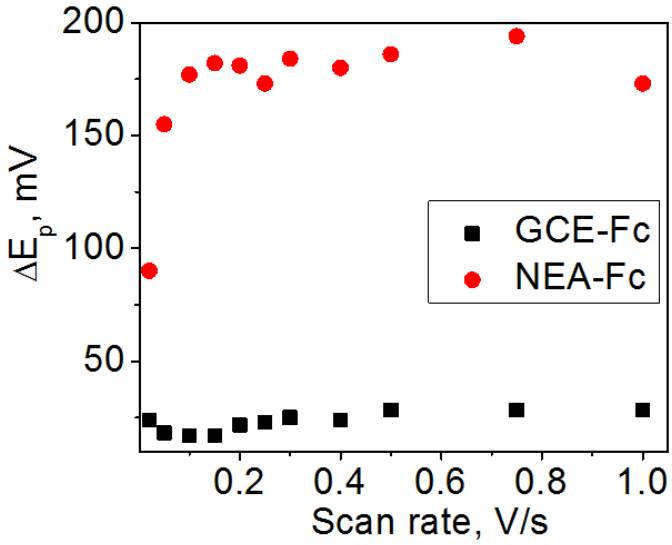

Figure 3.6 Peak-to-peak splitting (ΔE_p) for Fc-attached to GCE and CNF NEA as a function of scan rate.

The k_{dc}^{o} values calculated by this method for GCE and CNF NEA functionalized with the Fc moiety at υ=0.10 V/s are 6.32 s^{-1} and 0.38 s^{-1} respectively (see Table 3.1). The k_{dc}^{o} of the GCE by DC CV is ~17 times of that of the CNF NEA. This is reflected by the difference in ΔE_p (i.e. 177 mV for the CNF NEA vs. 25 mV for the GCE).

Table 3.1 Surface coverage of Fc moiety and the k_{dc}^{o} calculated from the DC cyclic voltammetry data obtained at a scan rate of 0.10 V/s.

Electrode	Γ_o (Fc/cm^2)	$E_{1/2}$ (mV) [a]	**ΔE_p (mV)**	**k_{dc}^{o} (s^{-1})**
GCE	1.1×10^{14}	269	**25**	**6.32**
CNF NEA	9.2×10^{11}	323	**177**	**0.38**

[a] The potential is reported vs Ag/AgCl (sat'd KCl).

In a recent report, Landis et al[115] studied Fc molecules attached through linkers of various lengths to the whole sidewall surface of a bare VACNF array with the average CNF length of 1.0

± 0.3 μm. The ΔE_p was found to be ~50 mV at 100 mV/s scan rate and invariant while the linker molecule is changed from -$(CH_2)_3$- to -$(CH_2)_{10}$-. The calculated ETR constant is k_{dc}^{o} = ~1.2 s^{-1}, which is slightly higher than our results on embedded CNF NEA but much lower than that on the GCE. This indicates that the ETR rate is not limited at the Fc/CNF interface but likely by the intrinsic processes interior of CNFs. With these observations, we hypothesize that, in DC CV measurements with our embedded CNF NEAs, the electron from Fc has to hop between graphitic layers stacked along the 5 μm long CNF axis, leading to the low k_{dc}^{o}. This is analogous to the phenomena observed by Choi et al[105] with long conductive molecular wires over ~4 nm. The slightly higher ETR constant in Landis' study[115] than our results is due to the fact that electrons travel through a much shorter distance in CNFs.

3.4 ETR at Fc-CH_2-NH_2 modified GCE and NEA using AC voltammetry (ACV)

Interestingly, ACV demonstrated dramatically different ETR compared to DC CV measurements. An anomalously high ETR at CNF NEAs was obtained compared to GCEs. ACV has been previously employed by other researchers to study redox kinetics in monolayers of $FcCONH(CH_2)_{15}SH$ on Au electrode surfaces.[93] Higher current signal was obtained in ACV due to the fact that the electrons were cycled at each Fc by the sinusoidal AC wave superimposed on the linear DC potential ramp,[93-94] but the ETR was found to be the same by DC CV (k^0 = 10 s^{-1})[116] and ACV (k^0 = 9-13 s^{-1})[94]. As shown in Figure 3.7, a peak AC current $i_{p,ac}$ corresponding to the redox reaction of surface-attached Fc is observed at +0.275 V for both GCEs and CNF NEAs.

However, the dependence of $i_{p,ac}$ on the frequency of the applied AC voltage is dramatically different at these two types of electrodes. In Figure 3.7a-c, $i_{p,ac}$ at the GCE is very low at the starting frequency of 10 Hz. It increases to a maximum as the frequency is raised to 75 Hz and then decreases until diminishes relative to background as the frequency is raised to 3500 Hz. In contrast, as shown in Figure 3.7d-f, $i_{p,ac}$ at the CNF NEA continuously increases as the frequency is raised until reaching the maximum at 3,500 Hz. It slowly decreases as the frequency is further increased. A substantial signal over the background is still measurable even at 10,000 Hz (see Figure 3.8), the maximum frequency that can be applied by the potentiostat (Model CHI440A, CH Instruments).

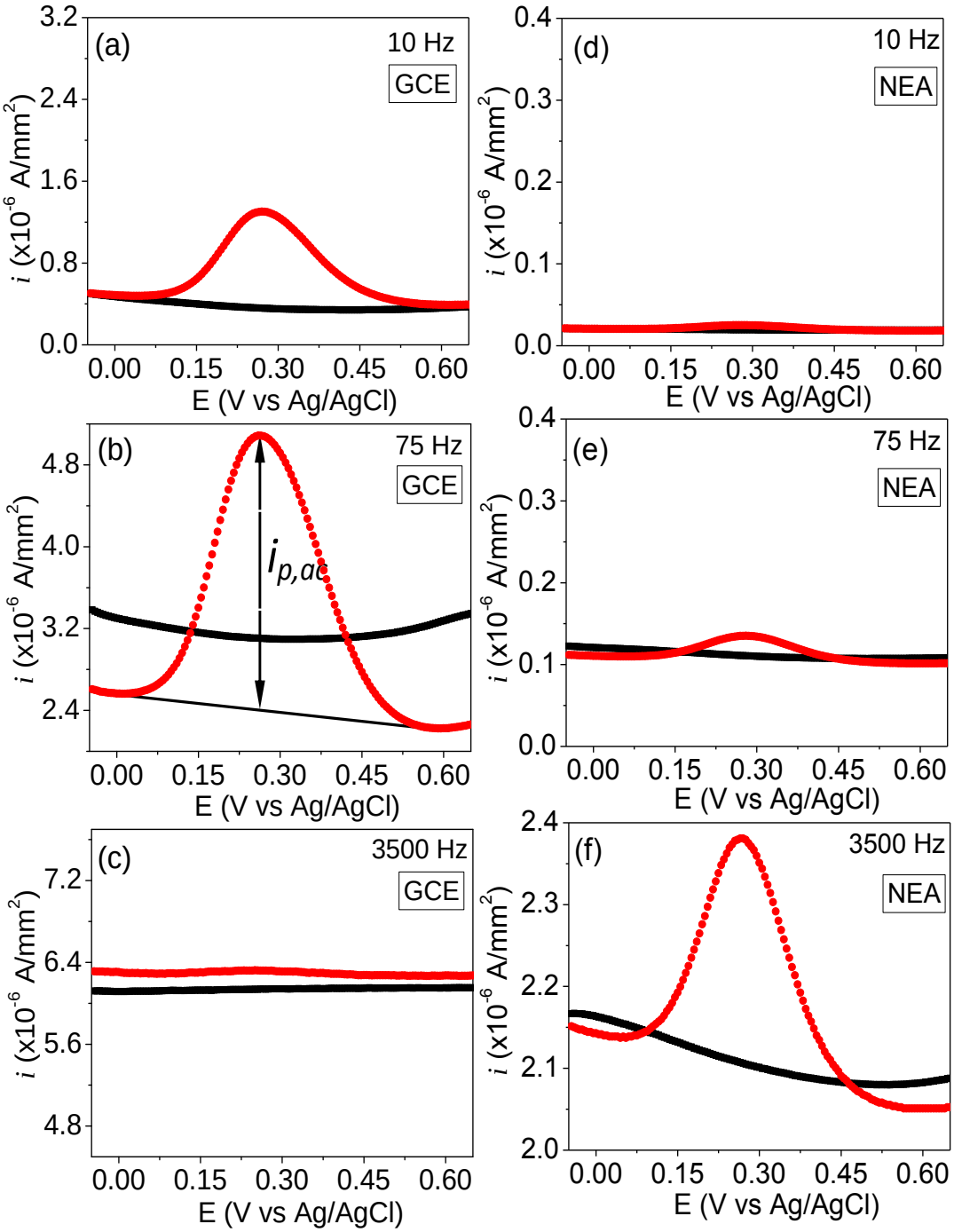

Figure 3.7 (a)-(f) AC voltammograms measured at 10, 75, 3500 Hz with a sinusoidal wave of 25 mV in amplitude superimposed on the DC staircase ramp from -0.05 to 0.65 V at a scan rate of 10 mV/sec. (a)-(c) are the measurements on a GCE electrode, (d)-(f) on a CNF NEA. The black curve is the background measured with clean electrodes in 1.0 M KCl and red curve is the ACV signal in 1.0 M KCl after functionalization of the electrode with Fc.

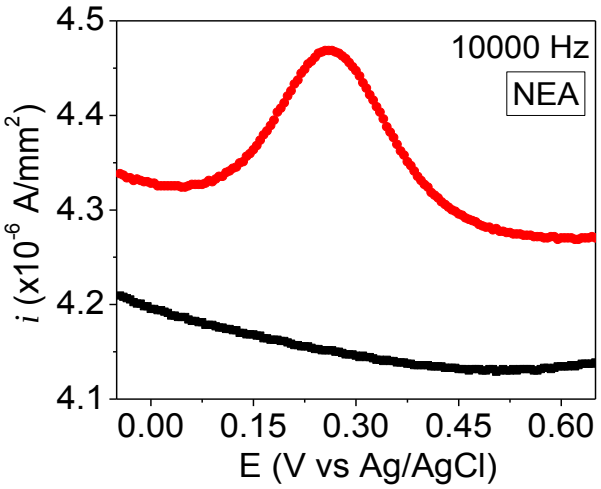

Figure 3.8 ACV measurement performed on a Fc-functionalized CNF NEA at an AC frequency of 10000 Hz and AC voltage amplitude of 25 mV on the DC staircase ramp from -0.05 to 0.65 V at a scan rate of 20 mV/s in 1.0 M KCl.

The difference between GCE and CNF NEAs in frequency dependence using ACV is more striking in Figure 3.9a and Figure 3.9b, where the peak AC current ($i_{p,ac}$) of the surface-functionalized Fc is plotted vs. the frequency in linear and logarithm scales, respectively. The GCE shows a sharp peak in linear scale with the maximum $i_{p,ac}$ at 75 Hz while the CNF NEA presents a much broader peak with the maximum $i_{p,ac}$ at 3500 Hz. In logarithm scale, both GCE and CNF NEA show similar shape. Creager et al[93-94] reported that, as the frequency of the superimposed sinusoidal wave is over certain value, the ACV signal (i.e. $i_{p,ac}$) diminishes because the ETR cannot cope up with the rapidly changing potential and is ultimately limited by the kinetics of the electrochemical reaction. Since CNF NEA reaches the maximum peak current at a much higher AC frequency than the GCE (i.e. 3500 Hz vs. 75 Hz), the electron transfer rate at the CNF NEA should be much higher than that at the GCE. This observation seems to contradict the above-discussed CV study (see section 3.3.2) which shows lower ETR at the CNF NEA. The puzzled difference between ACV and CV studies is probably associated with a different mechanism of electron transfer through the CNF NEA, which has not been reported before.

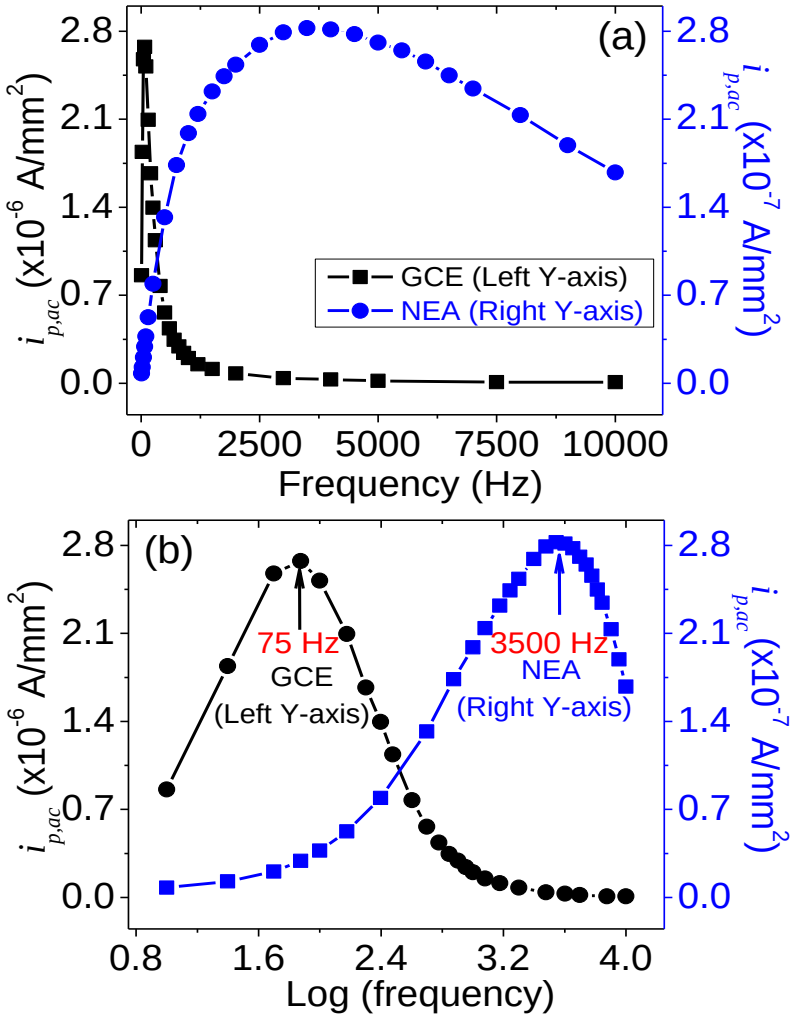

Figure 3.9 (a) Background corrected peak current density ($i_{p,ac,}$ nromalized to the 3 mm dia. geometric surface area) of surface-attached Fc molecules from AC voltammetry plotted against the frequency for a Fc-functionalized GCE and a Fc-functionalized CNF NEA. The maximum $i_{p,ac}$ is at 75 Hz for the GCE electrode whereas at 3500 Hz for the CNF NEA. (b) The same data plotted in log-log scale.

3.4.1 Surface coverage calculation using ACV data

Within the proper frequency range, the peak AC current ($i_{p,ac}$) can be used to estimate the surface coverage as described by Creager et al[93] using the Equation:

$$i_{p,ac} = \left(\frac{F^2}{4RT}\right)(\Gamma_0)(2\pi f)\in \qquad \textbf{(3.4)}$$

where Γ_o is the surface coverage of Fc, f is the frequency, and ϵ is the peak amplitude of the superimposed AC voltage. From the measurements at 100 Hz with a amplitude of 25 mV, we obtained Γ_o=1.03 x 10^{13} Fc/cm^2 for the GCE and Γ_o=3.09 x 10^{10} Fc/cm^2 for the CNF NEA. These values are lower than those calculated from DC CV measurements, which is typical as also reported by other researchers in similar studies.[93-94]

3.4.2 Interpreting the mechanism of larger ACV signal at higher frequencies with NEA

For ACV, we hypothesize that the capacitive coupling between the graphitic layers in the CNF is the dominant mechanism (see Figure 3.10). The measured capacitance at the CNF NEA generally involves two capacitors in series, i.e. (1) the interfacial capacitance (C_{dl}) due to the electric double layer between the electrolyte and the exposed CNF surface, and (2) the space charge capacitance (C_{sc}) inside the conical graphitic layers stacked along the CNF axis. The exposed CNF surface can be treated as a mixture of basal and edge plane. It has been reported that the interfacial capacitance between electrolyte and basal plane graphite show a V-shape curve vs. electropotential, with a minimum value of ~10-20 μF/cm^2 in aqueous solution while that of edge plane goes up to 70 μF/cm^2.[117] Previous study with HOPG electrodes only observed the interfacial capacitance C_{dl} since the C_{SC} of HOPG is much larger.[117] Recently, by using a single-layer graphene in contact with ionic liquids and aqueous solutions, the total measured capacitance was found to be ~5-8 μF/cm^2, which was dominated by the capacitance of the electrode materials and was attributed to the quantum capacitance C_Q of the graphene.[106] But so far the understanding of the capacitance in the stacked graphitic layers and more complicated CNF structure is very limited. A recent study using a stack of controlled number of graphene layers has provided some insights.[118] As the number of graphene layers in the stack increases from 1 to 120, the measured capacitance was found to dramatically increase to approach bulk graphite properties. Since there are much more than 120 graphene layers in a 5 μm long CNF, the interior capacitance of CNFs (C_{CNF} or C_{sc}) will be much larger than the interfacial capacitance C_{dl}. This large interior capacitance of CNFs creates a new electron transfer pathway through capacitive admittance defined by $2\pi fC_{CNF}$. Clearly, this new mechanism particularly favors high-frequency AC techniques since the admittance is proportional to the frequency f. As

a result, the measured ETR in ACV is limited by the interfacial faradaic process in contrast to that by the slow hopping process interior of CNFs in DC CV.

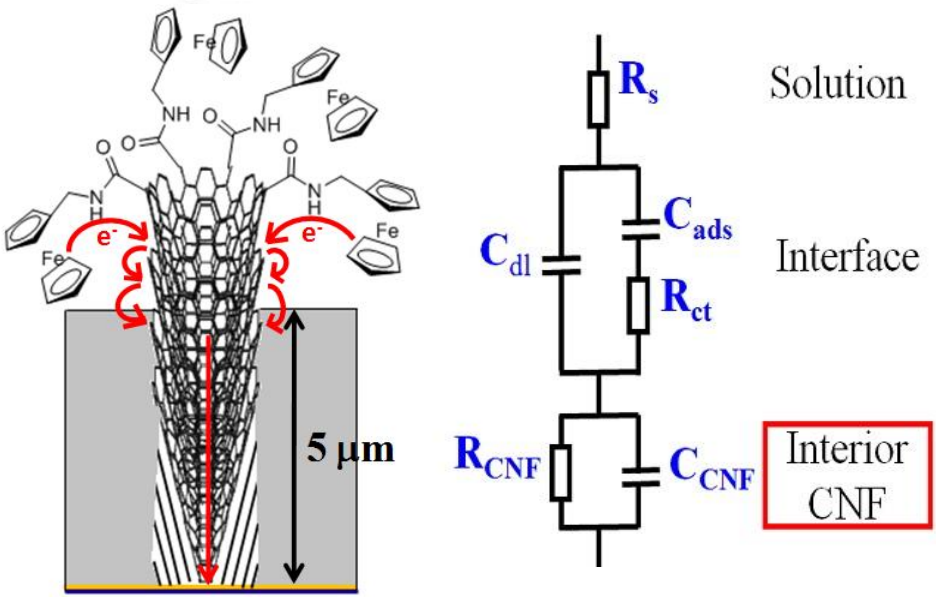

Figure 3.10 Schematic of the electron transfer from covalently attached Fc at the CNF NEA through an amide bond. The hypothesized equivalent circuit for the electron transfer mechanism is shown on right. (Image courtesy: Prof. Jun Li).

In a deeper view, the R_{CNF} (resistance of CNF) and C_{CNF} components along the CNF could behave as a microstructural electrical network consisting of randomly mixed capacitors and resistors similar to the microporous system studied by Almond et al.[119] At the frequency that the capacitive admittance $2\pi fC_{CNF}$ is comparable to or larger than the conductance of the resistive elements (i.e. R_{CNF}^{-1}), AC currents flow across the CNF via a complex set of paths with all components contributing to the network conductivity. This is in contrast to the DC or low-frequency AC currents, where the capacitors are essentially insulators, leaving the hopping paths through the resistive elements alone to determine the network response.

3.4.3 Electrochemical impedance spectroscopy (EIS) study for ETR calculation (AC Method)

To assess the ETR in ACV, EIS experiments were carried out from 100 kHz to 0.1 Hz with Fc-functionalized GCEs and CNF NEAs at a fixed DC potential bias corresponding to the

peak potential for Fc in ACV (i.e. at +0.275 V). The EIS of Fc-attached GCE and CNF NEA have drastically different features (see Figure 3.11) and have to be fit with different equivalent circuits using a complex nonlinear least-squares package (Princeton Applied Research, TN). For the GCE, the equivalent circuit is slightly modified from the Randles circuit used in a previous study of an electroactive monolayer on Au.[94] A resistor R_L attributed to the leaking current has to be added in parallel with the pseudocapacitor C_{ads} corresponding to the faradaic process of the surface adsorbed Fc (as validated by the difference in fitting quality in Bode plots in Appendix Figure A.2). This is likely because no passivation was used on the GCE to block the leakage current unlike the study on Au surface.[52] For the CNF NEA, the intrinsic properties of the ~5 μm long CNF is represented by a capacitor C_{CNF} in parallel with a resistor R_{CNF} (see Figure 3.11b), which is necessary for obtaining a good fit to the EIS data, particularly to the two maxima in the Bode phase plot (see Appendix Figures A.3b and A.4c). The fitting parameters obtained for both GCE and CNF NEA are listed in Table 3.2.

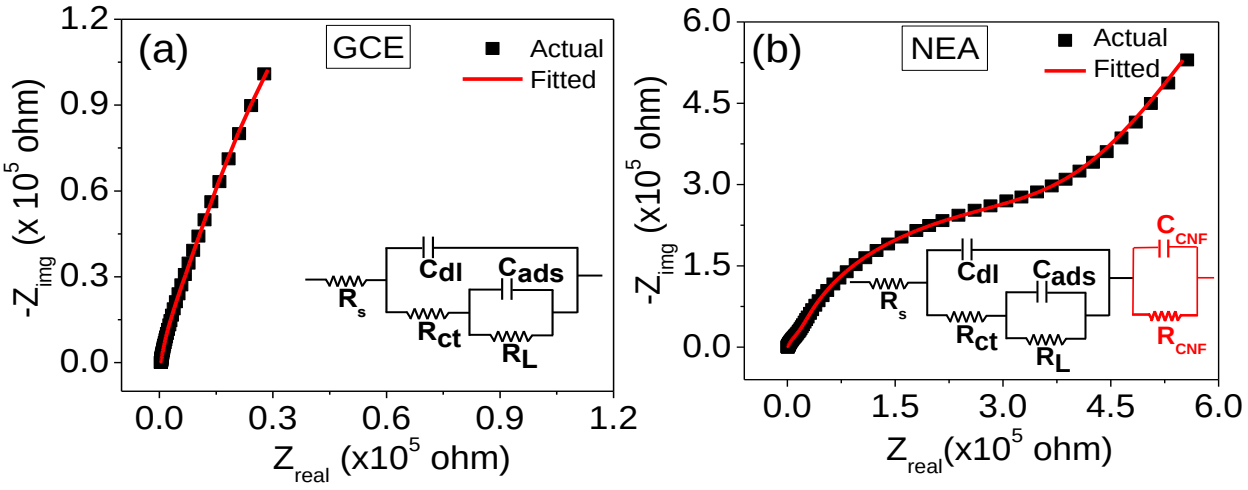

Figure 3.11 Nyquist plots of the electrochemical impedance spectra of ferrocene-functionalized (a) GCE and (b) CNF NEA in 1.0 M KCl. The spectra were recorded at 20 mV voltage amplitude, 0.1 Hz to 100 kHz frequency range, and biased at a DC potential of +0.275 V vs. Ag/AgCl (sat'd KCl). The solid line is the fitting curve obtained by using the equivalent circuits shown as insets. The fitting parameters are listed in Table 3.2.

Table 3.2 Fitting parameters for the electrochemical impedance spectra of Fc-attached electrodes and derived AC ETR constant k^0_{ac}.

Electrode	R_s, Ω	C_{dl}, F (n)	R_{ct}, Ω	C_{ads}, F (n)	R_L, Ω	C_{CNF}, F (n)	R_{CNF}, Ω	k^o_{ac} (s^{-1})
GCE	412.6	1.26×10^{-5} (0.93)	2.37×10^{5}	3.45×10^{-6}	5.57×10^{4}	--	--	**0.61**
CNF NEA	311.3	4.14×10^{-7} (0.864)	5.17×10^{4}	2.55×10^{-7} (0.976)	2.62×10^{5}	2.49×10^{-6} (0.707)	2.95×10^{7}	**38.0**

Note: If a number in the bracket is given below a capacitor, it indicates that a constant phase element (CPE) is used instead of an ideal capacitor and the number represents the value of the exponent *n* of the CPE.

The values of the fitting parameters from the EIS experiments can be used to estimate the ETR constant (by AC method) for surface-attached redox species in ACV by:

$$k^o_{ac} = 1/ (2R_{ct} C_{ads}) \quad \textbf{(3.5)}$$

where R_{ct} is the charge transfer resistance and C_{ads} is the pseudocapacitance by surface-adsorbed redox species. For fitting purpose, the capacitors were replaced by the constant phase element (CPE) as a general practice to account for the heterogeneity at the electrode surface. CPE is defined by the relationship $Z_{CPE} = 1/(C(i\omega)^n)$ where C is the capacitance, ω is the angular frequency and n is a dimensionless exponent whose value range from 0 to 1. The ETR constants k^o_{ac} calculated by Equation 3.5 using the fit values of R_{ct} and C_{ads} (see Table 3.2) are 0.61 s^{-1} for GCE and 38.0 s^{-1} for CNF NEA, respectively. *Apparently, the k^o_{ac} value for the CNF NEA is about 62 times of that of the GCE.*

The equivalent circuit to fit the EIS of CNF NEAs is very consistent with our above-discussed electron transfer mechanism in ACV (as discussed in section 3.4.2). Both the resistive conductance and capacitive admittance contribute to the current flow. The fitting value of R_{CNF} is very high ($2.946\text{x}10^7$ Ω). Thus a low AC frequency f =2.17 mHz is sufficient to make the capacitive admittance equal to the resistive conductance, namely $2\pi f C_{CNF}=1/R_{CNF}$. Since the EIS was taken from 0.1 Hz to 100 kHz, the capacitive admittance is much larger than the resistive

conductance in this range. Little current flows through R_{CNF}. As a result, dropping R_{CNF} by using C_{CNF} alone can generate the same fitting quality (see Appendix Figure A.3c-d). The fitting values of R_{ct} and C_{ads} are only slightly changed, which give almost the same value of ETR constants, i.e. k^o_{ac}=38.1 s^{-1} (see Appendix Table A.1).

3.5 NEA based electrochemical biosensor for rapid profiling of cancerous protease (Legumain)

Globally, thousands of lives are lost every day from various types of cancers. Cancer is the second leading cause of death after cardiac disease in the United States.[120] The best way of preventing these deaths is early diagnosis and effective treatment. It is well known that overexpression of certain enzymes such as kinases, phosphatase, and proteases leads to cancer.[121] Legumain (also known as asparaginyl endopeptidase) is a lysosomal cysteine protease whose activity is found in several tissues.[122] It is found highly expressed in a majority of tumors including carcinomas of the breast, colon, and prostate, and in central nervous system neoplasms.[123] However, overexpression is not found in normal cells. Legumain is present intracellularly in endosome/lysosome systems and extracellularly in tumor microenvironment, consequently making it a potential cancer biomarker. It has also been reported that legumain selectively cleaves asparaginyl carbonyl bond of the tetrapeptide Ala-Ala-Asn-Leu, hence is also known as Asparaginyl Endopeptidase.[123-124]

Towards developing a biosensor for legumain detection, a ferrocenyl tetrapeptide Ala-Ala-Asn-Leu-Fc (i.e. tetrapeptide with a redox moiety at one end) with a $-(CH_2)_4$ linker was synthesized and characterized using high performance liquid chromatography (HPLC) and mass spectroscopy (MS) by collaborating with Prof. Duy Hua. The goal is to apply the findings of the ETR study at the NEAs to build high performance legumain biosensor, i.e. high frequency ACV has to be employed for signal transduction. The tetrapeptide has an amine group at one end which can be used to directly attach it to the NEA or GCE surface using EDC and NHS, as shown in Figure 3.11. Due to the presence of the Fc at the distal end when we use ACV, Fc characteristic signal can be recorded. Commercially available human recombinant legumain was purchased from R&D systems (catalog number: 2199-CY). If we treat the NEAs or GCEs with the protease (legumain) following optimum conditions for incubation like buffer, pH, time, and temperature, then the tetrapeptide will be cleaved (proteolyzed) at the Asn site and the Leu-Fc

moiety will diffuse into the bulk solution. As a result, the ACV signal should decrease, likely the decay would be exponential. To begin with we first wanted to demonstrate that legumain indeed is able to cleave the in-house synthesized tetrapeptide. To prove this we used HPLC and MS, the details of which are discussed below. Therefore, along with the tetrapeptide, the fragment Leu-Fc was also synthesized as a standard of the cleaved product.

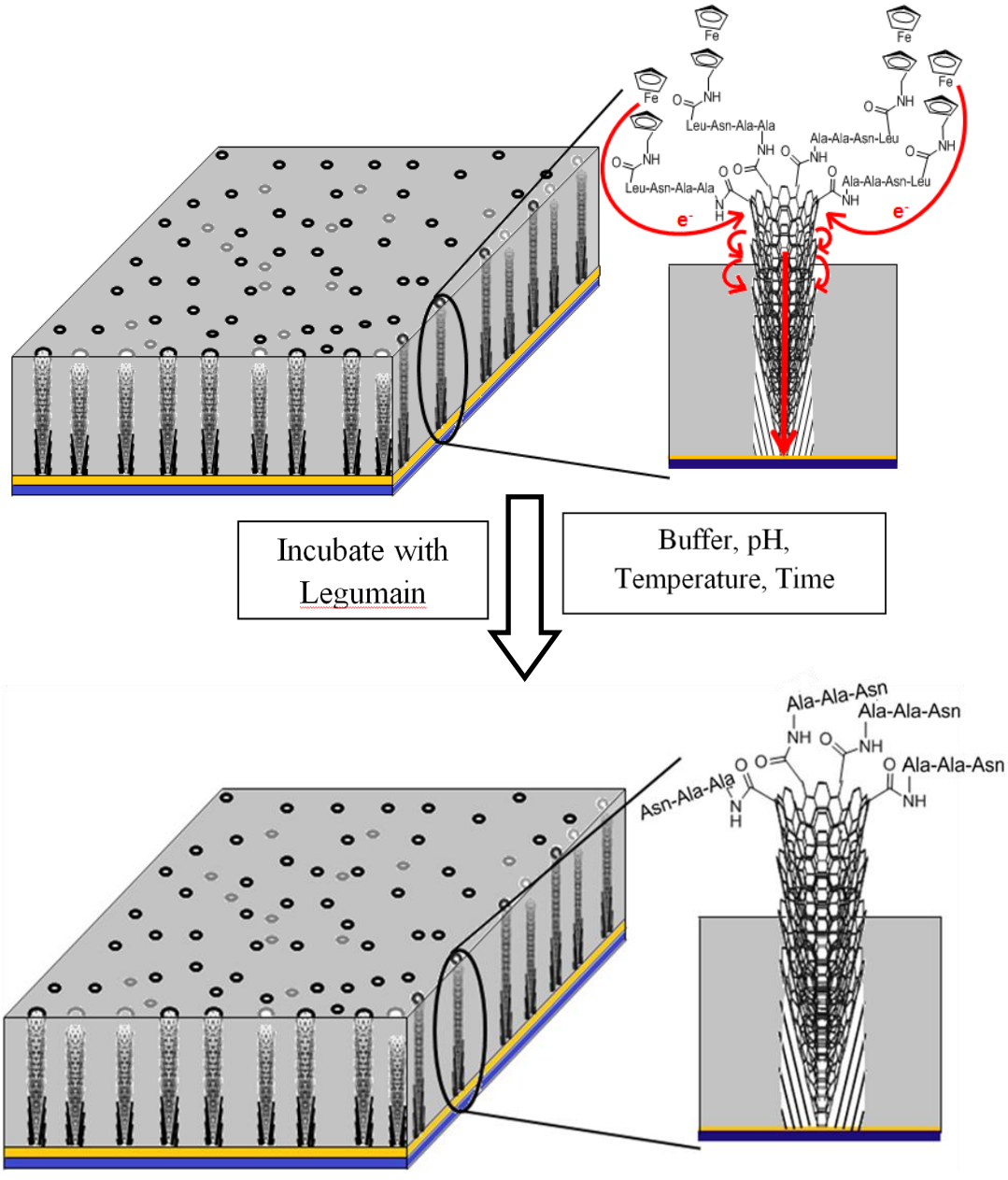

Figure 3.12 Schematic of proteolysis of the Fc-linked tetrapeptide occuring at a CNF NEA by incubating with legumain at optimum conditions.

3.5.1 High performance liquid chromatography (HPLC) and mass spectroscopy (MS) characterization of authentic tetrapeptide and Leu-Fc

Instrument details: HPLC was done using model 210 Varian Prostar with UV-Vis detector and XPERCHROM AEGIS C18 (120 A^o, 10 μm, 250x10 mm) column was used. For each run ~100-150 μl sample (100 μM) was injected directly on the column. Mobile phase used consisted of 0.1 M phosphate buffer (pH 6) and acetonitrile with 0.1% TFA. A flow rate of 10 ml/min was set-up starting with 20% of acetonitrile and ramping it to the 50%. MS measurements were done using API 2000 LC/MS/MS system from Applied Biosystems.

Authentic samples of tetrapeptide and fragment (Leu-Fc) were first analyzed using HPLC and MS. The tetrapeptide was eluted at a retention time of ~10.1 min and Leu-Fc ~12.3 min (see Appendix Figures A.5 and A.6). When a mixture of authentic tetrapeptide and Leu-Fc sample was injected, two baseline resolved gaussian peaks at retention times of ~10.1 min and ~12.3 min were observed (see Appendix Figure A.7). This indicates that the gradient elution protocol of mobile phase is optimum for the separation of tetrapeptide and Leu-Fc. MS of the eluted peaks was done for further confirmation. For the peak with retention time of 10.1 min, which corresponds to the tetrapeptide ($C_{32}H_{49}FeN_7O_6^{2-}$) of calculated mass 683.31 gave a parent peak at 684.5 ($M+H^+$) peak and other prominent peaks at 706.6 and 199.1 corresponding to ($M+Na^+$)and a fragment Fc^+ respectively (see Appendix Figure A.8). The Leu-Fc ($C_{17}H_{24}FeN_2O$) of calculated mass 328.23, which is the peak eluted at 12.3 min gave a small peak at 329.1 ($M+H^+$) and two other prominent peaks at 351.1 ($M+Na^+$) and 199.0 corresponding to the fragment Fc^+ were observed (see Appendix Figure A.9).

3.5.2 HPLC and MS monitoring of tetrapeptide cleavage by legumain in bulk solution

Cleavage of tetrapeptide with legumain in bulk solution was done using the following procedure:

(1) Thaw 2 μl (0.543 μg/μl) legumain on ice for ~30 min. Add 9 μl of activation buffer (50 mM sodium acetate, 100 mM NaCl, and pH 4.0). Incubate at 37 ^oC for 2 hrs (activation of legumain).

(2) Dilute legumain to 1.0 or 3.0 ng/μl in assay buffer (50 mM MES, 250 mM NaCl, and pH 5).

(3) Dilute the tetrapeptide to 200 μM in assay buffer.

(4) Mix legumain and tetrapeptide in 1:1 ratio and incubate at room temperature for 2 hrs. Step 5: Perform HPLC and MS experiments. A control sample with a mixture of tetrapeptide and MES buffer (without legumain) was also incubated for 2 hrs along with the actual sample.

After 2 hrs, first the control sample was injected into the HPLC. The control sample gave a single peak at the retention time of ~10.1 min corresponding to tetrapeptide (see Appendix Figure A.10). The cleavage experiments were done at two different concentrations of legumain, 1.0 and 3.0 ng/µl. When the tetrapeptide incubated with 1.0 ng/µl legumain (sample #1) was injected, it gave two peaks, a major peak at 10.1 min and a small but well resolved and above the baseline noise peak at 12.3 min (see Appendix Figure A.11). The peak at 10.1 min corresponds to the uncleaved tetrapeptide and the other peak at 12.3 min corresponds to the fragment Leu-Fc from the cleaved tetrapeptide. This confirms that, legumain does cleave the tetrapeptide at the Asn site, however qualitatively the percentage of cleavage seems to be less. The area under the peaks was then used to quantitatively estimate the percentage of cleavage. The cleavage percentage obtained with the data shown in chromatogram of Appendix Figure A.11 was about 7%. Then the tetrapeptide was incubated with ~3 times higher concentration of legumain (3.0 ng/µl, sample #2) to increase the cleavage percentage. The sample#2 when analyzed using HPLC gave two peaks with retention times 10.1 and 12.3 min corresponding to uncleaved tetrapeptide and the fragment Leu-Fc respectively, consistent with the results observed in case of sample #1 (see Appendix Figure A.12). The cleavage percentage increased from to 7% to 20%, as estimated using the area under the peaks. Further confirmation was done using MS for the sample#2, where the elutes of the peaks at 10.1 and 12.3 min from HPLC column was collected separately and the samples were then concentrated and analyzed using MS. The results confirm that the peaks observed in HPLC correspond to tetrapeptide and Leu-Fc (see Appendix Figures A.13 and A.14).

3.5.3 Optimization of ACV experimental conditions for legumain detection

Before the actual legumain detection experiments with NEAs can be performed, we first need to characterize the ACV signal at different frequencies in 1 M KCl solution, to find the optimum conditions to measure ACV signal. Representative AC voltammograms at GCE and NEA at frequencies of 100 Hz and 1750 Hz, plotted along with background measurements are shown in Figure 3.13a and Figure 3.13b, respectively. The results of the dependence of peak current with respect to the frequency of the applied sine wave are shown in linear scale in Figure

3.13c and log scale in Figure 3.13d. As expected, in case of GCEs the ACV signal reaches to its maximum value at a much lower frequency of ~100 Hz, where as with NEAs this value jumps to ~1750 Hz.

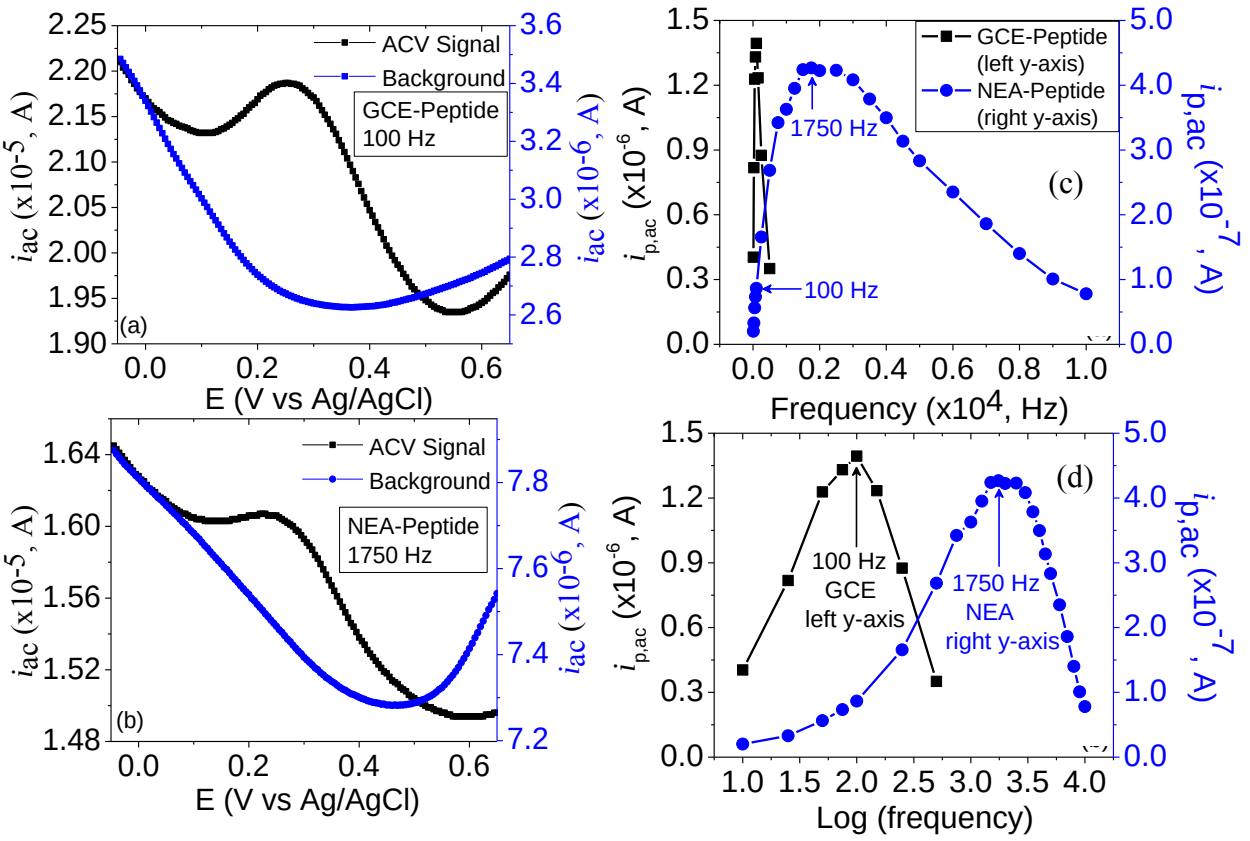

Figure 3.13 (a) AC voltmmetry signal (black curve) at GCE functionalized with peptide in 1.0 M KCl solution, measured at 100 Hz. Blue curve represents the background where no peptide was attached to the GCE. (b) AC voltmmetry signal (black curve) at NEA functionalized with peptide in 1.0 M KCl solution, measured at 1750 Hz. Blue curve represents the background where no peptide was attached to the CNFs. (c) Background corrected peak currents ($i_{p,ac}$) of surface-attached Ala-Ala-Asn-Leu-Fc molecules from AC voltammetry plotted against the frequency for GCEs and CNF NEAs. ACV signal was measured in 1 M KCl solution. The maximum $i_{p,ac}$ is at 100 Hz for the GCEs whereas at 1750 Hz for the CNF NEAs. (d) The same data plotted in log-log scale.

At low frequency of 100 Hz the value of i_p at the NEAs is 8.6×10^{-8} A, whereas at 1750 Hz the value of i_p jumps to 4.3×10^{-7} A, which is 5 times higher. This can be attributed to the fast ETR offered by the NEAs at higher frequencies, consistent with our previous discussion. Further enhancement of the ACV signal is possible by choosing an optimum value for the amplitude of the AC sine wave (in current experiments its much low, 25 mV), which needs to be explored in detail in future. Therefore, under optimum conditions of frequency and amplitude of the AC sine wave we expect that the ACV signal would be atleast 1-2 orders of magnitude larger than regular values that are used in case of standard macro electrodes like gold or GCEs.

3.5.4 Preliminary results of legumain detection

Figures 3.13a and Figure 3.13b shows the preliminary results with GCEs functionalized with ferrocenyl tetrapeptide. It can be clearly seen that after legumain incubation the ACV signal decreases drastically. ACV measurements gave a well-defined peak AC current of $i_p = \sim1.0\times10^{-6}$ A at ~0.26 V (Figure 3.13c), at about the same DC potential as the electrode directly attached with ferrocenylmethylamine (Figure 3.3). After incubation in 250 µl of 1x PBS buffer containing 1.0 ng/ml legumain for ~2 h, the signal ip drops to $\sim2.7\times10^{-7}$ A, indicating that most Fc moieties were removed from the electrode surface by proteolytic cleavage of the Asn-Leu bond. The baseline current (i_b) at 0.26 V also significantly drops from $\sim2.27\times10^{-5}$ A to 1.36×10^{-5} A after incubation. In ideal case one would expect that there will 100% cleavage of the tetrapeptide and almost no peak in ACV measurement after legumain incubation. The reasons to account for this, and also the legumain experiments with NEAs are currently being explored by Li group. Nevertheless, the preliminary results are very encouraging and with further critical understanding of basic concepts would lead us to build an ultrasensitive biosensor for electrochemical monitoring of legumain activity in various cancerous cell lines.

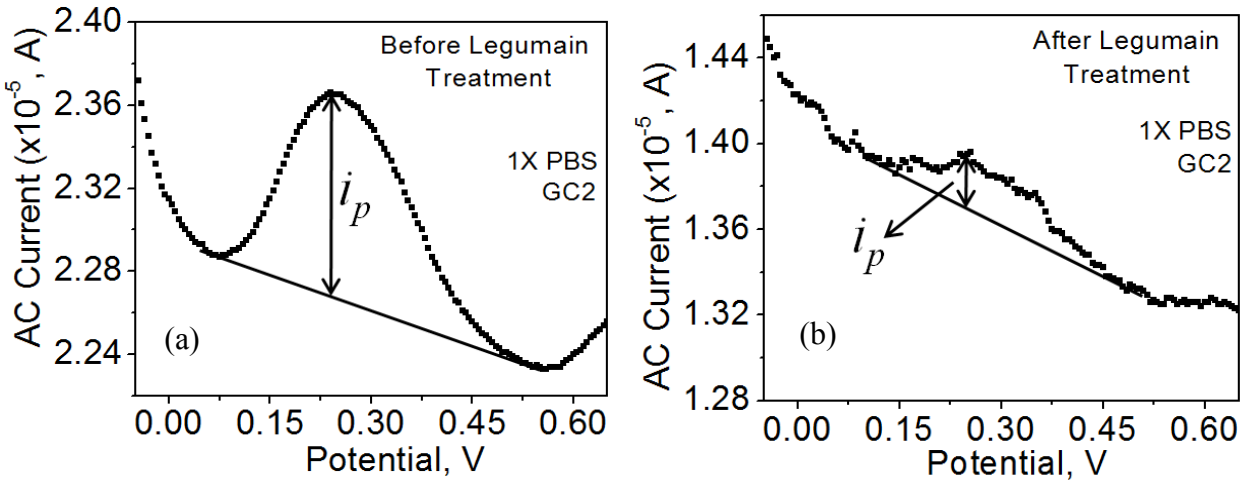

Figure 3.14 AC voltammetry measurements carried out in 1.0 M KCl with a 25 mV AC voltage at 100 Hz before (a) and after (b) incubation of the ferrocenyl tetrapeptide-attached to glassy carbon electrode.

3.6 Conclusions

In summary, we demonstrated that the Butler-Volmer model can be readily used to fit the bulk CV data, which revealed that the slow electrode kinetics can be attributed to the notable tilt in the bulk CV curves. There is about 2 orders of magnitude difference between the calculated and observed peak current value in the bulk CV data, which needs to be carefully investigated in future. Distinct ETRs at the embedded CNF NEAs by AC and DC voltammetry was observed. In DC CV measurements with both bulk $Fe(CN)_6^{4-}$ solution and surface-functionalized Fc molecules, the ETR at CNF NEAs is about 10 times and 17 times lower than on GCEs. However, in ACV, the ETR of surface-functionalized Fc molecules at the CNF NEA is 62 times of that on GCEs. The high ETR at CNF NEAs by ACV is reflected in the capability to obtain the maximum peak current of Fc at 3,500 Hz in CNF NEAs vs. ~75 Hz in GCEs. The difference is likely due to the microstructure of the unique conically stacked graphitic layers in CNFs, which can be treated as a microstructural electrical network with randomly mixed resistive and capacitive pathways. This model is consistent with the equivalent circuits of EIS. A detailed study was carried out to demonstrate that the inhouse synthesized ferrocenyl tetrapeptide can be specifically cleaved at the Asn site using HPLC and MS. The preliminary results of legumain detection using GCEs show a notable decrease in the ACV signal, which is encouraging. Further careful optimization of ACV experimental conditions (like amplitude of AC sine wave), with GCEs and NEAs may

prove even more beneficial, especially in case of NEAs. The critical understanding of the phenomena's discussed in this chapter will provide new insights into the fundamental electronic properties of nanostructured carbon materials and stimulate the development of high-performance biosensors and nanoelectronics.

Chapter 4 - Dielectrophoretic Trapping of Bacterial Cells at Micropatterned Nanoelectrode Arrays

Reproduced in part by permission of the John Wiley and Sons.

Published as: Syed, L. U.; Liu, J.; Price, A. K.; Li, Y.-f.; Culbertson, C. T.; Li, J. *Electrophoresis* **2011**, 32, 2358-2365.

4.1 Introduction

Rapid detection of pathogens like bacteria and viruses is of great importance for monitoring water and food quality, the early detection and diagnosis of diseases, countering bioterrorism attacks, and other applications. Successful detection requires the manipulation and capture pathogenic particles for further analysis. Optical tweezers,[125] acoustic forces,[126] and surface interactions[127] have been used to physically manipulate bioparticles. Another attractive approach is the use of electrical force such as electrophoresis (EP) and dielectrophoresis (DEP) to manipulate cells.[71, 128-131] DEP is of particular interest for capturing pathogenic particles stably in isolated locations of a device. The fundamental principles of DEP were described by Pohl in 1970s. It deals with the motion of a dielectric particle due to polarization effects in a nonuniform electric field.[132] DEP discriminates particles based upon their intrinsic dielectric properties which, to some extent, adds selectivity in the manipulation of one type of bioparticle from a heterogeneous mixture. DEP has been extensively used as a nondestructive and noninvasive technique to detect and separate bacteria,[133] discriminate between live or dead bacteria,[134] detect isogenic mutants of *E. coli* differing exclusively in one mutant allele,[135] and capture and lyse smaller particles like viruses.[136]

Conventionally DEP has been performed using patterned interdigitated electrodes (IDE) and the collection of bacteria mainly takes place at the edges of the electrode.[137-138] However, in many applications one needs to manipulate single cells and preferably capture those cells at isolated spots instead of allowing them to aggregate. Another problem associated with the IDE is that the electrodes are laid at the bottom of the fluidic channel and the ∇E^2 decreases rapidly further away from the channel bottom.[139] To deal with these problems, reversible dielectrophoretic capture and release of a single *E. coli* employing NEA in "points-and-lid" geometry was developed.[131] Fabrication of well-controlled NEAs using VACNFs embedded in

insulating materials on Si substrates has been reported earlier.[90, 140-142] The exposed tips of VACNFs serve as a point's array electrode and a large transparent indium-tin-oxide (ITO) electrode at the top acts as the lid. Recently, it has been reported that precise e-beam lithographically patterned VACNFs can be fabricated as embedded NEAs on individually addressed micropads on the 4" wafer scale.[143] This extends the use of embedded VACNF NEAs for either single or multiplex detection.

This chapter discusses the fabrication of microfluidic device utilizing exposed tips of embedded VACNFs as active nanoelectrodes in a selected area to capture bacterial cells of *E. coli* strain DHα5. The active area is defined by a 2-μm thick SU-8 photoresist to minimize the distance between the nanoelectrodes (NEs) and the *E. coli* cells flowing through the channel. It has been reported that the electric field can be enhanced with non-planar structure with high aspect ratios (~100) as offered by fiber-like NEs.[144-146] The enhanced e-field at NEs in solution was also observed.[131, 147] We demonstrate here that the attractive nanoscale "point-and-lid" design and the increased enhancement in the electric field gradient leads to effective capture of *E. coli* at a high flow velocity up to 1.6 mm/sec. The DEP capture of *E. coli* cells at different AC frequencies and flow velocities are investigated. Towards our goal of label-free electrical detection using dielectrophoretic impedance measurements (DEPIM), we performed the initial electrochemical impedance spectroscopy (EIS) studies. A substantial change in the value of $|Z|$ was observed at 100 kHz, the optimum DEP frequency, corresponding to the capture of *E. coli* cells at the CNF NE tips. Thus it is highly feasible for real-time monitoring the capture process by DEPIM.

4.2 Theory of Dielectrophoresis (DEP)

The term Dielectrophoresis was coined by Herbert Pohl in 1951.[132] It is the movement of a polarizable particle arising from the interaction of non-uniform electric field and the net dipole moment induced in a particle (as shown in Figure 4.1a).[148-149] Due to the non-uniformity of the applied field, the electric field will be stronger on one side of the object and weaker on the other side because of which the pulling and pushing forces will not be fully cancelled, leading to a net force acting on the particle.[150]

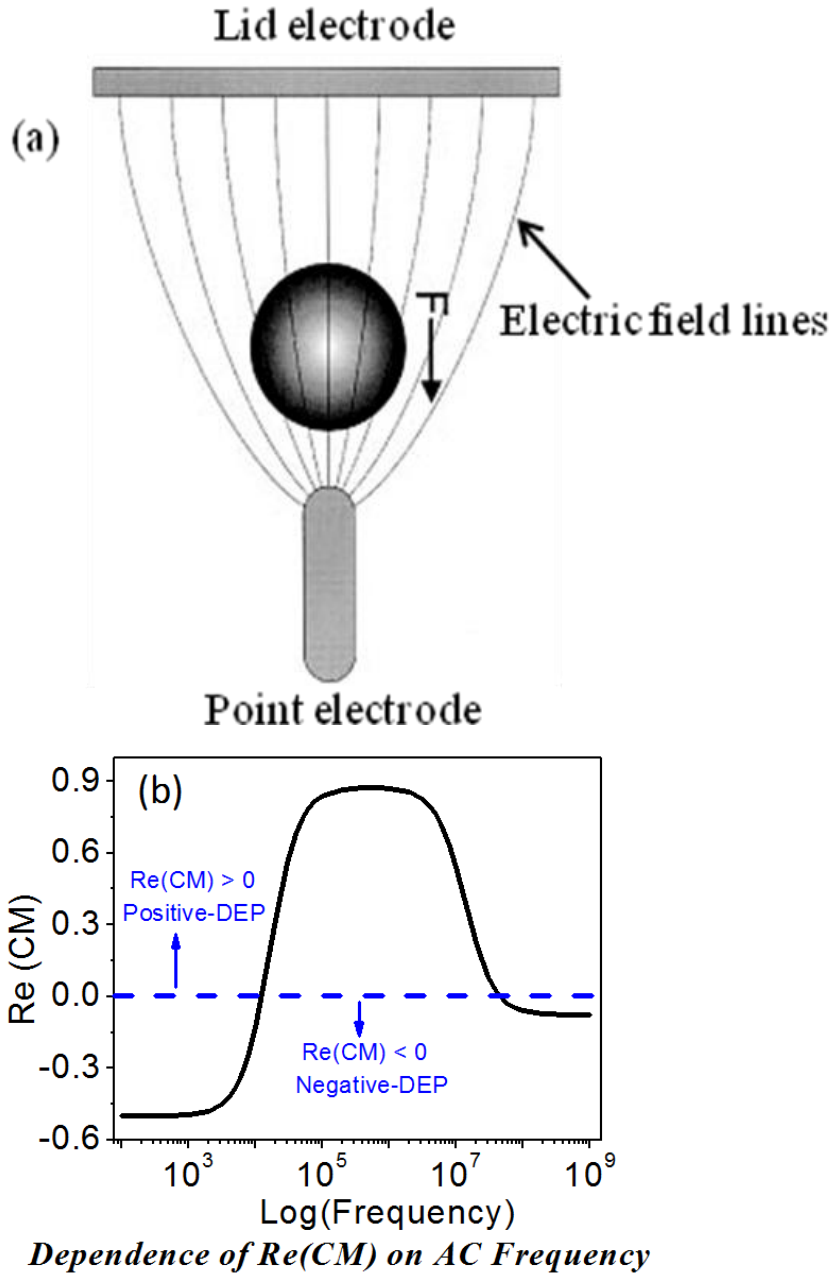

Figure 4.1 (a) Shows net force on a particle experiencing nonuniform electric field (Adapted with permission from ref. 148. Copyright © 2002, John Wiley and Sons.) (b) Schematic showing dependence of CM factor on frequency of the applied field.

The time-average DEP force (F_{DEP}) on a spherical particle is given by:[132, 149-151]

$$\left\langle F_{DEP} \right\rangle = 2\pi r^3 \varepsilon_m \, \mathrm{Re}[CM(\omega)] \nabla E_{RMS}^2 \qquad \textbf{(4.1)}$$

where r is the radius of the particle, ε_m is the permittivity of the suspending medium, ∇E^2 is the gradient of the square of the applied electric field strength (assuming a sinusoidal time dependence), and Re[CM(ω)] is the frequency dependent real component of the complex Clausius-Mossotti (CM) factor, which is given by:

$$CM(\omega) = \frac{\varepsilon_p^* - \varepsilon_m^*}{\varepsilon_p^* + 2\varepsilon_m^*}; \quad \text{Where} \quad \varepsilon^* = \varepsilon - j\frac{\sigma}{\omega} \tag{4.2}$$

with ε^* representing the complex permittivity and the indices *p* and *m* referring to particle and medium respectively. σ is the complex conductivity, ω is the angular frequency ($\omega = 2\pi f$) of the applied electric field, and $j = \sqrt{-1}$. The dependence of the F_{DEP} on cube of the particle radius indicates that DEP is particle volume-dependent (ponderomotive) effect.[152] The magnitude and direction of the F_{DEP} depends on: (1) the difference between the complex permittivity of the particle and suspending medium, (2) the frequency of the applied AC electric field which affects both of ε_p^* *and* ε_m^*, and (3) the magnitude of ∇E^2 which depends on the electrode design/geometry and magnitude of the applied AC voltage, when $\varepsilon_p < \varepsilon_m$, then Re(CM) < 0. Therefore, the dielectric particle experiences negative DEP (nDEP; i.e. particle is less polarizable than surrounding medium) and is pushed towards electric field minima. When $\varepsilon_p > \varepsilon_m$, then Re(CM) > 0, the particle experiences a positive DEP (pDEP; particle is more polarizable than surrounding medium) and will be pulled towards field maxima (these two situations are depicted as a schematic in Figure 4.1b).

4.3 Commonly used electrode geometries for DEP

The most commonly employed electrode geometries for the study of DEP are shown in Figure 4.2.[139, 150, 153-155] With the advances in the micro and nano lithography techniques these geometries can be readily fabricated as thin metal films (1-100 nm) on insulating substrates. Figure 4.2a shows the simplest geometry (two planar electrodes with a gap) where a nonuniform field fringes out of the plane. This kind of design is useful for pDEP (particles will be attracted at the edges of the electrodes) and nDEP, in which the particles will be pushed away from the plane of the electrode. To achieve higher electric field gradients castellated electrodes (Figure 4.2b) are used. For both planar and castellated electrode geometries, interdigitated fingers referred to as interdigitated electrodes (IDEs) are often used. Quadrupole electrode geometry (shown in Figure

4.2c) is normally used for nDEP where particles experiencing negative DEP that are in the plane of the electrodes will be trapped in the center of the electrodes. Figure 4.2d shows schematic of array of microelectrodes (~3 μm diameter) that are used to manipulate cells.[155] The electrode geometry/size plays a key role in controlling the factor ∇E^2, which has dimensions of V^2/m^3.[151-152]

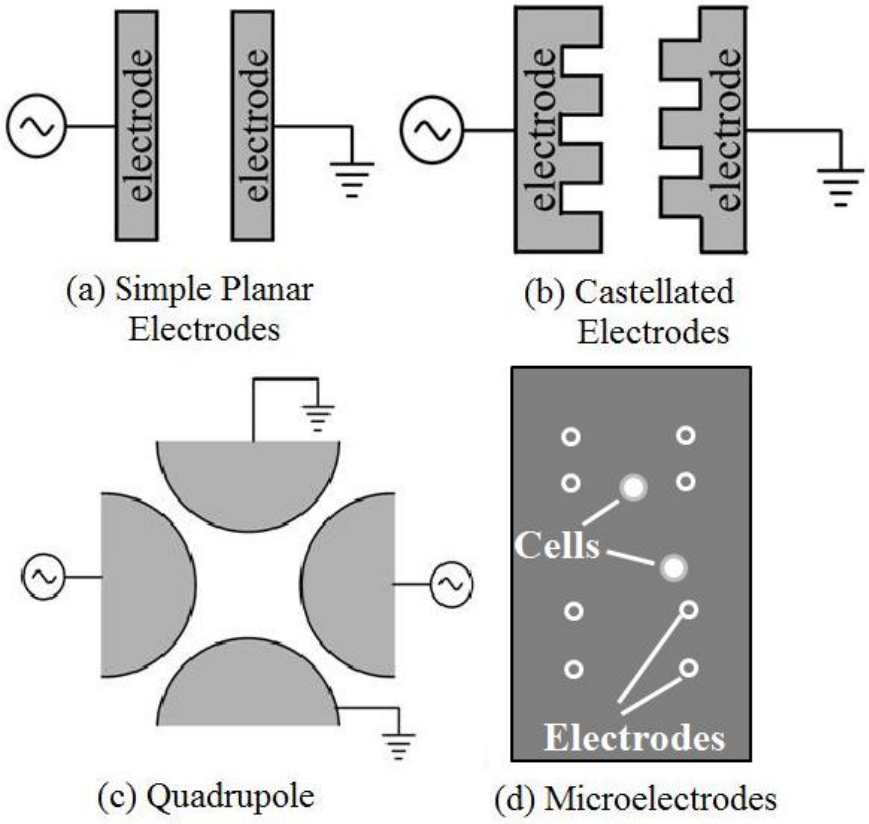

Figure 4.2 Commonly employed electrode geometries for DEP experiments. (a-c: Adapted with permission from ref. 150. Copyright © 2004, American Scientific Publishers; d: Adapted with permission from ref. 155. Copyright © 2004, with permission from Elsevier.)

4.4 Predicting Clausius Mossotti factor using homogeneous sphere model

DEP has been widely used to manipulate biological particles such as bacteria,[70, 137] viruses,[156] spores,[157] yeast[158] and other eukaryotic cell types as well as proteins,[159] nucleic acids,[147, 160] and other biomolecules. These bioparticles have more complicated internal structure and inhomogeneous composition than that of a solid homogeneous spherical particle. Though the structures are complicated, the fundamental physics does not change much if they are properly

accounted for while calculating the DEP force. To account for their heterogeneous structure they can be modeled using single (cross-over frequency determination), and smeared-out multishell model.[161-164] Depending on the availability of parameters from literature, either of these two approaches can be employed to calculate the dependence of CM factor on the frequency of the applied field. Let us now, look at how we can use multi-shell model to predict the DEP behavior of bioparticles, in particular *E. coli* cells, and vaccina virus. This kind of prediction will be very helpful when one want to separate or manipulate a single bioparticle from a heterogeneous mixture.

To predict the DEP response of *E. coli* cells, it is convenient to model it as a sphere covered by two shells (inner shell: cytoplasmic membrane, outer shell: cell wall) as shown in Figure 4.3. The complex permittivity of *E. coli* (ε_p^*) cells has to be replaced with an effective complex permittivity (ε_{eff}^*) which is calculated using the multishell smeared-out sphere model (see Equation 4.3).

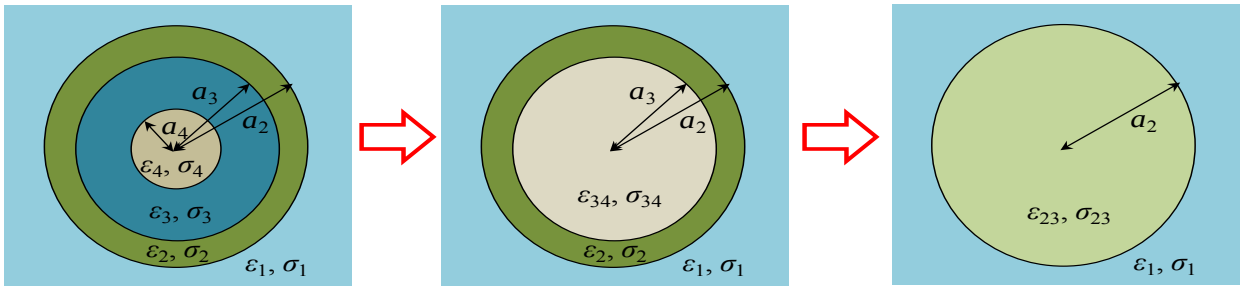

Figure 4.3 Schematic of three shell "smeared-out" model approach for calculating effective permittivity (ε_{eff}^*) of *E. coli* cells.

$$\varepsilon_{34}^* = \varepsilon_3 \frac{\left(\frac{a_3}{a_4}\right)^3 + 2\left(\frac{\varepsilon_4^* - \varepsilon_3^*}{\varepsilon_4^* + 2\varepsilon_3^*}\right)}{\left(\frac{a_3}{a_4}\right)^3 - \left(\frac{\varepsilon_4^* - \varepsilon_3^*}{\varepsilon_4^* + 2\varepsilon_3^*}\right)}; \varepsilon_{23}^*(\varepsilon_{Eff}^*) = \varepsilon_2^* \frac{\left(\frac{a_2}{a_3}\right)^3 + 2\left(\frac{\varepsilon_{34}^* - \varepsilon_2^*}{\varepsilon_{34}^* + 2\varepsilon_2^*}\right)}{\left(\frac{a_2}{a_3}\right)^3 - \left(\frac{\varepsilon_{34}^* - \varepsilon_2^*}{\varepsilon_{34}^* + 2\varepsilon_2^*}\right)}; CM(\omega) = \frac{\varepsilon_{eff}^* - \varepsilon_1^*}{\varepsilon_{eff}^* + 2\varepsilon_1^*} \quad \textbf{(4.3)}$$

The parameters used for the calculation of ε_{eff}^* for *E. coli* cells can be found from previous reports,[134, 165-166] which are listed below in Table 4.1. In most of the DEP experiments water or buffer is preferred as the suspending medium. So, the only parameter which can be varied is the conductivity of the suspending medium. Different scenarios of the dependence of

CM factor based on the conductivity of the suspended medium can be deduced using the Equation 4.3 and the values presented in Table 4.1.

Table 4.1 Parameter values used for theoretical predictions of Re[CM(ω)] for *E. coli* cells.[134]

Component	**Parameter**	**Value**
Cell	Radius	1 μm
Cell cytoplasm	Relative perimittivity (ε_4)	60
	Conductivity (σ_4)	0.1 S/m
Cell membrane	Relative perimittivity (ε_3)	10
	Conductivity (σ_3)	50 nS/m
	Thickness	5 nm
Cell wall	Relative perimittivity (ε_2)	60
	Conductivity (σ_2)	0.5 S/m
	Thickness	20 nm
Suspension medium (DI water)	Relative perimittivity (ε_1)	80
	Conductivity (σ_1)	**Variable** S/m

Similar kind of predictions about the CM factor can also be done for smaller bioparticles like vaccine virus. In case of viruses, the model is simpler due to absence of a cell wall and cell membrane as shown in Figure 4.4. The complex permittivity of *E. coli* (ε_p^*) cells has to be replaced with an effective complex permittivity (ε_{eff}^*) which is calculated using the two shell smeared-out sphere model (see Equation 4.4). The parameters used for the calculation of ε_{eff}^* for vaccina virus can be found from previous reports[136], which are listed in Table 4.2.

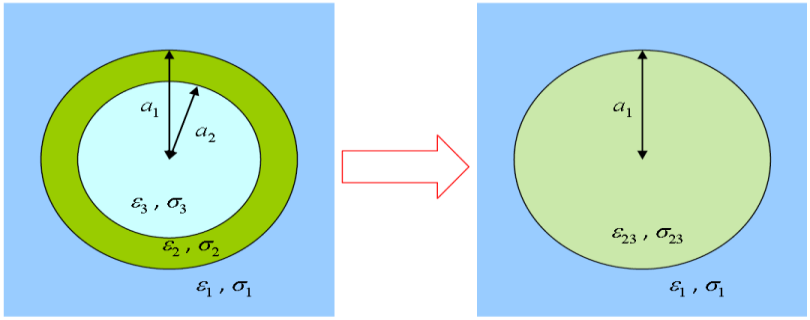

Figure 4.4 Schematic of two shell "smeared-out" model approach for calculating effective permittivity (ε_{eff}^*) of vaccina virus.

$$\bar{\varepsilon}_{23}(\varepsilon^*_{eff}) = \bar{\varepsilon}_2 \frac{\left(\frac{a_1}{a_2}\right)^3 + 2\left(\frac{\bar{\varepsilon}_3 - \bar{\varepsilon}_2}{\bar{\varepsilon}_3 + 2\bar{\varepsilon}_2}\right)}{\left(\frac{a_1}{a_2}\right)^3 - \left(\frac{\bar{\varepsilon}_3 - \bar{\varepsilon}_2}{\bar{\varepsilon}_3 + 2\bar{\varepsilon}_2}\right)} \quad ; \quad f_{CM,23} = \frac{\varepsilon^*_{eff} - \bar{\varepsilon}_1}{\varepsilon^*_{eff} + 2\bar{\varepsilon}_1} \qquad \textbf{(4.4)}$$

Table 4.2 Parameter values used for theoretical predictions of Re[CM(ω)] for vaccina virus.[136]

Component	**Parameter**	**Value**
Bulk	Relative permittivity (ε_3)	65
	Conductivity (σ_3)	1.6×10^{-1} S/m
Membrane	Relative permittivity (ε_2)	10.3
	Conductivity (σ_2)	0.19×10^{-9} S/m
	Thickness	20 nm
Suspension medium (DI water)	Relative permittivity (ε_1)	80
	Conductivity (σ_1)	**Variable** S/m

Using the values listed in Table 4.1 and Table 4.2, the predict spectra of CM factor vs. different frequencies of the AC voltage at various suspending medium conductivities of the *E. coli* cells and vaccine virus is shown in Figure 4.5. Suspending medium conductivities of 0.1, 0.01, and 0.001 S/m were selected in this case.

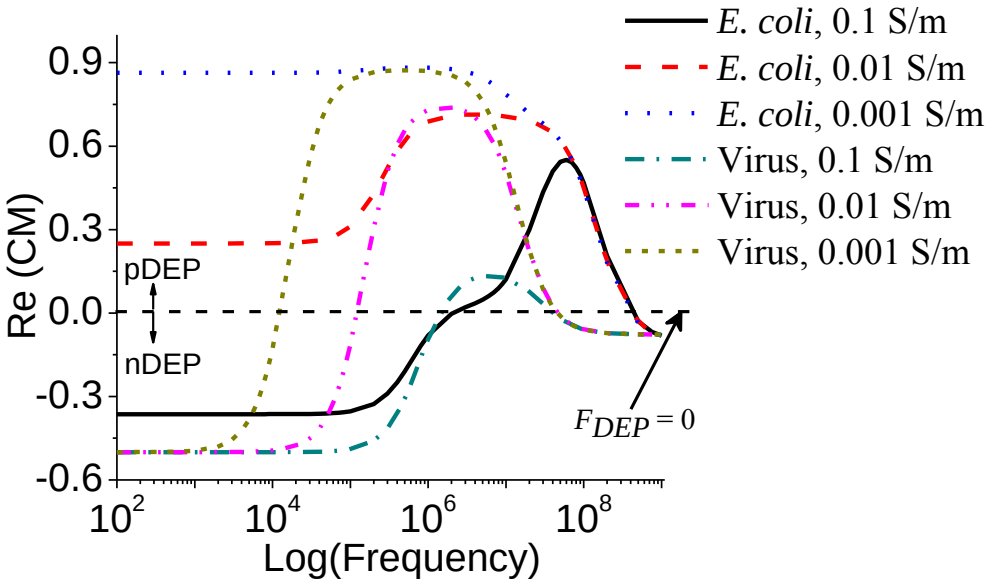

Figure 4.5 DEP Spectrum of *E. coli* cells and Vaccinia virus at medium conductivities of 0.1, 0.01, and 0.001 S/m.

The excel sheet template programmed to calculate the effective permittivity and there by the CM factor for both *E. coli* cells and vaccina virus are attached as supplementary files. It can be observed from Figure 4.5 that, at low suspending medium conductivities (0.01 or 0.001 S/m) and lower frequencies (1-10 kHz), the *E. coli* cells always have a positive value of CM factor leading to a pDEP force, whereas vaccina virus has a negative value of CM factor there by experiencing nDEP. These observations can be very useful for future studies dealing with *E. coli* cells or viruses individually or together.

4.5 Experimental details

4.5.1 DEP Device Fabrication

Fabrication of the DEP device (see Appendix Figure B.1) involves five major steps: (1) preparation of a randomly distributed VACNF NEA covering the whole surface of a Si chip of 1 cm x 2 cm in size, (2) UV-lithography patterning to define an active capture area (200 μm x 200 μm) on the VACNF NEA chip using a 2 μm thick SU-8 photoresist (see Figure 4.7a), (3) UV-lithographic patterning a microchannel of 500 μm in width with a 2 mm diameter circle on a ITO-glass substrate (1 cm x 2 cm) using a 18 μm thick SU-8 photoresist (see Figure 4.7a), (4) aligning and bonding of SU-8 patterned NEA chip and ITO substrates, and (5) making fluidic and electrical connections. The details of each step are given below.

(1) Embedded VACNF NEAs were made by the method described in chapter 2 (see section 2.2).

(2) SU-8 2002 photoresist (Microchem, Newton, MA) of ~2.0 μm in thickness was used to develop patterns on the planarized NEA. The substrate was cleaned by rinsing with acetone several times, blow-dried in air and dehydrated at 150 ^{o}C for 20 min in an oven (Fisher Scientific, 3510-1FS). SU-8 2002 was spin coated on NEA chip at 2800 rpm speed for 40 sec using a spin coater. It was soft-baked at 95 ^{o}C for 75 sec on a hot plate, exposed to UV light (44 mW/cm^2) for 3 sec through a Mylar mask in soft contact mode to define a 200 μm x 200 μm active area, post baked for 90 sec on a hot plate at 95 ^{o}C, developed in SU-8 developer, and washed with isopropyl alcohol (IPA) and dried using a stream of dry N_2.

(3) SU-8 2010 photoresist (Microchem, Newton, MA) of ~18 μm in thickness was deposited on a 2 cm x 4 cm ITO-coated glass electrode by spin coating SU-8 2010 at 1350 rpm speed for 40 sec. It was then soft baked at 95 ^{o}C for 4 min on a hot plate, exposed to UV light

(44 mW/cm^2) for 5.7 sec through the second Mylar mask to define the microchannel and circular chamber, post baked for 4 min at 95 ^{o}C on a hot plate. The remaining steps were the same as explained for NEAs. Finally, two holes were drilled from glass side using a 0.75 mm diameter diamond drill bit at the two ends of the microchannel and then a section (1 cm x 2 cm) of ITO-glass electrode containing the microchannel was diced to eliminate edge-beads, which may interfere with the bonding process.

(4) SU-8 patterned NEA and ITO-glass electrodes were cleaned with IPA to remove dust particles. Alignment markers on both the substrates were used to align them under a regular table top microscope with a 4X objective lens and then a mechanical force was applied to hold the substrates together (see Figure 4.7a and Figure 4.7b). Subsequently, the substrates were placed in a vacuum oven (Curtin Matheson Scientific, Inc) which was preheated to 175 ^{o}C. It was evacuated and held at 25 Torr for ~20 min for the substrates to bond with each other.

(5) Electrical connections to the electrical pads on the NEA and ITO-glass were made using conductive silver epoxy (MG Chemicals, Ontario) and thirty gauge wire. Microbore tubing was connected from a 1 ml glass syringe to the DEP device using sleeves, ferrules and fittings (Upchurch Scientific Inc, WA). A syringe pump (NE-1000, New Era Pump Systems, Inc) was used to control the flow rate during the experiments.

4.5.2 E. coli cell culture and labeling

Frozen *E. coli* DHα5 stock was purchased from Fisher (18265-017) and stored at -80 ^{o}C. For bacterial culture, the stock was thawed on ice for 20 min and inoculated in 2.0 ml LB medium in a sterile culture tube and incubated overnight at 37 ^{o}C. For each DEP experiment, 20 µl of grown culture was transferred into 2.0 ml of fresh LB media and incubated at 37 ^{o}C to reach a cell concentration of ~1 x 10^9 cells/ml into the late log phase. Bacterial cell counting was done using a Petroff-Hausser counting chamber. The cells were centrifuged at 5000 rpm for 5 min and supernatant LB media was discarded. The collected cells were resuspended and washed in ~1.5 ml 1x phosphate buffer saline (PBS) at least 3 times to eliminate the remaining ingredients of the LB media. Labeling of *E. coli* cells was done in two steps, as shown in Figure 4.6. In first step, ~3 x 10^9 cells/ml were incubated with FITC conjugated rabbit anti-*E. coli* Ab (AbD Serotech, NC) at 330 µg/ml for 1 hr at room temperature (RT). The cells were then subjected to pelleting with centrifugation (7000 rpm), and washing with PBS three times. In the

second step, *E. coli* cells were incubated with Alexa 555 conjugated goat anti-rabbit second Ab (Invitrogen, CA) at 130 µg/ml for 1 hr at RT. The labeled *E. coli* cells were pelleted and washed two times with 1x PBS followed by two times with DI water. The cells were finally resuspended in DI water to a desired concentration of ~1 x 10^9 cells/ml for the DEP experiments.

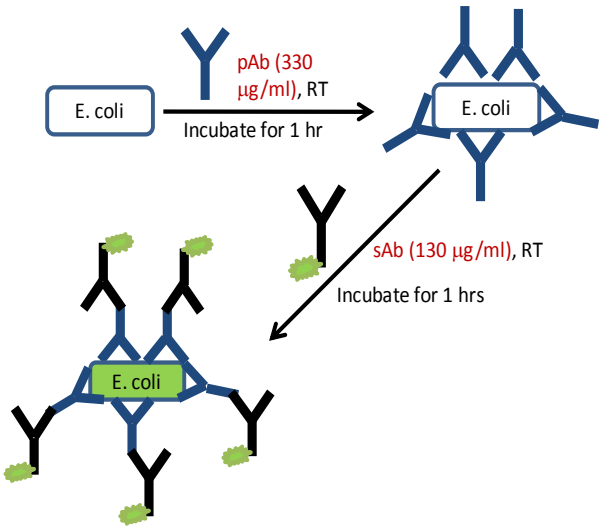

Figure 4.6 Schematic showing two stage labeling procedure of *E. coli* cells using primary antibody (pAb) and secondary antibody (sAb).

4.5.3 DEP capturing experimental details

An upright fluorescence optical microscope (Axioskop 2 FS plus; Carl Zeiss) in reflection mode was used for DEP experiments. The packed fluidic chip was placed under the 50X objective and focused at 200 µm x 200 µm active NE area through the transparent ITO-glass electrode. A filter set with excitation wavelength of 540-552 nm and emission wavelength of 567-647 nm (filter set 20HE, Carl Zeiss) was used in connection with an Axio Cam MRm digital camera to record fluorescence videos at an exposure time of 0.4 s using multi-dimensional acquisition mode in the Axio-vision 4.7.1 release software (Carl Zeiss MicroImaging, Inc). Before performing DEP experiments 1.0 ml BSA solution (2% w/v) was fed through the channel at a flow rate (Q) of 0.2 µl/min to passivate the surface of SU-8 and SiO_2 in the fluidic channel in order to prevent non-specific adsorption of *E. coli* cells. The channel was then washed with 2 ml DI water at a Q = 5.0 µl/min. Labeled *E. coli* suspension in DI water was injected into the channel. DEP experiments at different frequencies (f) of the sinusoidal AC voltage and at

different flow velocities of *E. coli* cells were performed. Each experiment was performed for a span of 30 sec during which no voltage (V_{off}) was applied in the initial ~10 sec, fixed AC voltage at different frequencies was applied (V_{on}) in the next ~10 sec, and no voltage was applied (V_{off}) in the last ~10 sec. Videos were recorded during each experiment. The response of *E. coli* cells was also visually monitored using microscope to determine the optimum frequency of the AC voltage for DEP capture of *E. coli* cells. DEP videos were later analyzed using Automeasure module in Axio vision software to quantify the capture of *E. coli* cells.

4.5.4 Impedance measurement after DEP capture

Electrochemical impedance spectroscopy (EIS) was measured in two-electrode setup before and after *E. coli* cells were captured dielectrophoretically with a potentiostat (PARSTAT 2273, Princeton Applied Research Corporation) with *E. coli* cells suspended in DI water filled between the CNF NEA and the ITO-glass electrode in the microfluidic channel. An AC voltage of 2.8 V_{pp} (peak-to-peak voltage) at the limit of the instrument was applied at the CNF NEA at the open-circuit potential vs. the ITO-glass electrode with the frequency uniformly spanned in the logarithm scale from 1 MHz to 100 mHz. The applied voltage amplitude is much larger than the value of 10-50 mV_{pp} used in conventional EIS measurements since our goal is at developing real-time impedance measurements in which the AC voltage serves both as the DEP driving force and the EIS probe. For capturing, *E. coli* cells were injected into the fluidic channel at a flow velocity of 0.11 mm/sec. The pDEP was applied for 5-10 seconds with an AC voltage of 10 V_{pp} using a wave function generator (Model 33120A, Hewlett Packard) at a fixed frequency of 100 kHz. After capturing enough *E. coli* cells, the flow was turned off while the AC voltage remained on for ~10 minutes. Sufficient number of *E. coli* cells were observed by fluorescence microscope to stick to the exposed tips of the CNF and remained stably attached after the AC voltage was turned off. The cell was then disconnected with the solution sealed in the channel by two inline valves and moved to the potentiostat for EIS measurements.

4.6 Results and Discussion

A critical factor for efficient cell trapping is the strength of F_{DEP} required to overcome the hydrodynamic drag force (F_{DRAG}) excerted on the cells by the fluidic flow which carries the cells moving downstream with fluid. F_{DRAG} could be considerably large at high flow velocities above 100 μm/s. The rationale behind the design of the DEP device is based on the results of DEP

modeling performed using two-dimensional (2D) finite element multiphysics software.[131] According to this study, higher trapping efficiencies are attained either by injecting the particles at a height less than 3 μm from the NEA or by applying a higher voltage bias 9 V_{pp}. Efficient capture was observed at a high flow velocity up to 2 mm/sec. In the same study, a comparison of ∇E^2 and magnitudes of F_{DRAG} and F_{DEP} for particles located at different heights in the channel was made. In the middle of the fluidic channel, the direction of F_{DEP} (namely the vector of ∇E^2) is mostly in vertical direction, which is perpendicular to F_{DRAG} by the fluidic flow.[131] As a result, even a small DEP force is sufficient to deflect the bacterial particles downward as they flow. But as the particle is moved closer to the NEA, a larger horizontal component in ∇E^2 starts to play a significant role which may exceed the horizontal drag force by the fluidic flow and retain the particles at the nanoelectrode site. In this study, the opposite vertical drag force as the particles are pulled down by the initial vertical DEP force F_{DRAG} is neglected since the vertical velocity is negligible comparing to the high lateral flow velocity of the fluid. It was found that, at a height of 2 μm, F_{DEP} is 3 orders of magnitude higher than the F_{DRAG} at a high flow velocity of 10 mm/sec. If a particle is injected at an optimum point above the NEA, high trapping efficiencies even at very high flow velocities can be achieved.

To achieve efficient bacterial capture at a selected location, a square area of 200 μm x 200 μm was opened in a thin SU-8 2002 coating on the NEA substrate which is limited at ~2 μm in thickness in this study. A microchannel of ~18 μm in height was patterned in the 18 μm thick SU-8 2010 layer on ITO-glass electrode. The height of the feature in the SU-8 films on the NEA and the ITO-glass were measured using Ambios Technology XP-2 profiler and was consistent with the design (see Appendix Figure B.2). A bright field image of the DEP device with the active NEA square at the bottom and a microchannel with the circular chamber in the SU-8 on the ITO-coated glass on top is shown in Figure 4.7a. The inset shows an enlarged crossectional schematic of the F_{DRAG} and F_{DEP} on a single *E. coli* cell as it is flowing through the mid of the channel above the active NEA square. A cross-sectional view of the structure of the DEP device is further schematically shown in Figure 4.7b. Fluid enters from one end and collected in a waste collector at the other end. The top-view SEM image of the surface of a CNF NEA is shown in Figure 4.7c, which indicates that the diameter of exposed CNFs is ~100 nm and the density of exposed CNFs is ~2×10^7 CNFs/cm^2 with an average spacing of ~2.0 μm. At such low density,

the exposed CNF tips are well separated from each other and each is expected to behave same as a single NE.

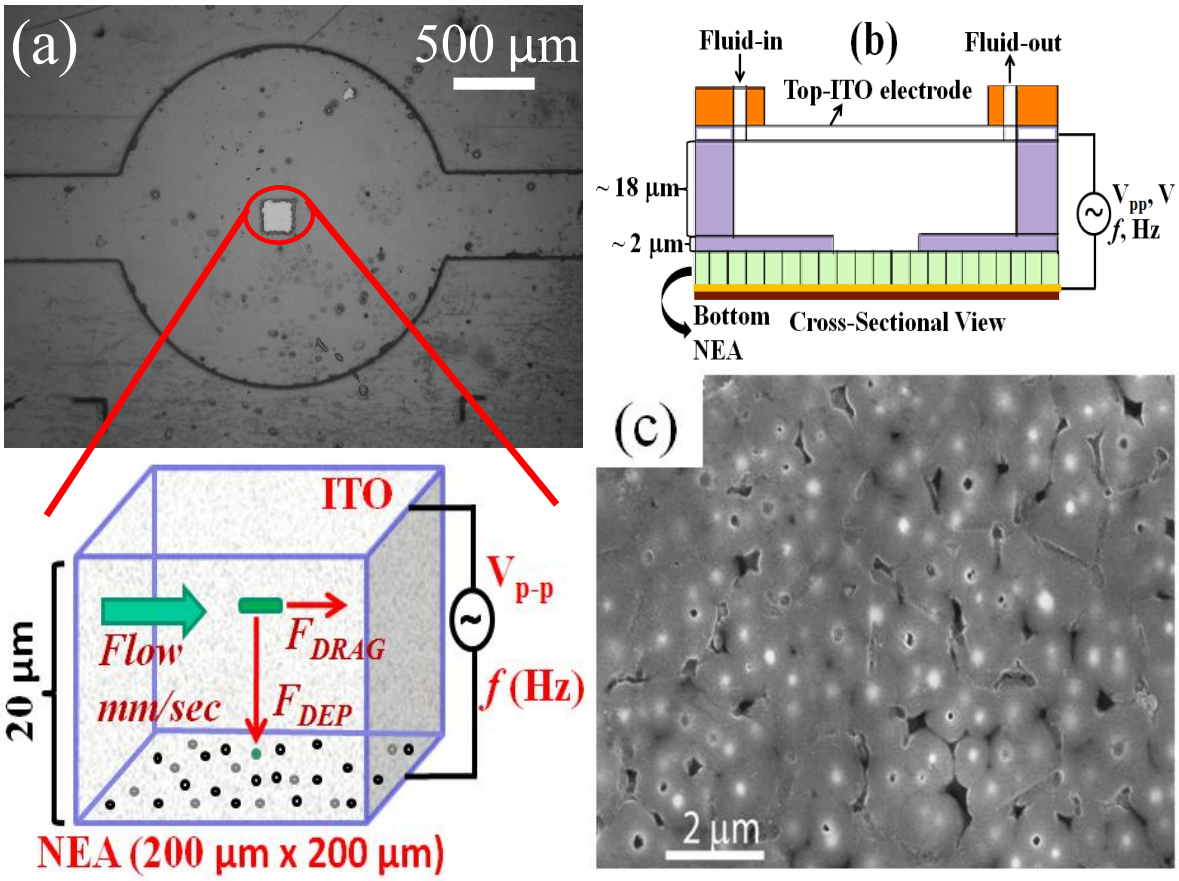

Figure 4.7 Design of nano-DEP device. (a) A brightfield image taken using an upright optical microscope (4x objective) in reflection mode of a DEP device. The small square (200 µm x 200 µm) at the center is the exposed active CNF NEA placed at the bottom. A 500 µm wide microchannel with a 2 mm diameter chamber is patterned on an ITO-glass electrode which is flipped upside down, placed on top CNF NEA, and aligned to the center of the square. The inset beneath shows the enlarged schematic of an *E. coli* cell influenced by the major forces when it flow through the channel between the two electrodes where a AC voltage is applied. The total height of the channel is 20 µm. (b) A cross-sectional schematic view of the nano-DEP-device. (c) A scanning electron microscopy image (top view) of the CNF NEA showing exposed CNF tips.

The captured *E. coli* cells at each exposed CNF tip appear as round bright spots as shown in the enlarged schematic of the device in Figure 4.7a. As the AC voltage is turned-off the captured *E. coli* cells are released and pushed away from the exposed tips by the hydrodynamic drag force F_{DRAG} from the fluidic flow. To stably capture the cells, the F_{DEP} has to somehow overcome F_{DRAG} acting on an *E. coli* cell. When an AC voltage of proper frequency is applied to the CNF NEA, *E. coli* cells will be pulled by the pDEP force (F_{DEP}) toward the exposed tips of NEA and remain captured as long as the AC voltage is on. DEP capture experiments at various AC frequencies (50 kHz to 1 MHz) at fixed AC amplitude of 10 V_{pp} were first carried out. The number of captured *E. coli* cells is quantified by counting the number of individual fixed bright spots using Automeasure module of the microscope software. Figure 4.8 shows a plot of number of bright spots at different frequencies of the AC voltage. It can be observed that there is least number (~30) of bright spots at 1 MHz frequency whereas the count was maximum (~300) at 100 kHz, indicating more *E. coli* cells being captured at the NEA. Clearly, 100 kHz gives the best capture efficiency for pDEP capture of *E. coli* cells. Thus the 1 MHz AC voltage used in the previous study[131] was too high and far from the optimum condition.

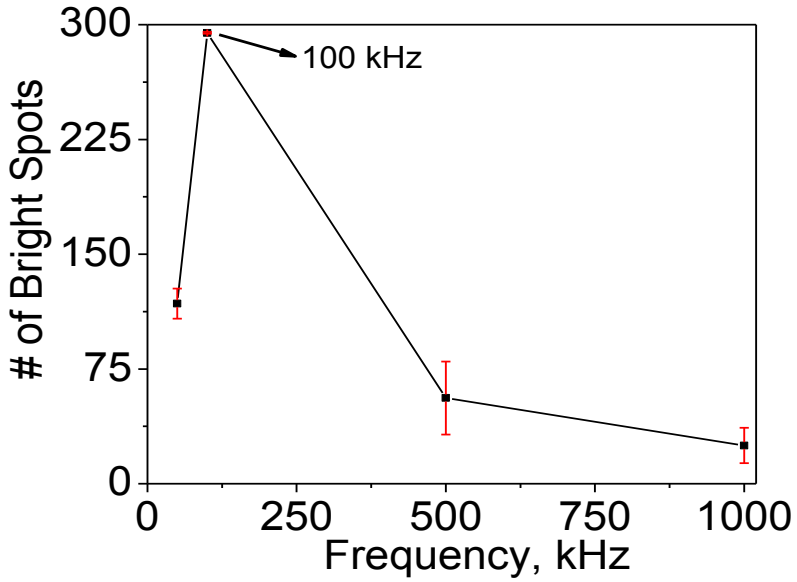

Figure 4.8 The number of bright spots count in each pDEP experiment vs. the frequency of the applied AC voltage. All experiments use an AC voltage bias of 10 V_{pp}. The maximum trapping efficiency is obtained at 100 kHz.

The conductivity of the solution suspended with ~1 x 10^9 cells/ml is 6.74 μS/cm, only ~3.5 times higher than the value of 1.9 μS/cm for ultrapure DI water. Using the value of 6.74 μS/cm for the suspending medium, the dependence of CM factor on the frequency of the AC voltage was studied, with all other parameter same as discussed above in section 4.4. As seen in Figure 4.9, at all frequencies below ~10^7 Hz, *E. coli* cells are expected to experience approximately same DEP force. At higher frequencies (>10^8 Hz), CM factor becomes negatives indicating that *E. coli* cells will experience nDEP. The variation of the CM factor vs. frequency between the theoretical calculation and experimental observation of *E. coli* cell capture (as shown in Figure 4.8) is not consistent at this stage. One possibility could be due to the attachment of antibodies on the surface of *E. coli* cells, causing a thicker protein cell wall. However, increasing the thickness of cell wall by ~20 nm does not show any change in the calculated CM factor (red curve in Figure 4.9). On the other hand, from theoretical calculations (see Figure 4.5), we know that at high medium conductivities, CM factor can flip from positive to negative as the frequency is lowered. There might be some error when conductivity measurements were done or if any residual salts left due to PBS buffer in the channel might change the local conductivity, which leads to the difference in theoretical calculation and experimental observations. This needs to be carefully investigated in details in future studies.

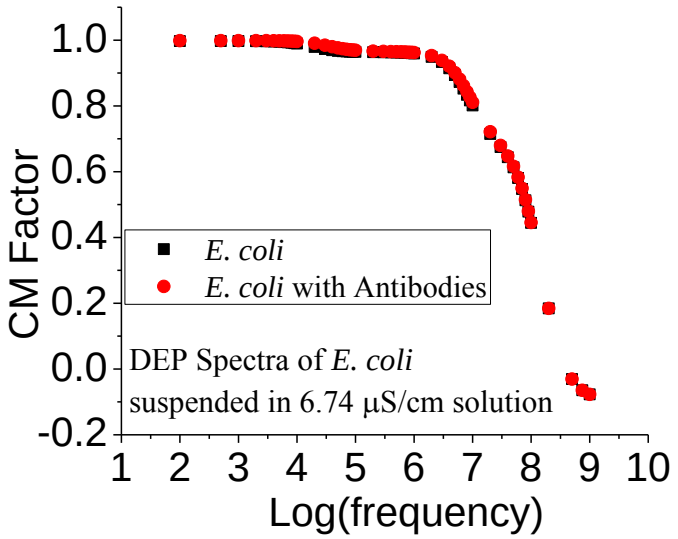

Figure 4.9 Calculated CM factor of *E. coli* cells suspended in a medium with the conductivity of 6.74 μS/cm.

We then carried out pDEP capture experiments with AC voltage fixed at the frequency of 100 kHz while sequentially increasing the flow velocity of *E. coli* cells from 0.11 mm/sec to 1.6 mm/sec. The flow velocities referred in this paper is the linear flow velocities at the 200 μm x 200 μm NEA area calculated from the recorded videos (see supplementary videos files for details). Before performing DEP capture experiments, *E. coli* cells at a particular flow velocity were flowed through the channel for sufficient time to get rid of air bubbles and other particles to attain a uniform and stable flow. Figure 4.10a shows snap shot of the video as *E. coli* cells are flowing at 0.11 mm/sec through the channel when the voltage is turned off, where each cell appears as a stretched line. Green pseudocolor is used to represent the fluorescence emission.

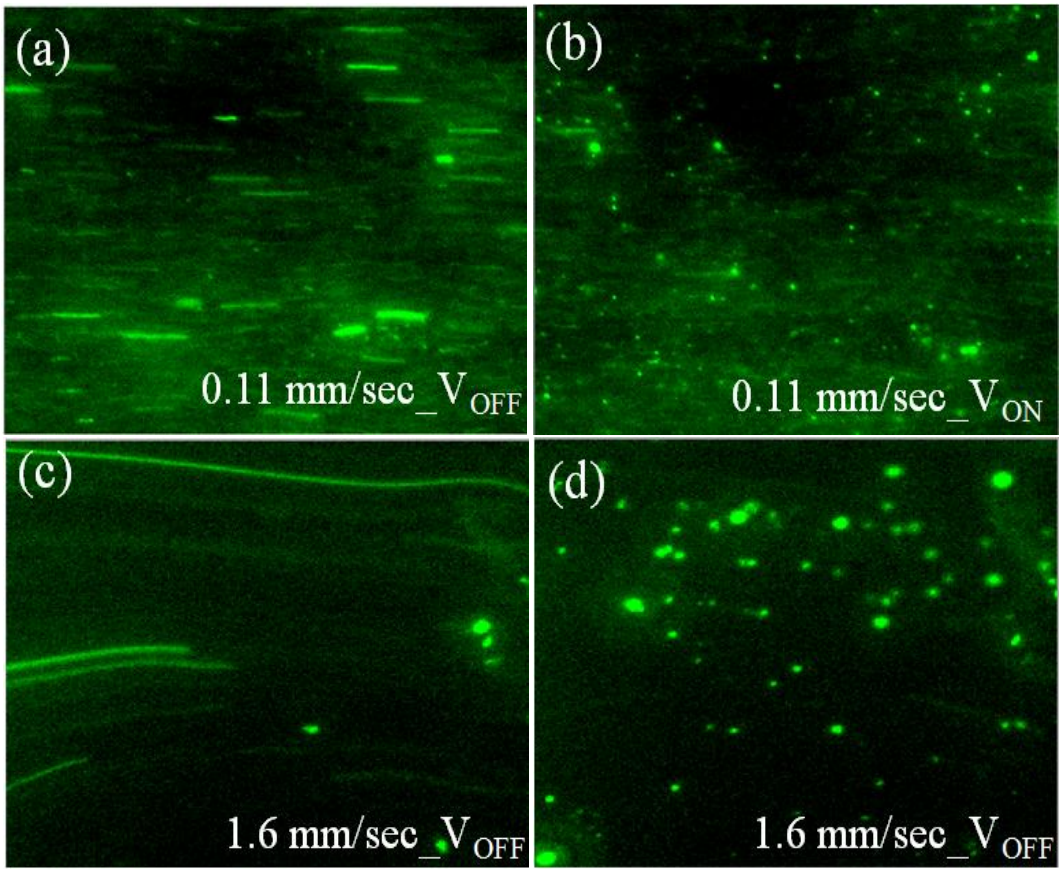

Figure 4.10 Images of *E. coli* cells before and after being captured at the CNF NEA with 100 kHz frequency and 10 V_{pp} AC bias. (a) and (c) Snap shots of *E. coli* cells flowing at 0.11 and 1.6 mm/sec flow velocities, respectively, in the DEP device when no voltage is applied. (b) and (d) Snap shots of *E. coli* cells captured at the exposed tips of CNF NEA by applying an AC voltage of 10 V_{pp} at 0.11 and 1.6 mm/sec flow velocities, respectively.

Almost immediately after the voltage is turned on, the stretched lines turn into bright round green spots at fixed positions as shown in Figure 4.10b, indicating that *E. coli* cells are captured at the tips of CNF NEA by pDEP. When the flow velocity is increased, *E. coli* cells experience a larger F_{DRAG} since F_{DRAG} is proportional to the flow velocity. As a result, less *E. coli* cells can be stably captured. Figure 4.10c shows a snap shot from a video of *E. coli* cells flowing at a flow velocity of 1.6 mm/sec when the voltage is turned-off. *E. coli* cells appear as much longer stretched lines due to the higher flow velocity as compared to that in Figure 4.10a. When the voltage is turned on, substantial number of *E. coli* cells are captured by pDEP at the NE tips as seen in Figure 4.10d. This indicates that the pDEP force is sufficient to attract many cells (likely those that are closer to the bottom NEA surface) toward the NEA. Once they are at the CNF tip, the lateral DEP force component is larger than the hydrodynamic drag force along the flow direction even at a high flow velocity of 1.6 mm/sec and thus is able to keep the *E. coli* cell at the surface.

Further analysis was carried out to show the capture kinetics at three different flow velocities. The number of bright spots at each time frame was counted during DEP capture experiments and plotted vs. time in Figure 4.11a. At the initial conditions at all three flow velocities almost no *E. coli* cell is trapped when no AC voltage is applied, the moment an AC voltage is applied, a sudden increase in the count of bright spots is seen, indicating the capture of *E. coli* cells at the NEA. The count remains almost the same during the time the voltage is applied. But the number of the bright spots clearly depends on the flow velocity. At a low flow velocity of 0.11 mm/sec, the count of bright spots is ~300 while it sharply drops to ~70 as the flow velocity is increased to 1.6 mm/sec. More details of the kinetic process to capture *E. coli* cells can be seen in real-time DEP videos at 0.11 mm/sec and 1.6 mm/sec flow velocities in supplementary videos. The flow velocity at 1.6 mm/sec is ~3 times higher than the maximum flow velocity of 0.5 mm/sec that is reported for a micro-points-and-lid device[155] and is at the high end of the typical range of the flow velocity (0.04-2 mm/sec) used in interdigitated micro-DEP device.[167]

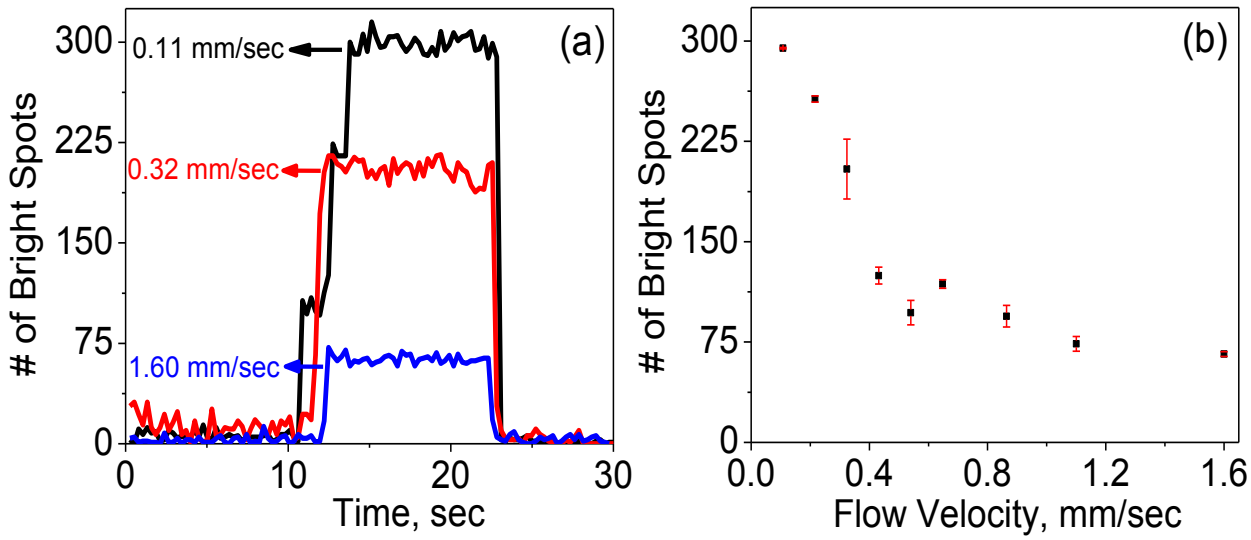

Figure 4.11 Quantifying *E. coli* cells captured at different flow velocities. (a) The change in number of captured *E. coli* cells (correlated to the number of bright spots counted) with respect to time at three different flow velocities (0.11, 0.32 and 1.6 mm/sec). DEP capture experiments are performed by applying an AC voltage of 10 V_{pp} at a frequency of 100 kHz. (b) The change in number of bright spots as a function of flow velocity as *E. coli* cells are flowing through the channel.

For stable capture of a particle, two sequential processes are involved. First, a vertical DEP force has to be strong to be able to quickly pull the particle to the NEA tip before it flows out of the active area. Second, the lateral DEP force F_{DEP} at the NEA tip has to overcome the lateral drag force F_{DRAG} by the lateral fluidic flow which depends on the flow velocity. The hydrodynamic drag force by the fluid to carry the particles with the flow in a microfluidic channel is defined by Stokes equation:[167]

$$F_{drag} = 6\pi k r \eta \upsilon_m \qquad \textbf{(4.3)}$$

where η is the dynamic viscosity of the fluid, υ_m is the velocity of the medium fluid at the center of the particle, and k (>1) is a nondimensional factor accounting for the wall effects. It should be noted that the value of υ_m is height-dependent since the fluid follows in a parabolic laminar flow profile with the highest velocity at the center and slowest velocity at the channel walls. In our results reported in this work, the flow velocity is calculated from the length of stretched lines in

the videos focused on the CNF NEA surface at the bottom of the microchannel, and thus it is the actual υ_m within the depth of field of the camera (~0.6 μm by the tutorial calculator at Carl Zeiss website) from the CNF NEA surface. The average flow velocity $<\upsilon_m>$ is ~2.78 mm/sec (see Appendix B), much higher than 2.0 mm/s used in the previous study.[131] From Equation 4.3, increasing the flow velocity clearly does not favor pDEP capture of the bacterial cells. However, many practical applications require rapidly isolating bacterial cells from a dilute solution, in which a high flow rate has to be used to obtain sufficient throughput. It has been very challenging to use pDEP for such applications. The pDEP force has to be increased to compete with the increased drag force. According to the DEP modeling study published earlier,[131] the square of the electric field strength at the NE tip is 200 times higher than that of the micro electrodes used in points-and-lid configuration. This provides a very high DEP force required to counteract the large drag force and capture *E. coli* stably at the CNF NEA. However, the experiments were carried out only at two average flow velocities, i.e. 0.25 mm/sec and 2.0 mm/sec. Here we show the systematic study at a series of surface flow velocities from 0.11 mm/sec to 1.6 mm/sec. It is convincing that pDEP capture of *E. coli* cells is effective at the flow velocity of 1.6 mm/sec or even higher.

The kinetic profiles of the fluorescent spots vs. time during pDEP capture of *E. coli* cells in our study can be interestingly compared with those in the previous study by Arumugam et al.[131] They found that, at low AC voltage amplitude (1-7 V_{pp}), there was a slow kinetic process which took seconds for the fluorescence intensity of captured *E. coli* cells to reach the saturated level. But it almost immediately jumped to the saturated level at a high AC voltage of 9 V_{pp}. The fast kinetic phenomena at 9 V_{pp} is consistent with our results in Figure 4.11a, all of which were measured at 10 V_{pp} AC bias. Interestingly, although the saturated level of the fluorescence counts varies with the flow velocity, none of the curves shows the slow kinetic process during which bacterial cells slowly accumulates when the AC voltage is turned on. It seems that pDEP action is accomplished instantaneously even at the highest flow velocity. The saturated level of the captured fluorescent spots is plotted vs. the flow velocity in Figure 4.11b. A monotonically decreasing curve is obtained as the flow velocity is increased. The trend is consistent with our discussion above.

Our long-term goal is to develop this technique as a rapid pathogen detection technique using handheld electronics. The fluorescence measurement needs to be replaced with simpler

electronic methods for detection. Impedance biosensors integrated with techniques like DEP, termed as DEPIM, are widely employed for rapid detection of pathogenic bacteria. DEPIM has been demonstrated to monitor the processes utilizing pDEP force to capture bioparticles on the electrode surface at a fixed AC frequency using real-time impedance measurements.[70] It can detect pathogenic bacteria both quantitatively and selectively at IDEs where the bacteria are trapped in between the electrode pair in a pearl chain fashion and the conductance change between the electrodes was monitored.[168-169]

To explore the feasibility of DEPIM with CNF NEAs, we carried out EIS measurements with 2.8 V_{pp} AC voltage bias before and after pDEP capture of *E. coli* cells. The Bode plots of EIS are shown in Figure 4.12. Figure 4.12a shows the |Z| value over the whole frequency range after pDEP performed at 10 V_{pp} in comparison with that without subjected to pDEP capture. Clear differences can be seen at frequencies below 100 Hz.

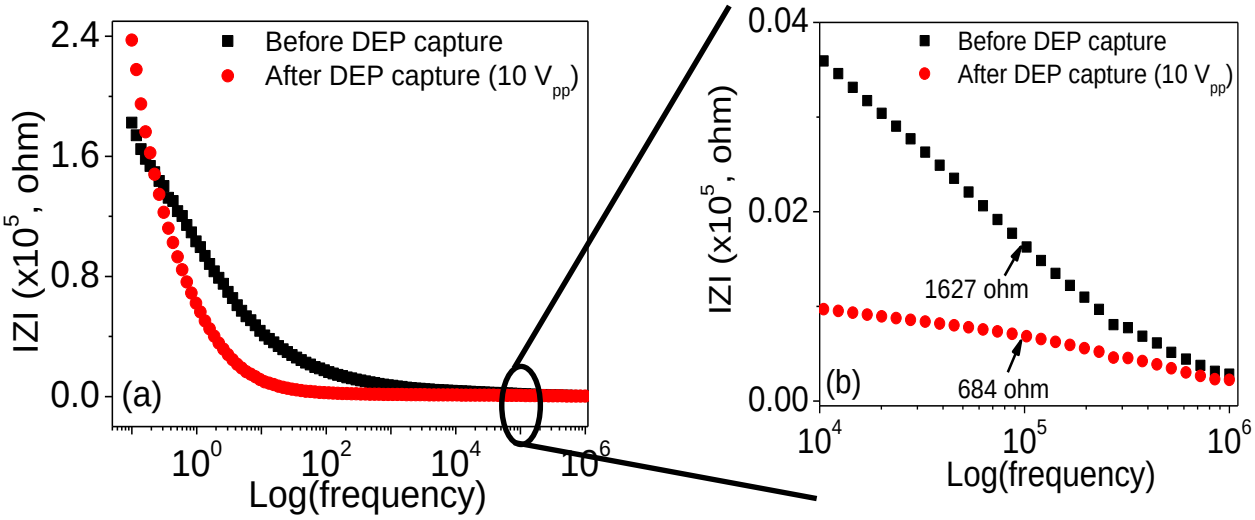

Figure 4.12 Variation of the electrochemical impedance spectroscopy (EIS) before and after bacterial cell capture. (a) The Bode plot of the EIS, that is the amplitude of |Z| vs. the logarithm of the AC frequency, recorded in an *E. coli* cell suspension in DI water before and after subjected to DEP capture at the exposed CNF tips by applying an AC potential of 10 V_{pp} at 100 kHz frequency. (b) An enlarged portion of the Bode plot to show impedance change at the frequency around 100 kHz in an *E. coli* cell suspension before and after subjected to DEP capture at the CNF NEA.

The enlarged plot in Figure 4.12b shows that, percentage of the change in the |Z| value at 100 kHz (the optimum pDEP frequency) is as large as that at low frequencies. The |Z| value of CNF NEA in *E. coli* suspension at 100 kHz is ~1627 Ω before pDEP bacterial capture. After running pDEP experiments to capture *E. coli* cells, the |Z| value decreases to ~684 Ω (by ~58%). The arrows in Figure 4.12b indicate the |Z| values at 100 kHz. Thus the decrease in the impedance may be likely because the large (1-2 μm in size) and more conductive bacterial cells that are in direct contact with the small CNF tips (~100 nm in dia.) which is equivalent to increasing the electrode size. The results in this study serve as a reference of the maximum change that one can obtain to reach the saturated bacterial capture.

4.7 Conclusions

In summary, a brief theory behind the concept of dielectrophoresis was presented. Multi-shell smeared-out model can be readily used for the prediction of effective permittivity and CM factors for complex bioparticles like *E. coli* cells and vaccina virus. Then a theoretical prediction of CM factor and DEP force at different medium conductivities for *E. coli* and vaccine virus was discussed. We demonstrated effective pDEP based capture of *E. coli* cells from a high-velocity flow at the exposed tips of an embedded CNF NEA. The CNF NEA is placed at the bottom of a microfluidic channel vs. a large transparent ITO-coated glass at the top with 20 μm spacing in between to form a "points-and-lid" configuration. Our results have confirmed the observations in a previous report using such nano-DEP device. More importantly, we found that the optimum frequency of the AC voltage is around 100 Hz, much lower than 1 MHz used in the previous study. *E. coli* cells can be captured in a selected area by lithographically defining a window on the CNF NEA chip. The total quantity of captured *E. coli* cells is found to decrease monotonically as the flow velocity is increased. Interestingly, the fluorescence signal representing the captured *E. coli* cells immediately jumps to the saturated level at all flow velocities once a 10 V_{pp} AC bias is applied. No kinetic accumulation is observed at such a high-voltage bias. EIS before and after capturing *E. coli* cells show clear changes over the whole frequency range. Particularly, the |Z| value at 100 kHz (i.e. the optimum pDEP operation condition) is decreased by ~58% after cell capture. Therefore, it is highly feasible in future studies to use real-time impedance (i.e. DEPIM) for directly monitoring the process during pDEP capture of bacterial cells.

Chapter 5 - Luminol Decorated Gold Nanoparticles (GNPs) as a Sensitive Chemiluminescence (CL) Biosensor for Trace Blood Detection

Provision patent No. 61/595,958 (A Nanoparticle-functionalized Chemiluminescent Method for Biosensing, by Lateef U. Syed, Jun Li, Judy Wu, and Mark Richter) was filed on Feb. 7th, 2012.

Reproduced partly from "An Ultrasensitive Chemiluminescence Method for Trace Blood Detection Using Luminol-Labeled Gold Nanoparticles" Syed. L. U.; Rochford. C.; Wang. F.; Wu. J.; Richter. M.; Balivada. S.; Troyer. D.; Li. J. manuscript in preparation.

5.1 Introduction

CL is a process in which visible light is emitted as a result of chemical reactions. CL is a much more sensitive and convenient analytical technique than commonly used fluorescence methods due to high quantum yield, no need of exciting light sources, and low background.[170] It has been widely utilized for forensic investigations by spraying luminol (5-amino-2,3-dihydro-1,4-phthalazine-dione) and hydrogen peroxide to identify dried blood stains.[171-172] CL catalyzed by luciferase is also used in pyrosequencing, one of the most successful DNA sequencing techniques.[172] In this chapter, we will discuss our study to improve luminol based CL by covalently attaching luminol molecules onto gold nanoparticles (GNPs) that are protected by a monolayer of carboxylic acid terminated alkane thiols. Using GNPs as high-surface carriers, manipulation and binding of luminol moieties to desired locations were made easier. In addition, the absorption or colorimetry of GNPs may serve as an additional signal modal for analytical measurements.

GNPs have gained considerable attention in the past few decades due to their unparalleled optical, electronic, physical, and chemical properties.[173-175] The ease of surface modification of GNPs with alkane thiol molecules[176-179] and further covalent linking with other biological moieties makes GNPs an attractive choice for biosensor applications. Modifying GNPs with a particular DNA probe or an antibody has become a common practice for developing affinity based biosensors. In addition, GNPs present strong size-dependant surface

plasmon resonance. This makes them ideal sensors for colorimetric or absorption detection of DNA, amino acids, and proteins, by specific binding with another recognition element in bulk solution or immobilized on a substrate.[77-78, 80, 180-183] The detection limit for nucleic acids based on GNP aggregation varies in a large range, with the lowest reported at ~33 zmol (2.0×10^4 target molecules).[184] The GNPs in such detection may be much more than target molecules. Here, we demonstrate that CL from luminol molecules carried by GNPs can be detected with as low as ~1,000 GNPs.

Luminol belongs to the family of heterocyclic hydrazide compounds, and is by far one of the most popular agents for CL applications.[185-188] The concept of light production by luminol catalyzed by Fe^{3+} ions released from red blood cells is the basis of forensic and hospital analysis of blood contamination.[30, 171, 189] When GNPs are added to a solution containing luminol and ferricyanide ($Fe(CN)_6^{3-}$), they may inhibit the CL signal of luminol due to quenching if the diameter is less than 5 nm or enhance it due to catalytic effects if d is ~25-38 nm).[190-191] The effect of GNPs was found to be minimum with 5-10 nm diameter.[190-191] However, in one study, CL signal was reduced by ~5.0 fold with luminol covalently attached to 30 nm GNPs compared to that in solution.[192] The mechanism of these effects remains to be understood.

In general, electron transfer may facilitate catalytic effects while energy transfer to GNPs may cause nonradiative deactivation (quenching) of chemically excited luminol products. To avoid the complication, we chose to use 10 nm-diameter GNPs in this study, where GNPs only serve as nanocarriers with a large surface-to-volume ratio for ease of manipulation of luminol molecules. In addition, the surface of GNPs is protected with a close-packed self-assembled monolayer of long-chain thiol linker, mercaptoundecanoic acid (MUA), to minimize both electron transfer and energy transfer between luminol and the GNP. This allows us to assess whether the surface-functionalized luminol can generate CL as efficiently as in bulk solution, which was an issue in previous studies.[192-193] Using this design, we have observed very strong CL from luminol-attached GNPs and found that the CL intensity increased linearly on the logarithmic scale with the number of GNPs over 7 orders of magnitude. We measured CL with as small as ~1,000 luminol-labeled GNPs. Using this method, we were able to detect sheep blood samples after 10^8 fold dilution from the stock solution.

5.2 Experimental details

5.2.1 Materials and reagents

Citrate protected GNPs (8.0-12.0 nm in diameter), and mercaptoundecanoic acid (MUA) were purchased from Sigma Aldrich. Luminol (LUM), EDC, NHS, Tween 20, potassium ferricyanide ($K_3Fe(CN)_6$), PBS, sodium hydroxide (NaOH), and hydrogen peroxide (H_2O_2) were obtained from Fisher Scientific. Polydimethylsiloxane (PDMS) was ordered from Dow Corning. All chemicals used in this study were analytical grade. DI water was used in all the experiments.

5.2.2 Multiwell fabrication for blood experiments

A polydimethylsiloxane (PDMS) test strip ~1 mm thick was fabricated on a glass slide using a fixture shown in Figure C.1a. A 20:1 ratio of PDMS and curing agent respectively was mixed and cured at ~60 ^{o}C for 20 min. An array of oval shaped holes (~4 mm x 3 mm) was punched through the PDMS that can hold ~12 µl volume of solution for CL experiments.

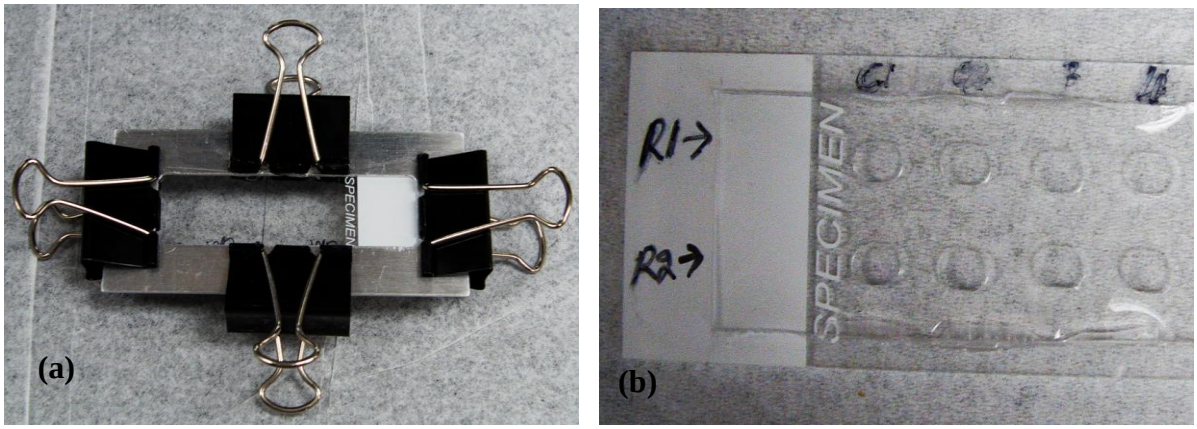

Figure 5.1 (a) Fixture used to fabricate PDMS test strip for chemiluminescence experiments. (b) Test strip with holes punched in the PDMS.

5.2.3 Blood sample preparation

Whole sheep blood was obtained from HemoStat Laboratories (Dixon, CA). The concentration of the sheep red blood cells in the stock blood solution was measured as ~$4.6x10^9$ cells/ml using Petroff Hausser counting chamber under an upright optical microscope (AxioSkop II, Carl Zeiss), as shown in optical image (Figure 5.2a). The received blood sample was stored at

~4°C. Before CL experiments, the sample was inspected under an optical microscope, to make sure that the cells were intact. In the experiments using lysed cells, 100 μL blood samples were frozen at -20°C and thawed on ice before use. This resulted in complete cell lysis (see Figure 5.2b). Also, UV-Visible study of lysed and unlysed RBCs was done, which further confirmed that the freeze-thaw of RBCs indeed lyse them (see Appendix Figure C.1)

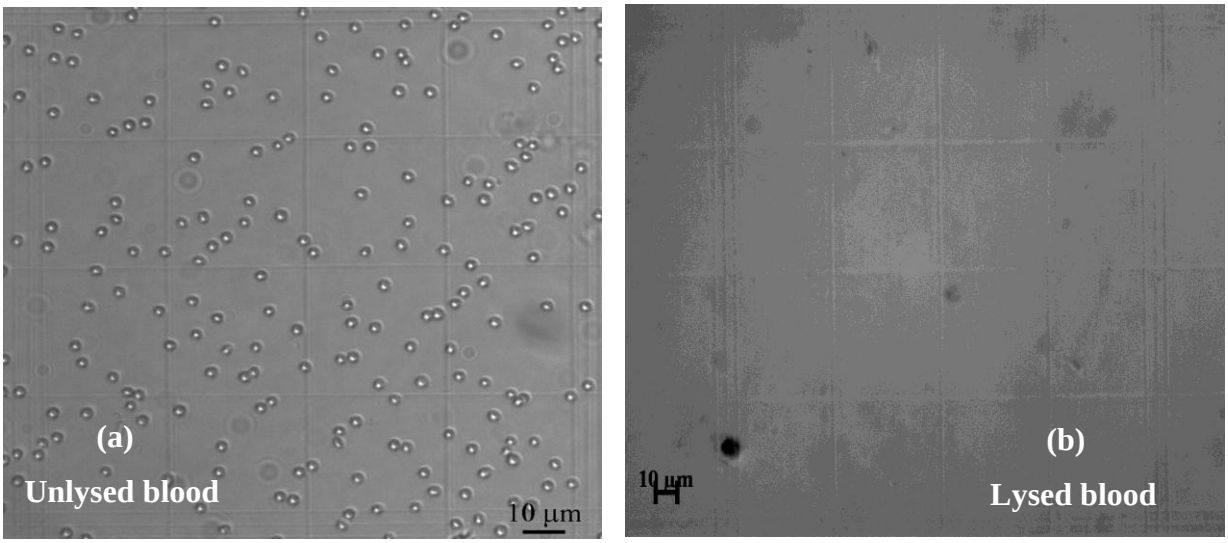

Figure 5.2 (a) Bright field image of unlysed 10X diluted sheep blood on a Petroff-Hausser counting chamber. The RBCs are ~3-4 μm in size. (b) Bright field image after lysing RBCs using freeze-thaw method.

5.2.4 Characterization instruments

UV-visible absorption spectra were recorded using Beckman DU640 spectrophotometer in a 360 μL microcuvette with an optical path length of 10.0 mm. Infrared spectroscopy (IR) was performed on a Nicolet 380 FT-IR spectrophotometer with neat solid samples in transmission mode. Transmission electron microscopy (TEM) measurements were carried out using FEI Tecnai F20 XT field emission system.

5.2.5 Modification of GNPs with chemiluminescent luminol

The initial step was to exchange the citrate groups with the MUA ligand on the surface of GNPs under the protection of the nonionic surfactant Tween-20. Typically, 2 ml of citrate-protected GNP stock solution (5.99×10^{11} particles/ml) was transferred in a clean, dry test tube

with a screw-cap followed by addition of 2 ml of 1X PBS with 0.2 mg/ml Tween-20 buffer (the same buffer composition was used for all following steps during functionalization). The mixed solution was incubated at room temperature (RT) for 30 min before 2 ml of 3.0 mM MUA solution (in 1:3 ethanol/DI water) was added. The solution was further incubated overnight at RT with gentle shaking. The mixture was centrifuged at 14,100 rpm for 20 min to pellet the MUA-covered GNPs (GNP-MUA). The supernatant was discarded and the pellet was re-suspended in the buffer. The pellet was washed three more times before the final suspension in the buffer. MUA modified GNPs (200 µl) were then reacted with 100 µl of freshly prepared aqueous solution of 50 mM EDC and 50 mM NHS for 15 min. This mixture was then combined with 100 µl of 50 mM LUM solution (a few drops of 0.4 M NaOH were added to increase the solubility of LUM in DI water) and incubated at RT for 2 h. Finally, the LUM-modified GNPs (GNP-MUA-LUM) were washed 3 times with buffer and finally suspended in the buffer solution to obtain a final concentration of ~$1x10^{12}$ GNP/ml.

5.2.6 CL measurement

CL experiments were carried out using a IVIS Lumina II system (Caliper Life Sciences, CA), which utilizes a highly sensitive, -90^{o}C cooled, and back illuminated CCD camera as the detector. A layer of PDMS of ~1.5 mm in thickness was laid on a glass microscope slide (3" x 1" x 1 mm) in which an array of oval shaped holes (3 mm x 4 mm) was punched through to form CL reaction wells of ~12 µl in volume. The GNP-MUA-LUM solution was dropped in the well and dried before CL measurements. Each well contained a known number of luminol modified GNPs. Typical CL experiments involved mixing 4 µl of 0.033 M NaOH, 4 µl of 0.47 M H_2O_2, and 4 µl of 1 mM $Fe(CN)_6^{3-}$ solution or, in some experiments, blood samples (at varied concentrations) in different PDMS wells. The slide was then quickly placed in the light tight black box of the IVIS Lumina II system. A bright field reference photograph was first recorded using the CCD camera (this process takes ~3 sec), and then the CL signal (Photon flux) was recorded in the kinetic mode (i.e. flux of photons vs. time) with an exposure time of 10 sec to the CCD camera. The CL signal is represented in a pseudocolor image by overlaying the bright-field and CL images. The elapse between consecutive CL snap shots in the kinetic mode is approximately 13 sec (i.e. 3 sec for reference photograph, and 10 sec to collect CL signal).

Normally, 10 such CL snapshot images were taken and the integrated photon flux over the designated PDMS well was plotted vs. time.

5.3 Results and discussion

5.3.1 GNPs modification and characterization

The two-step strategy to functionalize luminol on GNPs and the scheme of using such functionalized GNPs for detecting Fe^{3+} containing analytes are illustrated in Figure 5.3. In the first step, the citrate ligand, which was used to stabilize GNP colloid in the starting material, was replaced with MUA by ligand exchange. This process produced a self-assembled monolayer of MUA on each GNP through stronger Au-thiol interaction, yielding carboxylic acid (-COOH) terminal groups at the exterior surface. In the second step, the MUA derivatized GNP colloid was reacted with luminol in the presence of EDC and NHS, which facilitated the covalent binding of luminol onto the GNPs via an amide bond formed between the -COOH group of MUA and the $–NH_2$ group of luminol.

The product is labeled as *compound A* (i.e. GNP-MUA-LUM) in Figure 5.3. UV-vis, IR, and HRTEM measurements were employed at each stage of modification to confirm physical and chemical changes occurring at the surface of the GNPs.

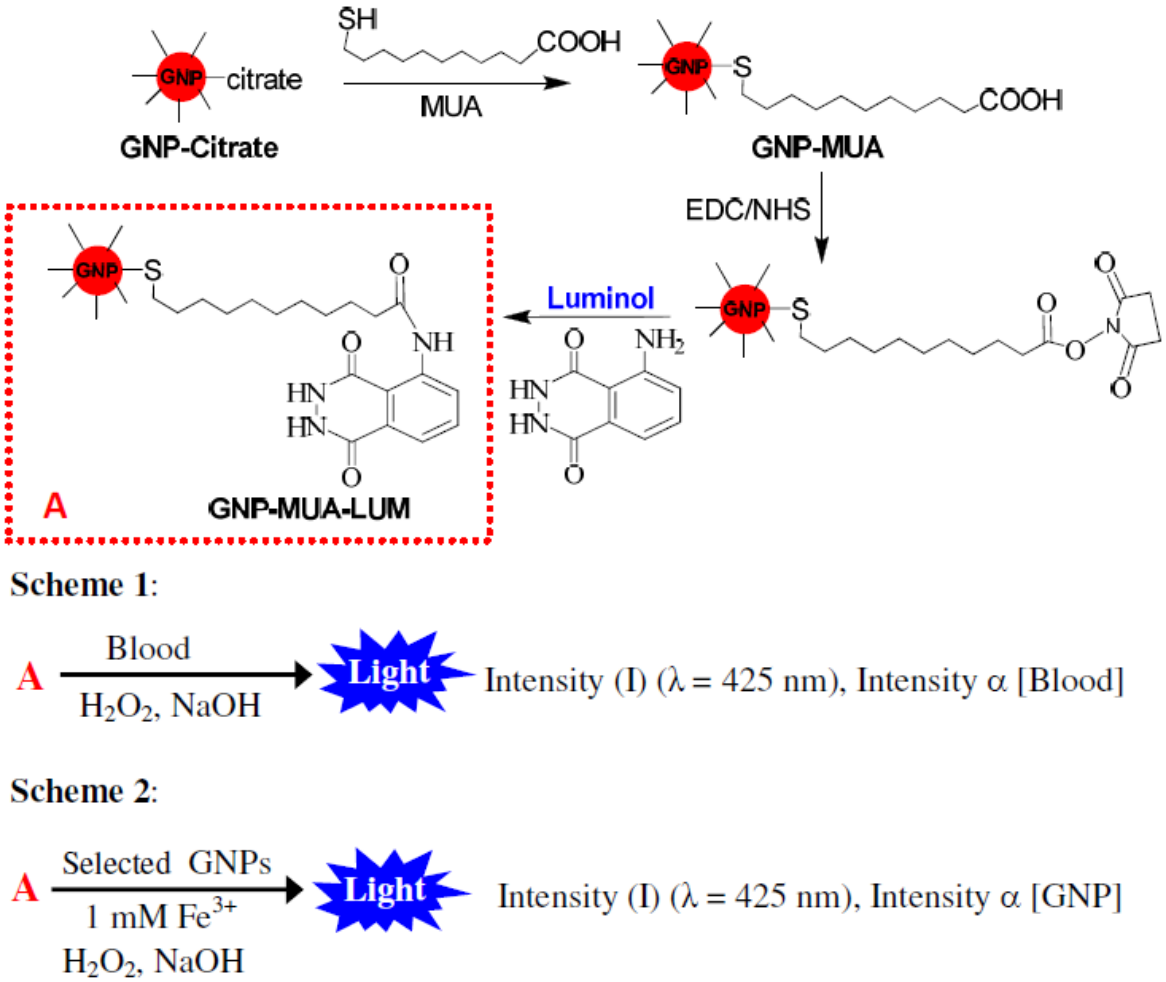

Figure 5.3 Schematic of the two-step modification of gold nanoparticles (GNPs) with luminol (LUM): ligand exchange of citrate with mercaptoundecanoic acid (MUA) and amide formation between the –COOH group in MUA and $–NH_2$ group in LUM. Two schemes to implement luminol-labeled GNPs (compound A) for analytical applications are illustrated: Scheme 1– to detect analytes (such as red blood cells) which can catalyze the CL reaction in presence of sufficient amount of A and required reagents (H_2O_2 and NaOH); Scheme 2 – to detect selected amount of A by supplying sufficient Fe^{3+} catalyst and required reagents (H_2O_2 and NaOH).

5.3.1.1 UV-visible absorption characterization of modified GNPs

The UV-visible absorption spectra in Figure 5.4 show the GNPs with different functional moieties at each stage, i.e. GNP-citrate, GNP-MUA, and GNP-MUA-LUM. Strong absorption

peaks were observed for all GNPs at ~516 nm, corresponding to the SPR. The full-width-half-maximum in the case of GNP-MUA and GNP-MUA-LUM is slightly larger than that of the GNP-Citrate. But the wavelength at the peak absorption of the GNP solution remains the same (as indicated by the deep red color shown in inset of Figure 5.4). These data indicate that the particle size remains similar as it goes through the ligand exchange and luminol functionalization processes. For GNP-MUA-LUM, however, there is an additional small, but noticeable peak at 347 nm, which corresponds to one of the absorption peaks of the luminol. UV-Visible absorption spectrum of pure luminol is shown in Appendix Figure C.2.

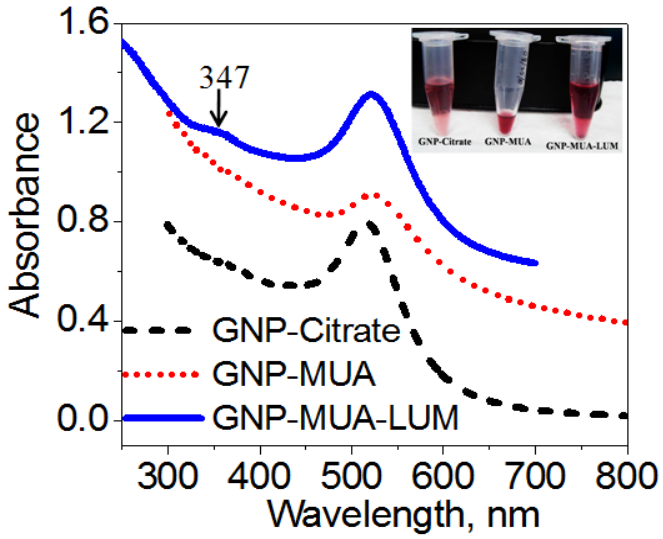

Figure 5.4 UV-visible spectra of citrate-stabilized GNPs (big dots), MUA modified GNPs i.e. after replacing citrate with MUA (small dots), and LUM attached GNPs (solid line). The small peak at 347 nm in the solid curve corresponds to an absorption peak of LUM. The GNP-MUA and GNP-MUA-LUM curves were translated upward by 0.2 and 0.5 units, respectively, along the y-axis for better comparison.

5.3.1.2 TEM characterization of modified GNPs

TEM images shown in Figure 5.3 further confirm that the shape and size of the GNPs before and after the modification have not been altered.

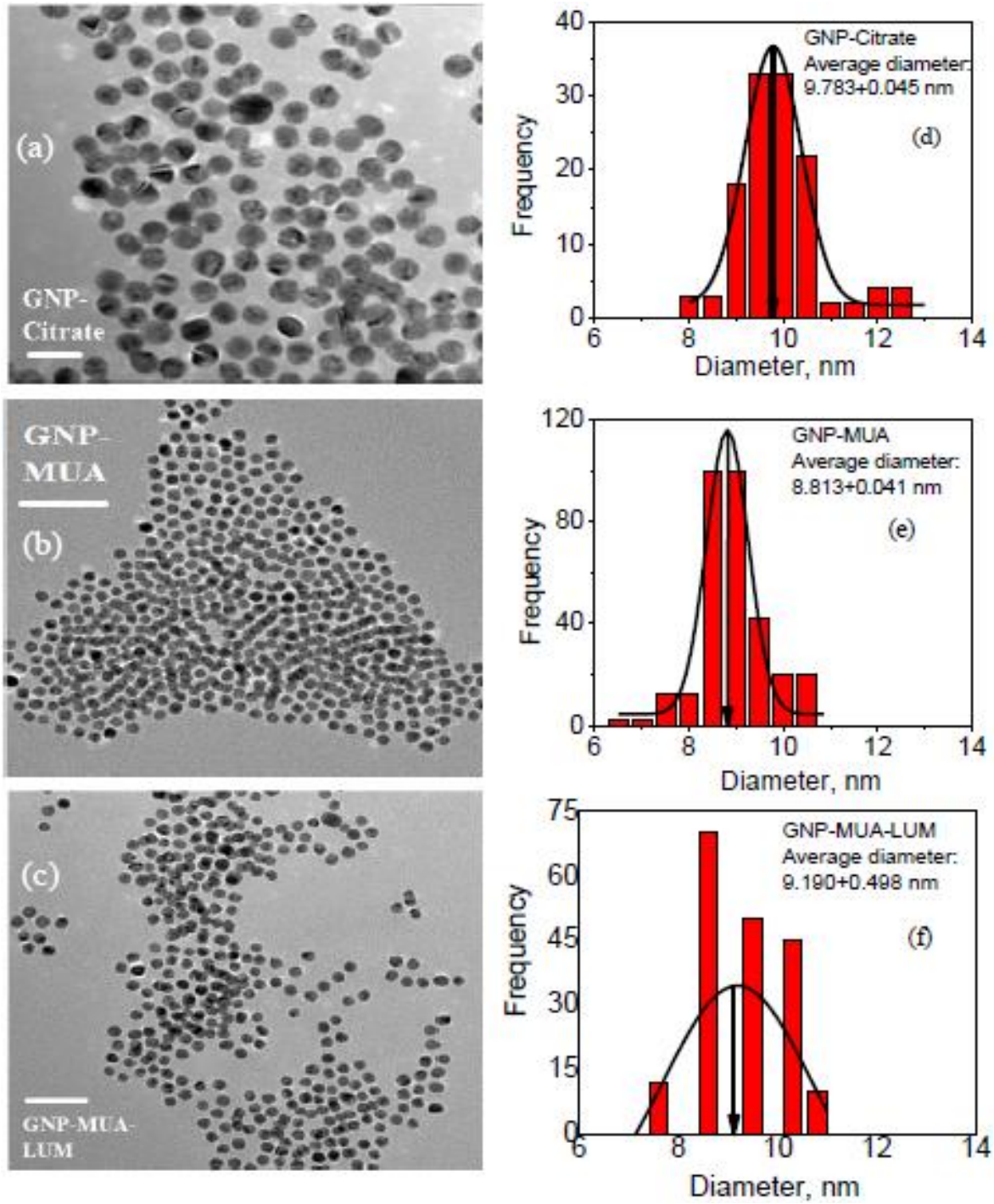

Figure 5.5 TEM images of GNPs with citrate protection (a), after MUA exchange (b), and luminol functionalization (c). The scale bars for (a)-(c) is 20, 50, and 50 nm, respectively. (d)-(f) show the size distribution of GNPs in (a)-(c). The average diameter of citrate stabilized, MUA exchanged, and luminol modified GNPs is ~9.8, ~8.8, and ~9.2 nm, respectively.

The average diameter of citrate-stabilized GNPs was found to be ~9.78 ±0.05 nm, in good agreement with the average size of 10 nm and a range distribution between 8.0 and 12.0 nm as certified by the vendor. After ligand exchange and luminol functionalization, the measured size of GNPs changed to ~8.81±0.04 nm and ~9.2±0.5 nm, respectively, within the size range of 8.0-12.0 nm, and no noticeable aggregation was observed.

5.3.1.3 FT-IR absorption characterization of modified GNPs

After ligand exchange and luminol functionalization steps, the GNP samples (including the starting GNP-citrate) were dried at room temperature and characterized with FT-IR. Figure 5.6 shows the FT-IR spectra of neat solid GNPs at different steps of functionalization. For MUA modified GNPs, the characteristic IR absorption peaks can be clearly seen at 2919 and 2849 cm^{-1}, which can be ascribed to the vibrational stretches of $–CH_2–$ functional groups in the MUA chain.[194] A peak corresponding to the C=O stretch in the terminal carboxylic acid group of MUA is expected at ~1700 cm^{-1}, but it was shifted to ~1550 to 1610 cm^{-1} for GNP-MUA and split between 1600 to 1730 cm^{-1} for GNP-MUA-LUM. This indicates that the carboxylic acid group in GNP-MUA presents in the ionized form (i.e. as carboxylate salts)[195] since the pH value of the suspension solution is ~7, above the pKa of general –COOH groups. The IR absorption at 1600 to 1730 cm^{-1} in GNP-MUA-LUM is consistent with the formation of amide bonds between the –COOH group in MUA and the $–NH_2$ group in luminol.[196] Also, a peak at 1396 cm^{-1} corresponding to the bending of C-H bond in the long alkane chain can be seen in GNP-MUA. The peaks corresponding to the C-H stretch of $–CH_2–$ in the alkane chain were observed at 2913 and 2864 cm^{-1} in GNP-MUA-LUM, confirming that the MUA monolayer was intact after LUM functionalization. The N-H stretch mode of luminol, which is expected to be at 3,300 to 3,500 cm^{-1}, however, was buried under the strong background absorption by GNPs. Overall, the FTIR spectra confirmed that the ligand exchange to replace citrate with MUA and functionalization of LUM to MUA were successful following the schemes shown in Figure 5.3.

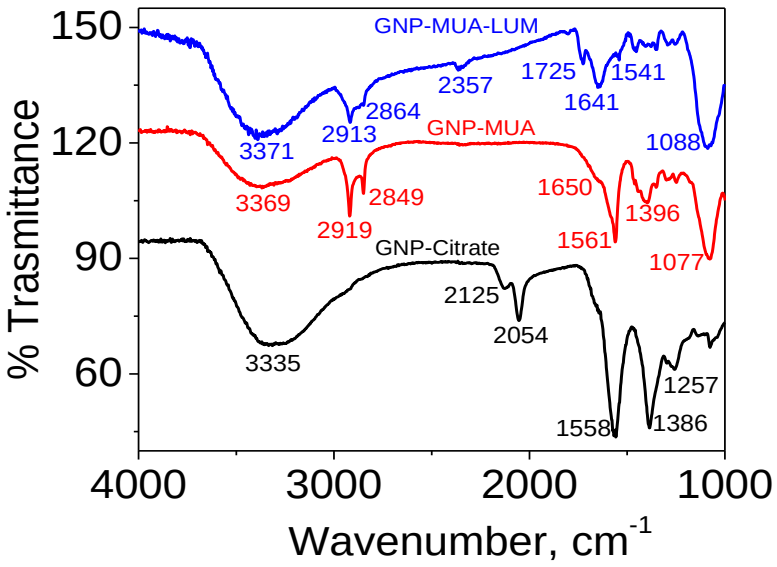

Figure 5.6 FT-IR spectra of citrate-stabilized GNPs (black curve), MUA modified GNPs after replacing citrate (red curve), and LUM attached GNPs (blue curve). The GNP-MUA and GNP-MUA-LUM curves were translated upward by 20 and 50 units, respectively, along y-axis for better presentation.

5.3.2 CL Assessment

After functionalizing GNPs with CL luminol molecules, the concentration of the stock solution was adjusted such that a 10 µl solution dispensed ~$1x10^{10}$ GNPs. This was used in a series of dilutions to obtain GNP-MUA-LUM solutions at concentrations varying over 8 orders of magnitude. The PDMS wells on the test strip were loaded with a 10 µl solution of respective concentration and dried in the incubator before CL measurements. Figure 5.7a and Figure 5.7b include representative snapshot CCD images of CL signals recorded during the CL measurements from the PDMS wells loaded with $1x10^{10}$ and $1x10^{3}$ GNP-MUA-LUM, respectively. Complete CL images are shown in Appendix Figure C.3 from the PDMS wells loaded with the LUM-labeled GNPs from $1x10^{10}$ to $1x10^{3}$ particles/well. Photons were emitted immediately upon addition of the premixed solution consisting of 4 µl of NaOH (0.033 M), 4 µl of H_2O_2 (0.47 M), and 4 µl of $Fe(CN)_6^{3-}$ (1.0 mM) to the PDMS wells. The region of interest (ROI) in the image was selected over the specific PDMS well using the IVIS Lumina II system software and the photon counts was integrated over this region.

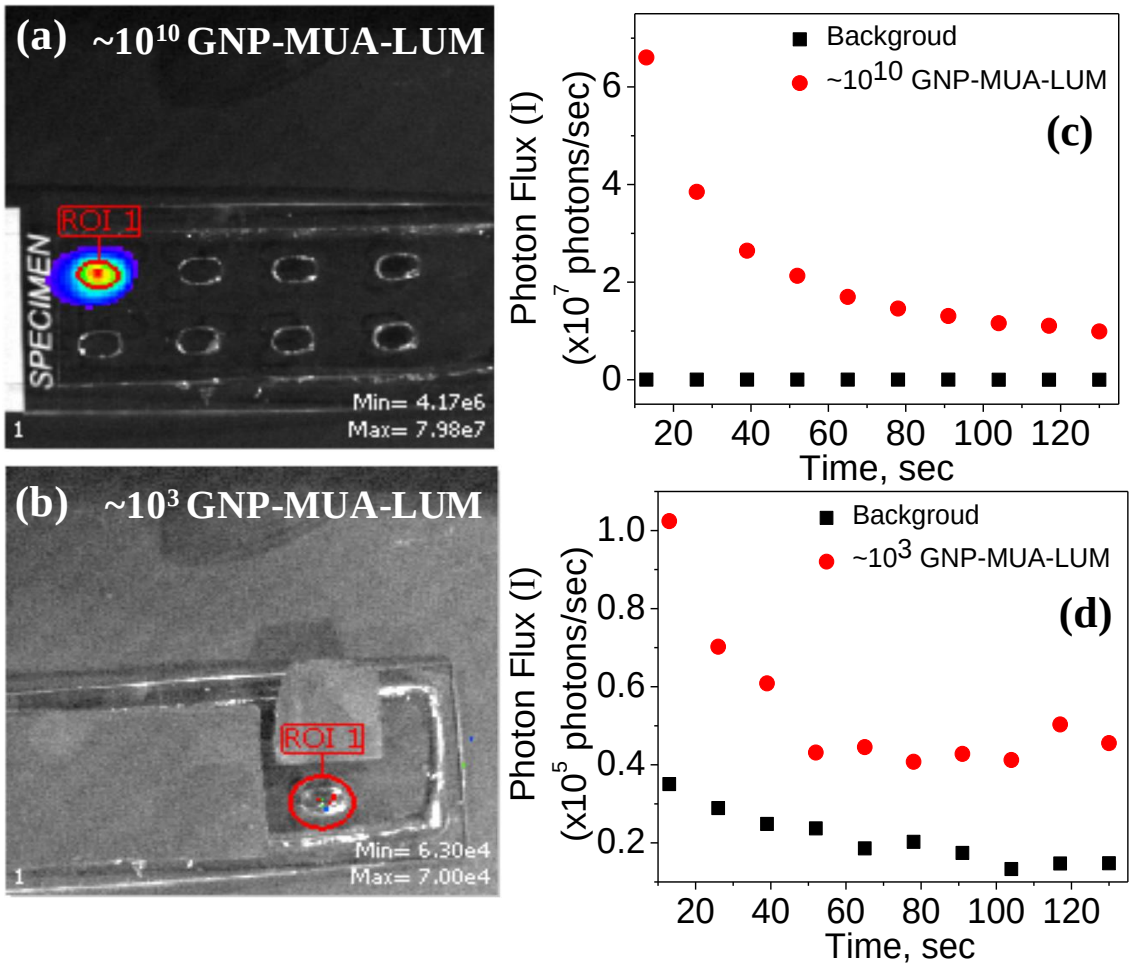

Figure 5.7 CL signal recorded using IVIS Lumina II. (a) and (b) are snapshot images using psuedocolor to represent the CL intensities from two designated PDMS wells on a glass slide, which are loaded with ~1x10^{10} and ~1x10^{3} GNP-MUA-LUM, respectively. (c) and (d) show plots of integrated CL signal (filled circles) from the wells containing ~1.0x10^{10} and ~1.0x10^{3} GNP-MUA-LUM over background signal (filled squares) obtained in control experiments without $Fe(CN)_6^{3-}$ ions.

CL of luminol is known to follow a flash mechanism in which CL occurs immediately and then decays quickly.[31] The half-life strongly depends on the experimental conditions.[171] It can be seen in Figure 5.7c and Figure 5.7d, that the integrated CL signal (filled circles) has the maximum value at the first snapshot image for the PDMS wells loaded respectively with 1x10^{10} to 1x10^{3} luminol labeled GNPs. The data sampling rate was limited by the imaging speed at ~13 s/frame. The CL signal decayed exponentially with time as shown in Figure 5.7c and Figure

5.7d. Nevertheless, the CL signal from $1x10^3$ luminol-labeled GNPs clearly remained above the background (filled squares) which was recorded by replacing the 1.0 mM $Fe(CN)_6^{3-}$ solution with DI water while all other experimental settings were kept the same. The half life is about 30 seconds for both $1.0x10^{10}$ to $1.0x10^3$ luminol labeled GNPs, indicating that the CL mechanism remained the same over such a large range.

In the experiment with the lowest number of luminol labeled GNPs (i.e. ~1,000 GNPs), the total number of CL photons was comparable to the estimated number of luminol molecules (~$1.4x10^3$ luminol/GNP) by assuming the formation of a close-packed thiol monolayer with the same density as on a flat gold surface. But the large variation in the measurement value limited the assessment of exact value of CL quantum yield of the attached luminol molecules. In an alternative approach, the CL signal measured with $1.0x10^{10}$ luminol-labeled GNPs was compared with that from the same number of free luminol molecules that were dispersed in solution (4 μL of 23 μM of luminol in each PDMS well) with all other parameters the same. As shown in Appendix Figure C.4, the maximum CL signal from GNP-MUA-LUM is about ~37% of that from the luminol solution. The reduction factor is ~2.7, much smaller than the 5.0 times reduction in the previous study using 30 nm diameter GNPs through a much shorter linker (3-mercaptopropionic acid).[192] If the absorption of the CL photons by GNPs is considered, the difference between luminols attached to GNPs and those freely dispersed in solution in our measurements is even smaller. This is probably why ultrahigh sensitivity was obtained in this study. The mechanism of CL on luminol-labeled GNPs and the size effect of GNP are certainly worth further study. Due to the fast decay in the CL signal, it is necessary to use the signal from the first snapshot (i.e the maximum CL signal I_{max}) instead of the average signal for quantitative analyses.

Figure 5.8 shows a calibration curve in which the background subtracted maximum CL signal (ΔI_{max}) is plotted vs. the number of luminol-labeled GNPs in a PDMS well.

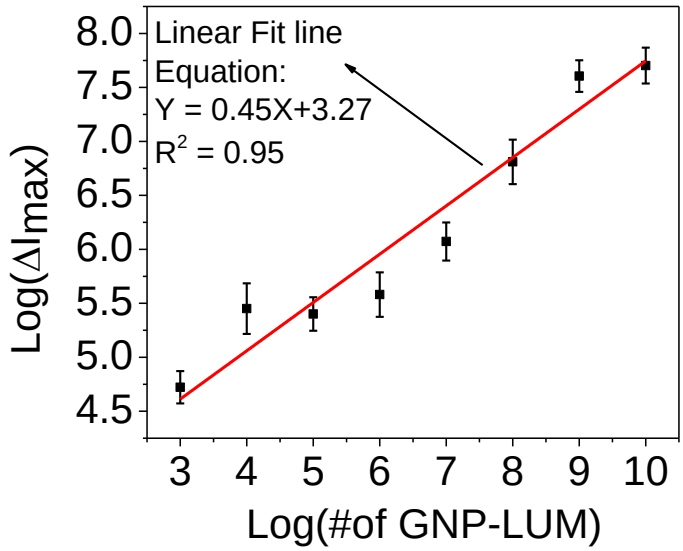

Figure 5.8 Calibration curve on a Log-Log scale of ΔI_{max} (background subtracted peak CL intensity from kinetic measurements) vs. the number of luminol modified GNPs. The solid line is the linear fitting line.

A linear relationship between the CL signal and the number of GNPs was obtained from $1x10^3$ to $1x10^{10}$ GNPs as:

$$Log(\Delta I_{max}) = 0.45Log(N_{GNP}) + 3.27 \quad \textbf{(5.1)}$$

with a R^2 value of 0.95, where N_{GNP} is the number of GNPs placed in the PDMS well. Even though CL signal from 1,000 GNPs can be clearly observed with ΔI_{max} = ~$5.0x10^4$ photons/s (see Figure 5.7d), the rigorous statistical detection limit depends on the standard deviation of the CL measurements with blank samples (with s_{blank} = $1.9x10^4$ photons/s). Following the convention, the signal at the detection limit needs to be:

$$I_{DL} = I_{blank} + 3s_{blank} \quad \textbf{(5.2)}$$

where the background signal I_{blank} is ~$2.4\ x10^4$ photons/s. Therefore, the statistical detection limit is derived to be ~2,600 GNPs. This can be improved by reducing the variation of

the background reading which was due to the variation in the experimental setting and the drift of the CCD camera.

The CL signal should be, in principle, proportional to the concentration of the luminol. However, the relationship between the background-subtracted maximum CL signal (ΔI_{max}) and the number of luminol-attached GNPs (N) was $\Delta I_{max} \propto N^{0.45}$ instead of a linear relationship as $\Delta I_{max} \propto N$. This might be due to luminol molecules being attached to the surface of GNPs which were deposited at the bottom of the well. It is a pseudo-two-dimensional system instead of the usual dispersion in bulk solution. The mechanism is worth further investigation.

GNPs are known to present strong SPR, which has been widely utilized to enhance the sensitivity in colorimetric or optical absorption methods.[78, 147] Our results suggest that CL can provide even higher detection sensitivity. To compare CL with absorption approaches, Figure 5.9 shows the UV-visible absorption spectra of GNP-MUA-LUM measured with 350 μl solution in a microcuvette of 10.0 mm optical path length. The total number of GNPs is varied from $1x10^{10}$ to $1x10^{3}$. At high concentrations (≥ ~$1x10^{8}$ GNPs), it shows a strong absorption peak at 518 nm, corresponding to the SPR of GNPs of ~10 nm in diameter. However, the absorption is below the baseline noise as the number of GNPs is at or below $1x10^{7}$. Also, the red color associated with the GNPs is only visually observable with naked eyes when the number of GNPs is more than ~$1x10^{9}$. The height of the absorption peak at 518 nm is fitted and plotted against the number of GNPs in the solution in Appendix Figure C.5. Clearly, the peak absorbance varies linearly with the number of GNPs when it is near or above $1x10^{8}$, but quickly drops below the detection limit when it is less than $1x10^{8}$.

In contrast, the CL signal using luminol-labeled GNPs can be easily observed with as few as 1,000 GNPs (Figure 5.7d), making this approach particularly useful for affinity biosensors based on Scheme 2 illustrated in Figure 5.3 in which the CL signal depends on the number of luminol-labeled GNPs captured through a co-functionalized recognition probe.[197-198] *To our knowledge, this is the first experimental demonstration that the detection sensitivity can be enhanced by at least 10^{4} times by using CL of luminol-labeled GNPs as compared to the optical absorption of GNPs.*

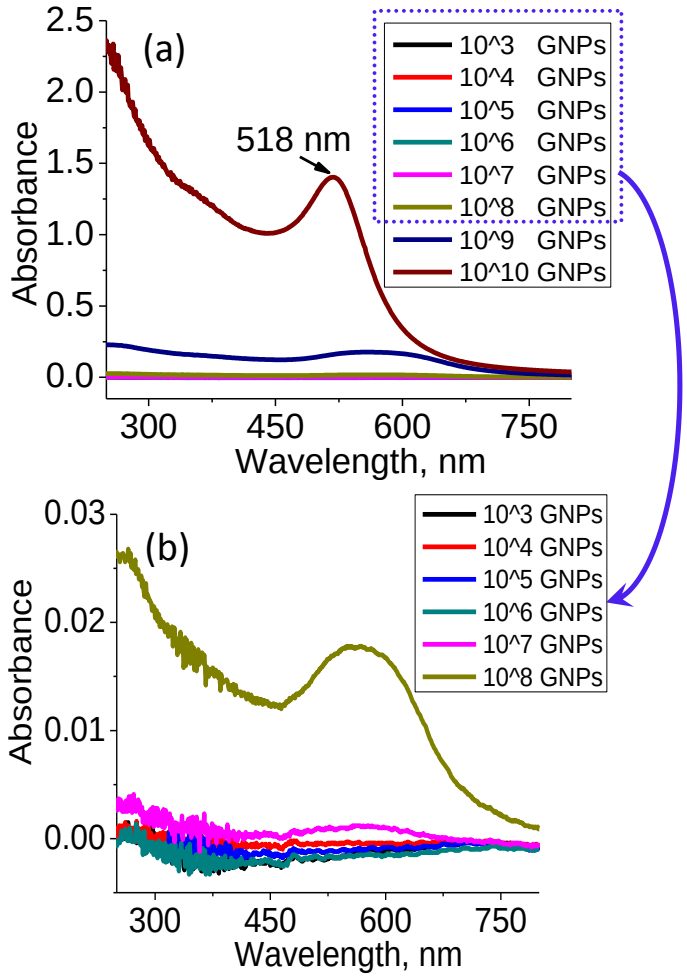

Figure 5.9 (a) The UV-Visible absorption spectra measured with varying number of GNP-MUA-LUM in 350 μL solution in a microcuvette with an optical pathlength of 10.0 mm. (b) The enlarged view to show the absorption spectra of highly diluted GNP-MUA-LUM solutions.

5.3.3 CL Detection of Unlysed and Lysed Red Blood Cells

As illustrated in Figure 5.3, the luminol-labeled GNPs can be used for CL detection under two different schemes. In this study, we focused on demonstrating the detection of blood samples using Scheme 1. Unlysed and lysed sheep blood samples were used to replace $Fe(CN)_6^{3-}$ ions as the analyte which also serves as the catalyst to generate luminol CL. The solutions containing ~$1x10^{10}$ luminol-labeled GNPs were preloaded in different PDMS wells and the solvent was then dried out. CL measurements were performed after adding the mixture of 4.0 μl of NaOH (0.1 M) and 4.0 μl of H_2O_2 (1.41 M) as well as 4.0 μl of blood sample of desired concentrations. The concentration of the sheep red blood cells in the stock blood solution was ~$4.6x10^9$ cells/ml, as

estimated by cell counting. The size of the sheep red blood cell is about 3-4 µm. In some experiments, the sheep red blood cells were lysed following the procedure described in the experimental section. The representative kinetic CL data obtained with the stock solutions of unlysed and lysed blood samples, respectively, and with those after 10^8 times dilution are shown in Figure 5.10. The CL signal of the lysed blood samples experienced a rapid decay with a half life of ~30 seconds (Figure 5.10a and Figure 5.10b), similar to what was observed with $Fe(CN)_6^{3-}$ ions (as shown in Figure 5.7c and Figure 5.7d). It is remarkable that such a strong CL signal can be observed with the lysed blood samples even after dilution by 108 times, which corresponds to ~0.18 cell/well.

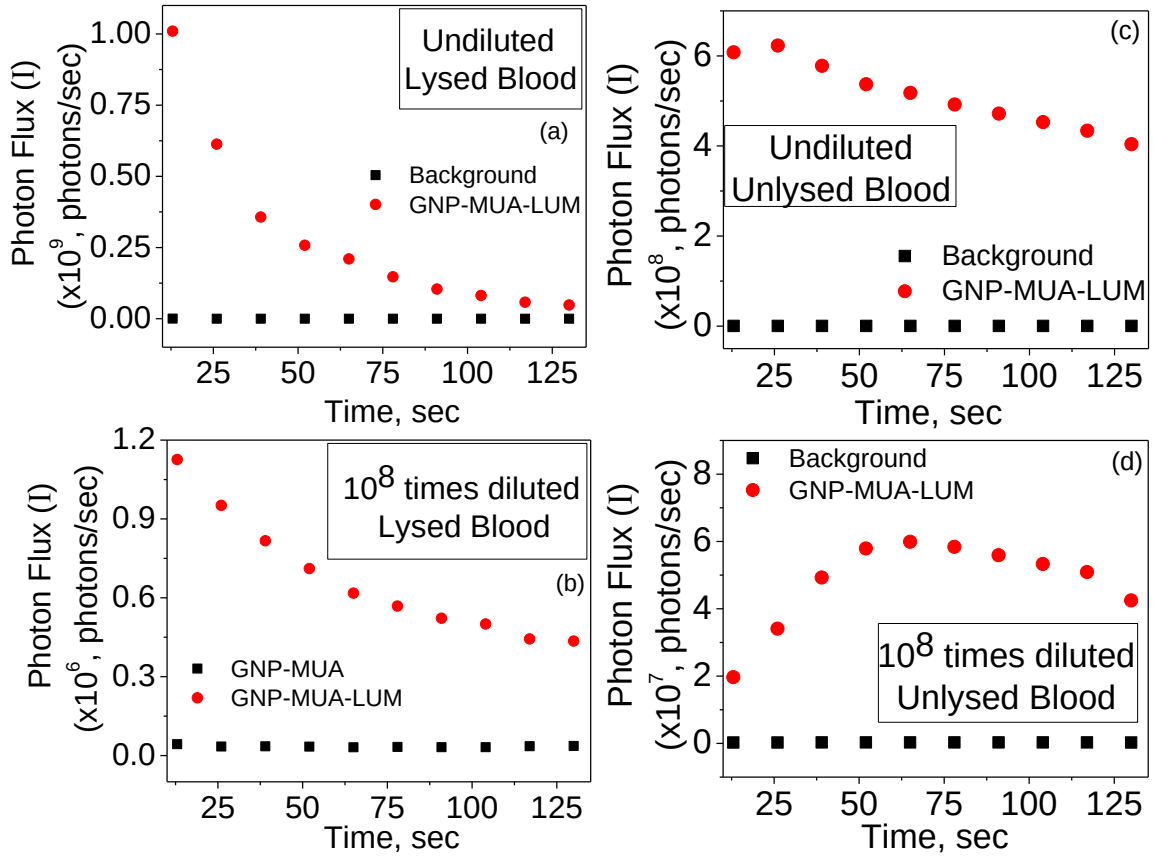

Figure 5.10 The kinetic plots of the CL signal (filled circles) of lysed (panels a and b) and unlysed (panels c and d) blood samples. Panels a and c were measured at stock concentration and panels b and d were measured after 10^8 fold dilution. The black squares represent the background from control experiments without adding any blood sample.

Interestingly, the unlysed blood samples showed quite different kinetics in CL measurements in both original and diluted samples. As shown in Figure 5.10c and Figure 5.10d, the CL signal rises in the initial period (~26 and 65 s, respectively) and then slowly decays. The rising and decay rates were lower in the highly diluted sample as compared to the original one. This is likely because the red blood cells need to be lysed first to release the hemoglobin to the exterior environment. The degradation of the polypeptidic portion of the hemoglobin then takes place, removing the protection to the reduced form of iron (i.e. Fe^{2+}) at the center of the histidine coordination.[171] As a result, Fe^{2+} is quickly oxidized into Fe^{3+} and becomes an active catalyst to facilitate the reaction of luminol molecules to generate CL. In the stock solution of the unlysed blood sample, there are likely many residual hemes outside the cell, hence the initial rise in CL signal is not prominent. But for the sample diluted by 10^8 times (to ~46 cells/ml), likely only a single red blood cell is randomly picked and dispensed into the PDMS well, which was lysed by the high concentration of NaOH (~0.033 M after mixing) to release hemoglobin for subsequent CL reaction. Hence the generation of CL is delayed by ~65 seconds.

Figure 5.11a and Figure 5.11b show the Log-Log plots of the background subtracted maximum CL signal (ΔI_{max}) vs. the dilution factor for lysed and unlysed blood samples, respectively. A linear relationship between $\log(\Delta I_{max})$ and log(dilution) was obtained for the lysed sample in a large range of the dilution factor ranging from 0 to 10^8. A slope of -0.459 is obtained from Figure 5.11a, which is very close to that of $\log(\Delta I_{max})$ vs. $\log(N_{GNP})$ (with N_{GNP} as the number of luminol-labeled GNPs) in Figure 5.8. This confirms that the CL in these experiments is likely based on the same mechanism (i.e. Scheme 1 in Figure 5.3). The unlysed blood sample in Figure 5.11b, however, shows a transition at the dilution factor of ~$5x10^4$. Two straight lines are needed to fit the experimental data, with a slope of -0.308 below 10^4 times dilution and a very small slope of -0.031 above 10^5 times of dilution. At the transition point of a dilution factor of ~$5x10^4$, there are ~370 cells dispensed in the PDMS well by calculation. This number is close to the limit of statistically reliable sampling. Other catalysts beside the hemoglobin from the intact red blood cells may also contribute to the CL signal and generates the CL even after 10^8 times dilution even though the slope is much smaller.

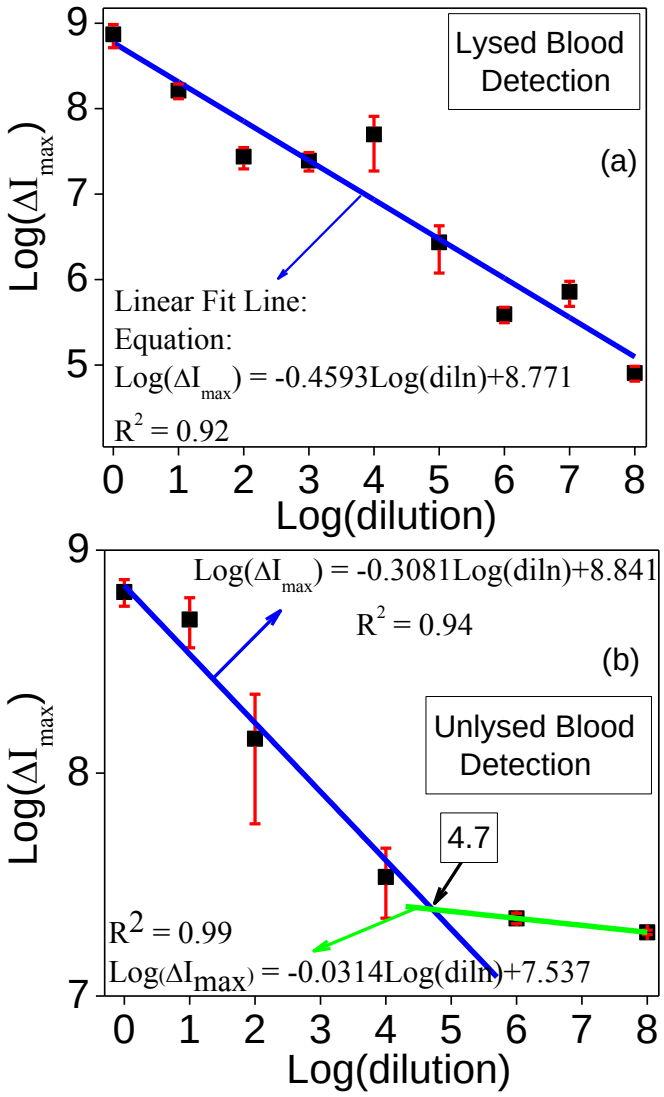

Figure 5.11 Calibration curves of the lysed and unlysed blood samples on the Log-Log scale of ΔI_{max} (the background subtracted peak CL intensity in kinetic measurements) vs. the dilution factor. The solid lines are linear fitting to two regions.

In this study, the CL reaction was carried out in a light tight chamber with a highly sensitive CCD which has relatively high cost. However, the method can be implemented with a photomultiplier tube detector coupled with fiber optics as a simple low-cost system with comparable photon collection efficiency. It is possible to develop a portable CL system for rapid and ultrasensitive point-of-care applications, which remains challenging with other techniques

such as fluorescence methods.[31] This CL method can be also applied on affinity based biosensors by incorporating additional biorecognition probes (such as antibodies or nucleic acid sequences) in luminol-labeled GNPs and using Scheme 2 in Figure 5.3 for analytical detection.

5.4 Conclusions

In conclusion, we have demonstrated that very strong CL signal can be generated with luminol molecules covalently attached to GNPs through an alkane thiol linker. This approach may be adopted for ultrasensitive analysis under two different schemes as shown in this work. The CL signal measured in 1.0 mM $Fe(CN)_6^{3-}$ solution scales linearly with the number of luminol-labeled GNPs in the log-log scale in a wide range from $1.0x10^{10}$ to $1.0x10^{3}$ GNPs in small PDMS wells. The ability to detect as small as 1,000 GNPs with luminol attachment is attributed to a high CL quantum efficiency of luminol molecules comparable to those in bulk solutions. The assessed detection sensitivity by CL from luminol-labeled GNPs is four orders of magnitude higher than that by optical absorption. By preloading sufficient amount of luminol-labeled GNPs in an array of PDMS microwells, we have demonstrated that strong CL can be generated from trace amount of blood samples in which either intact or lysed red blood cells are present. Particularly, the lysed blood sample can be detected following 10^{8} fold dilution. This method can be readily integrated with fiber optics and a low-cost detector into a portable point-of-care system for a rapid and ultrasensitive detection of trace blood contamination in hospitals, forensic sites, or other venues. The luminol-labeled GNPs can be further coupled with specific affinity probes such as antibodies or nucleic acid sequences to develop ultrasensitive biosensors for disease detection.

Chapter 6 - Conclusions and Future Direction

In this dissertation, nanoelectrodes and nanoparticles have been tried for developing different biosensing strategies. Most of our work is driven by the fact that there is a growing demand for label-free, fast, and sensitive techniques, which can at some point be utilized to construct hand-held devices for point-of-care detection. All of these project works provide an understanding of materials, methods and mechanisms of utilizing nanoscale material for different applications and hope that other researchers will benefit from results we have obtained to develop better materials and devices in future.

6.1 Understanding the electron transfer rates (ETRs) at NEAs and GCEs by AC and DC voltammetry

In this study, we used ferrocene functionalized NEAs and GCE (standard for comparison) to study the electron transfer kinetics. Initially, we employed DC voltammetry in both the cases and found that the ETR in case of NEA is very slow when compared to GCE (~17 times). This can seriously limit the use of NEA for biosensing using DC based electrochemical methods. To our surprise, when we used AC voltammetry instead of DC voltammetry we observed 100 times higher electron transfer rate at the NEAs. Lot of effort was made to quantitatively account for this behavior. Finally, we used electrochemical impedance spectroscopy and a proper physical model was used to account for all the anomalous behavior of NEAs when AC electrochemical technique is used. The electrochemical properties of the nanoelectrode were found to critically depend on the unique conical graphitic stacking of the carbon nanofibers, which facilitates a new capacitive pathway in high-frequency AC measurements.

In future, we can take advantage of high frequency signal enhancement given by NEA to develop biosensors, especially for cancerous protease detection. EIS experiments with GCE and NEA functionalized with tetrapeptide needs to be done, by biasing the WE at the formal potential of Fc. This experiment will give us the long range ETR, which can be compared to the values with just Fc attached WE. Optimization of ACV experimental conditions for each sequence of peptides needs to done carefully in the assay buffer. We can easily program the potentiostat to monitor real-time ACV. This will give us information about the kinetic behavior of the enzyme

understudy. The kinetic parameters thus obtained from electrochemistry can be compared from literature values or the values found from other standard assay techniques.

6.2 Dielectrophoretic trapping of bacterial cells at micropatterned NEAs

Rapid detection of pathogens is very crucial in several applications like monitoring water and food quality. We demonstrate the use of AC dielectrophoresis (DEP) and electrochemical impedance techniques with vertically aligned carbon nanofiber (VACNF) nanoelectrode arrays (NEAs) and ITO-coated glass in "points-and-lid" configuration. A nano-DEP device can be fabricated using UV-photolithography. A high frequency ac field was applied between NEA and ITO to generate p-DEP at the tips of exposed CNFs. Enhanced electric field gradient generated at the exposed CNF tips due to reduction in electrode size down to nanometer scale and high aspect ratio (~100) helps to overcome large hydrodynamic drag force experienced by *E. coli* flowing at higher flow velocities was noticed. A significant number of *E. coli* were captured at a high flow velocity of 1.6 mm/sec. A noticeable change in absolute impedance (|Z|) value at the NEA was observed in the Bode plot of impedance experiments. The results obtained in this study suggest the possibility of integration of a fully functional electronic device for rapid, reversible and label-free detection of pathogenic bacteria.

In future, to add more towards detection of pathogen we can integrate the DEP capture process with measuring Raman finger print of the captured pathogen. To enhance the Raman signal it might be necessary to incorporate nanoparticles along with pathogen so that both pathogen and nanoparticles are captured simultaneously, or another way would be to decorate exposed CNF with nanoparticles before DEP. For both the cases theoretical predictions of CM factor needs to be done. The methodologies presented in this chapter can also be directly extended for its use to capture smaller bioparticles like viruses.

6.3 Luminol decorated gold nanoparticles (GNPs) as a sensitive chemiluminescence (CL) biosensor for trace blood detection

CL is a very powerful analytical technique which can provide sensitivity orders of magnitude higher than that of commonly used fluoresecence methods. In conventional CL, the molecules (such as luminol) are dissolved in solutions. In our case luminol was covalently attached to GNPs of ~10 nm diameter. The nanoparticle serves as a carrier with large surface

area to ensure the functionalization of a large quantity of CL molecules. It provides the capability to be either suspended in solution or immobilized on a surface. This enables the application of nanoparticle-functionalized CL for detection of analytes in solution (such as red blood cells) in a multiwell format or as an amplified readout technique in a test strip format based on specific affinity binding. We have demonstrated a detailed procedure to prepare luminol-functionalized GNPs with convincing characterization with UV-Vis and IR spectroscopy and TEM. Two implementation schemes using luminol-GNPs were illustrated. In one scheme luminol-functionalized GNPs were exposed to blood samples of different concentrations and we were able to detect lysed blood samples after dilution by 10^8 times down on single red blood cell. In the other scheme, the CL signal was measured using 1.0 mM $Fe(CN)_6^{3-}$ solution. The CL signal scaled linearly with the number of luminol-labeled GNPs in the log-log scale in a wide range from $1.0x10^{10}$ to $1.0x10^3$ GNPs in small PDMS wells. The ability to detect as small as 1,000 GNPs with luminol attachment is attributed to a high CL quantum efficiency of luminol molecules comparable to those in bulk solutions. The assessed detection sensitivity by CL from luminol-labeled GNPs is four orders of magnitude higher than that by optical absorption.

In future, ultrasensitive readout methods can be developed for the detection of analytes or biomarkers in well-array format or affinity-based test strips. For examples we can detect microbes, proteins, and nucleic acid fragments (DNA, RNA, synthetic nucleic acids, etc.). The chemiluminescent assay can also adapted for the specific detection of virus particles (e.g. Hepatitis C) which is orders of magnitude more sensitive that the state-of-the-art colorimetric method based on light absorption by gold nanoparticles. It can potentially detect Hepatitis infections at very early stage without using PCR-based laboratory techniques. It can also be adapted for diagnosis of various diseases (such as cancers) through the ultrasensitive detection of specific biomarkers (such as proteins, peptide, ligands, and particular sequences of nucleic acid fragments).

Literature Cited

1. http://goldbook.iupac.org.

2. Kim, J. M.; Chang, S. M.; Muramatsu, H.; Isao, K. *Korean J. Chem. Eng.* **2011**, *28*, 987-1008.

3. Thévenot, D. R.; Toth, K.; Durst, R. A.; Wilson, G. S. *Biosens. Bioelectron.* **2001**, *16*, 121-131.

4. Patel, P. D. *TrAC, Trends Anal. Chem.* **2002**, *21*, 96-115.

5. Rogers, K. R.; Lin, J. N. *Biosens. Bioelectron.* **1992**, *7*, 317-321.

6. Rogers, K. R. *Biosens. Bioelectron.* **1995**, *10*, 533-541.

7. Collings, A. F.; Caruso, F. *Rep. Prog. Phys.* **1997**, *60*, 1397-1445.

8. Mehrvar, M.; Bis, C.; Scharer, J. M.; Moo-Young, M.; Luong, J. H. *Anal. Sci.* **2000**, *16*, 677-692.

9. Baird, C. L.; Myszka, D. G. *J. Mol. Recognit.* **2001**, *14*, 261-268.

10. Selvan, S. T.; Tan, T. T. Y.; Yi, D. K.; Jana, N. R. *Langmuir* **2010**, *26*, 11631-11641.

11. Jenkins, M., *Biomedical Polymers*. Woodhead Publishing: Cambridge, UK, 2007.

12. Kim, S. N.; Rusling, J. F.; Papadimitrakopoulos, F. *Adv. Mater.* **2007**, *19*, 3214-3228.

13. http://www.cancer.org/acs/groups/content/@nho/documents/document/caff2006pwsecuredpdf.pdf.

14. *Diabetes Care* **2003**, *26*, 917-932.

15. Nataro, J. P.; Kaper, J. B. *Clin. Microbiol. Rev.* **1998**, *11*, 403-403.

16. Mead, P. S.; Slutsker, L.; Dietz, V.; McCaig, L. F.; Bresee, J. S.; Shapiro, C.; Griffin, P. M.; Tauxe, R. V. *Emerging Infect. Dis.* **1999**, *5*, 607-625.

17. Abubakar, I.; Irvine, L.; Aldus, C. M.; Wyatt, G. M.; Fordham, R.; Schelenz, S.; Shepstone, L.; Howe, A.; Peck, M.; Hunter, P. R. *Health Technol. Assess.* **2007**, *11 (36)*.

18. *http://accessscience.com/content/Pathogen-detection,-food-borne/YB031850*.

19. Fung, D. Y. C. *Comprehensive Reviews in Food Science and Food Safety* **2002**, *1*, 3-22.

20. Melechko, A. V.; Merkulov, V. I.; McKnight, T. E.; Guillorn, M. A.; Klein, K. L.; Lowndes, D. H.; Simpson, M. L. *J. Appl. Phys.* **2005**, *97*, 41301-1-39.

21. Leonard, P.; Hearty, S.; Brennan, J.; Dunne, L.; Quinn, J.; Chakraborty, T.; O'Kennedy, R. *Enzyme Microb. Technol.* **2003**, *32*, 3-13.

22. Taguchi, T.; Takeyama, H.; Matsunaga, T. *Biosens. Bioelectron.* **2005**, *20*, 2276-2282.

23. Mansfield, L. P.; Forsythe, S. J. *Food Microbiol.* **2001**, *18*, 361-366.

24. Rompré, A.; Servais, P.; Baudart, J.; de-Roubin, M.-R.; Laurent, P. *J. Microbiol. Methods* **2002**, *49*, 31-54.

25. Schena, M.; Shalon, D.; Davis, R. W.; Brown, P. O. *Science* **1995**, *270*, 467-470.

26. Lipshutz, R. J.; Morris, D.; Chee, M.; Hubbell, E.; Kozal, M. J.; Shah, N.; Shen, N.; Yang, R.; Fodor, S. P. A. *BioTechniques* **1995**, *19*, 442-447.

27. Southern, E.; Mir, K.; Shchepinov, M. *Nat. Genet.* **1999**, *21*, 5-9.

28. Singh, A.; Goering, R. V.; Simjee, S.; Foley, S. L.; Zervos, M. J. *Clin. Microbiol. Rev.* **2006**, *19*, 512-530.

29. Powledge, T. M. *Advances in Physiology Education* **2004**, *28*, 44-50.

30. Kim, H.-S.; Pyun, J.-C. *Procedia Chemistry* **2009**, *1*, 1043-1046.

31. Knox Van Dyke, C. V. D., Karen Woodfork, *Luminescence Biotechnology: Instrumentation and Applications*. CRC Press, Newyork: 2001.

32. White, E. H.; Zafiriou, O.; Kagi, H. H.; Hill, J. H. M. *J. Am. Chem. Soc.* **1964**, *86*, 940-941.

33. White, E. H.; Bursey, M. M. *J. Am. Chem. Soc.* **1964**, *86*, 941-942.

34. White, E. H.; Roswell, D. F. *Acc. Chem. Res.* **1970**, *3*, 54-62.

35. Wang, J. *Analyst* **2005**, *130*, 421-426.

36. Vo-Dinh, T.; Cullum, B. M.; Stokes, D. L. *Sensors Actuators B: Chem.* **2001**, *74*, 2-11.

37. Arben, M., *Biosensing Using Nanomaterials*. John Wiley & Sons: New Jersey, 2009.

38. Nugent, J. M.; Santhanam, K. S. V.; Rubio, A.; Ajayan, P. M. *Nano Lett.* **2001**, *1*, 87-91.

39. Wang, J.; Musameh, M.; Lin, Y. *J. Am. Chem. Soc.* **2003**, *125*, 2408-2409.

40. Luo, H.; Shi, Z.; Li, N.; Gu, Z.; Zhuang, Q. *Anal. Chem.* **2001**, *73*, 915-920.

41. Cui, D. *J. Nanosci. Nanotechnol.* **2007**, *7*, 1298-1314.

42. Willner, I. *Science* **2002**, *298*, 2407-2408.

43. Patolsky, F.; Weizmann, Y.; Willner, I. *Angew. Chem. Int. Ed.* **2004**, *43*, 2113-2117.

44. Britto, P. J.; Santhanam, K. S. V.; Ajayan, P. M. *Bioelectrochem. Bioenerg.* **1996**, *41*, 121-125.

45. Davis, J. J.; Coles, R. J.; Allen, H.; Hill, O. *J. Electroanal. Chem.* **1997**, *440*, 279-282.

46. Che, G. L.; Lakshmi, B. B.; Fisher, E. R.; Martin, C. R. *Nature* **1998**, *393*, 346-349.

47. Rajesh; Ahuja, T.; Kumar, D. *Sensors Actuators B: Chem.* **2009**, *136*, 275-286.

48. Lin, Y.; Lu, F.; Tu, Y.; Ren, Z. *Nano Lett.* **2003**, *4*, 191-195.

49. Yu, Y.; Cimeno, A.; Lan, Y. C.; Rybczynski, J.; Wang, D. Z.; Paudel, T.; Ren, Z. F.; Wagner, D. J.; Qiu, M. Q.; Chiles, T. C.; Cai, D. *Micro & Nano Letters* **2009**, *4*, 27-33.

50. Heller, I.; Mannik, J.; Lemay, S. G.; Dekker, C. *Nano Lett.* **2009**, *9*, 377-382.

51. Koehne, J.; Chen, H.; Li, J.; Cassell, A. M.; Ye, Q.; Ng, H. T.; Han, J.; Meyyappan, M. *Nanotechnology* **2003**, *14*, 1239-1245.

52. Koehne, J. E.; Chen, H.; Cassell, A. M.; Yi, Q.; Han, J.; Meyyappan, M.; Li, J. *Clinic. Chem.* **2004**, *50*, 1886-1893.

53. Lee, H. J.; Beriet, C.; Ferrigno, R.; Girault, H. H. *J. Electroanal. Chem.* **2001**, *502*, 138-145.

54. Cai, D.; Ren, L.; Zhao, H.; Xu, C.; Zhang, L.; Yu, Y.; Wang, H.; Lan, Y.; Roberts, M. F.; Chuang, J. H.; Naughton, M. J.; Ren, Z.; Chiles, T. C. *Nat Nano* **2010**, *5*, 597-601.

55. Lin, Y.; Lu, F.; Tu, Y.; Ren, Z. *Nano Lett.* **2004**, *4*, 191-195.

56. Wang, J.; Lin, Y. *TrAC, Trends Anal. Chem.* **2008**, *27*, 619-626.

57. Li, J.; Ng, H. T.; Cassell, A.; Fan, W.; Chen, H.; Ye, Q.; Koehne, J.; Han, J.; Meyyappan, M. *Nano Lett.* **2003**, *3*, 597-602.

58. Koehne, J.; Li, J.; Cassell, A. M.; Chen, H.; Ye, Q.; Ng, H. T.; Han, J.; Meyyappan, M. *J. Mater. Chem.* **2004**, *14*, 676-684.

59. Li, Y.; Kaneko, T.; Hirotsu, Y.; Hatakeyama, R. *Small* **2010**, *6*, 27-30.

60. Arrigan, D. W. M. *Analyst* **2004**, *129*, 1157-1165.

61. Kuhr, W. *Nat. Biotechnol.* **2000**, *18*, 1042.

62. Gooding, J. J. *Electroanalysis* **2002**, *14*, 1149-1156.

63. Sosnowski, R.; Tu, E.; Butler, W.; O'Connell, J.; Heller, M. *Proc. Natl. Acad. Sci. U.S.A.* **1997**, *94*.

64. Umek, R. M.; Lin, S. W.; Vielmetter, J.; Terbrueggen, R. H.; Irvine, B.; Yu, C. J.; Kayyem, J. F.; Yowanto, H.; Blackburn, G. F.; Farkas, D. H.; Chen, Y. P. *J. Mol. Diagnostics* **2001**, *3*, 74-84.

65. Popovich, N.; Thorp, H. *Interface* **2002**, *11*.

66. Ghindilis, A. L.; Smith, M. W.; Schwarzkopf, K. R.; Roth, K. M.; Peyvan, K.; Munro, S. B.; Lodes, M. J.; Stover, A. G.; Bernards, K.; Dill, K.; McShea, A. *Biosens. Bioelectron.* **2007**, *22*, 1853-1860.

67. Dill, K.; Ghindilis, A.; Schwarzkopf, K. *Lab Chip* **2006**, *6*, 1052-1055.

68. Varshney, M.; Li, Y. B. *Biosens. Bioelectron.* **2007**, *22*, 2408-2414.

69. Varshney, M.; Li, Y. B.; Srinivasan, B.; Tung, S. *Sensors and Actuators B-Chemical* **2007**, *128*, 99-107.

70. Yang, L.; Bashir, R. *Biotechnol. Adv.* **2008**, *26*, 135-150.

71. Voldman, J. *Annu. Rev. Biomed. Eng.* **2006**, *8*, 425-454.

72. Jianrong, C.; Yuqing, M.; Nongyue, H.; Xiaohua, W.; Sijiao, L. *Biotechnol. Adv.* **2004**, *22*, 505-518.

73. Wang, J. *Small* **2005**, *1*, 1036-1043.

74. Essner, J. Dye Sensitized Solar Cells: Optimization of Gratzel Solar Cells Towards Plasmonic Enhanced Photovoltaics. Kansas State University, 2011.

75. Zhang, X.; Guo, Q.; Cui, D. *Sensors* **2009**, *9*, 1033-1053.

76. http://www.tedpella.com/gold_html/goldsols.htm.

77. Mirkin, C. A.; Letsinger, R. L.; Mucic, R. C.; Storhoff, J. J. *Nature* **1996**, *382*, 607-609.

78. Xia, F.; Zuo, X.; Yang, R.; Xiao, Y.; Kang, D.; Vallee-Belisle, A.; Gong, X.; Yuen, J. D.; Hsu, B. B. Y.; Heeger, A. J.; Plaxco, K. W. *Proc Natl Acad Sci* **2010**, *107*, 10837-10841.

79. Jena, B. K.; Raj, C. R. *Biosens. Bioelectron.* **2008**, *23*, 1285-1290.

80. Mao, X.; Ma, Y.; Zhang, A.; Zhang, L.; Zeng, L.; Liu, G. *Anal. Chem.* **2009**, *81*, 1660-1668.

81. Syed, L. U.; Liu, J.; Prior, A. M.; Hua, D. H.; Li, J. *Electroanalysis* **2011**, *23*, 1709-1717.

82. Syed, L. U.; Liu, J.; Price, A. K.; Li, Y.-f.; Culbertson, C. T.; Li, J. *Electrophoresis* **2011**, *32*, 2358-2365.

83. Cruden, B. A.; Cassell, A. M.; Ye, Q.; Meyyappan, M. *J. Appl. Phys.* **2003**, *94*, 4070.

84. Ren, Z. F.; Huang, Z. P.; Xu, J. W.; Wang, J. H.; Bush, P.; Siegal, M. P.; Provencio, P. N. *Science* **1998**, *282*, 1105-1107.

85. Ngo, Q.; Cassell, A. M.; Austin, A. J.; Li, J.; Krishnan, S.; Meyyappan, M.; Yang, C. Y. *IEEE Electron Device Lett.* **2006**, *27*, 221.

86. Bard, A. J.; Faulkner, L. R., *Electrochemical Methods: Fundamental and Applications*. 2nd ed.; Wiley: New York, 2001.

87. Menon, V. P.; Martin, C. R. *Anal. Chem.* **1995**, *67*, 1920-1928.

88. Wang, J., *Analytical Electrochemistry*. 3rd ed.; Wiley-VCH: 2006.

89. Ordeig, O. *Electroanalysis* **2007**, *19*, 1973-1986.

90. Li, J.; Koehne, J. E.; Cassell, A. M.; Chen, H.; Ng, H. T.; Ye, Q.; Fan, W.; Han, J.; Meyyappan, M. *Electroanalysis* **2005**, *17*, 15-27.

91. Baramee, A.; Coppin, A.; Mortuaire, M.; Pelinski, L.; Tomavo, S.; Brocard, J. *Biorg. Med. Chem.* **2006**, *14*, 1294-1302.

92. Tsierkezos, N.; Ritter, U. *J. Appl. Electrochem.* **2010**, *40*, 409-417.

93. Creager, S.; Yu, C. J.; Bamdad, C.; O'Connor, S.; MacLean, T.; Lam, E.; Chong, Y.; Olsen, G. T.; Luo, J. Y.; Gozin, M.; Kayyem, J. F. *J. Am. Chem. Soc.* **1999**, *121*, 1059-1064.

94. Creager, S. E.; Wooster, T. T. *Anal. Chem.* **1998**, *70*, 4257-4263.

95. Zhang, L.; Austin, D.; Merkulov, V. I.; Meleshko, A. V.; Klein, K. L.; Guillorn, M. A.; Lowndes, D. H.; Simpson, M. L. *Appl. Phys. Lett.* **2004**, *84*, 3972-3974.

96. Banks, C. E.; Davies, T. J.; Wildgoose, G. G.; Compton, R. G. *Chem. Commun.* **2005**, 829-841.

97. Zoski, C. G. *Electroanalysis* **2002**, *14*, 1041-1051.

98. Penner, R. M.; Heben, M. J.; L., L. T.; Lewis, N. S. *Science* **1990**, *250*, 1118-1121.

99. Fan, F.-R. F.; Bard, A. J. *Science* **1995**, *267*, 871-874.

100. Yu, Z.; McKnight, T. E.; Ericson, M. N.; Melechko, A. V.; Simpson, M. L.; Morrison, B. *Nano Lett.* **2007**, *7*, 2188-2195.

101. McKnight, T. E.; Melechko, A. V.; Hensley, D. K.; Mann, D. G. J.; Griffin, G. D.; Simpson, M. L. *Nano Lett.* **2004**, *4*, 1213-1219.

102. Chidsey, C. E. D. *Science* **1991**, *251*, 919-922.

103. Chidsey, C. E. D.; Bertozzi, C. R.; Putvinski, T. M.; Mujsce, A. M. *J. Am. Chem. Soc.* **1990**, *112*, 4301-4306.

104. Sikes, H. D.; Smalley, J. F.; Dudek, S. P.; Cook, A. R.; Newton, M. D.; Chidsey, C. E. D.; Feldberg, S. W. *Science* **2001**, *291*, 1519-1523.

105. Choi, S. H.; Kim, B.; Frisbie, C. D. *Science* **2008**, *320*, 1482-1486.

106. Xia, J. L.; Chen, F.; Li, J. H.; Tao, N. J. *Nat. Nanotechnol.* **2009**, *4*, 505-509.

107. Heller, I.; Kong, J.; Heering, H. A.; Williams, K. A.; Lemay, S. G.; Dekker, C. *Nano Lett.* **2004**, *5*, 137-142.

108. McCreery, R. L. *Chem. Rev.* **2008**, *108*, 2646-2687.

109. Feldberg, S. W. *Anal. Chem.* **2010**, *82*, 5176-5183.

110. Xun, S.; Song, X.; Wang, L.; Grass, M. E.; Liu, Z.; Battaglia, V. S.; Liu, G. *J. Electrochem. Soc.* **2011**, *158*, A1260-A1266.

111. Lu, M. P.; Hsiao, C. Y.; Lai, W. T.; Yang, Y. S. *Nanotechnology* **2010**, *21*.

112. Li, Q. The Study of DNA Dynamics at Carbon Electrode Surface Toward DNA Sensors by Fluorescence and Electrochemical Impedance Spectroscopy. Kansas State University, 2011.

113. Laviron, E. *J. Electroanal. Chem.* **1979**, *101*, 19-28.

114. Finklea, H. O., Electrochemistry of organized monolayers of thiols and related molecules on electrodes. In *Electroanalytical Chemistry: a Series of Advances, Vol 19*, Marcel Dekker: New York, 1996; Vol. 19, pp 109-335.

115. Landis, E. C.; Hamers, R. J. *J. Phys. Chem. C* **2008**, *112*, 16910-16918.

116. Weber, K.; Creager, S. E. *Anal. Chem.* **1994**, *66*, 3164-3172.

117. Randin, J. P.; Yeager, E. *J. Electrochem. Soc.* **1971**, *118*, 711.

118. Wang, D. W.; Li, F.; Wu, Z. S.; Ren, W. C.; Cheng, H. M. *Electrochem. Commun.* **2009**, *11*, 1729-1732.

119. Almond, D. P.; Bowen, C. R. *Phys. Rev. Lett.* **2004**, *92*, 4.

120. http://www.ncbi.nlm.nih.gov/pubmedhealth/PMH0002267/.

121. Bogyo, M. *Proc. eedings of the National Academy of Sciences of the United States of America 107*, 2379-2380.

122. Chen, J.-M.; Dando, P. M.; Rawlings, N. D.; Brown, M. A.; Young, N. E.; Stevens, R. A.; Hewitt, E.; Watts, C.; Barrett, A. J. *J. Biol. Chem.* **1997**, *272*, 8090-8098.

123. Wu, W. Y.; Luo, Y. P.; Sun, C. Z.; Liu, Y. A.; Kuo, P.; Varga, J.; Xiang, R.; Reisfeld, R.; Janda, K. D.; Edgington, T. S.; Liu, C. *Cancer Res.* **2006**, *66*, 970-980.

124. http://www.rndsystems.com/pdf/2199-CY.pdf.

125. Svoboda, K.; Block, S. M. *Annu. Rev. Biophys. Biomol. Struct.* **1994**, *23*, 247-285.

126. Wu, J. R. *J. Acoust. Soc. Am.* **1991**, *89*, 2140-2143.

127. Jung, D. R.; Kapur, R.; Adams, T.; Giuliano, K. A.; Mrksich, M.; Craighead, H. G.; Taylor, D. L. *Crit. Rev. Biotechnol.* **2001**, *21*, 111-154.

128. Lapizco-Encinas, B.; Simmons, B.; Cummings, E.; Fintschenko, Y. *Electrophoresis* **2004**, *25*, 1695-1704.

129. Klodzinska, E.; Buszewski, B. *Anal. Chem.* **2009**, *81*, 8-15.

130. Desai, M. J.; Armstrong, D. W. *Microbiol. Mol. Biol. Rev.* **2003**, *67*, 38-51.

131. Arumugam, P. U.; Chen, H.; Cassell, A. M.; Li, J. *J. Phys. Chem. A* **2007**, *111*, 12772-12777.

132. Pohl, H. A., *Dielectrophoresis: The behavior of neutral matter in nonuniform electric fields*. Cambridge Univ. Press: Great Britain, 1978.

133. Betts, W. B. *Trends Food Sci. Technol.* **1995**, *6*, 51-58.

134. Suehiro, J.; Hamada, R.; Noutomi, D.; Shutou, M.; Hara, M. *J. Electrostatics* **2003**, *57*, 157-168.

135. Castellarnau, M.; Errachid, A.; Madrid, C.; Juarez, A.; Samitier, J. *Biophys. J.* **2006**, *91*, 3937-3945.

136. Park, K.; Akin, D.; Bashir, R. *Biomed. Microdevices* **2007**, *9*, 877-883.

137. Suehiro, J.; Ohtsubo, A.; Hatano, T.; Hara, M. *Sensors and Actuators B-Chemical* **2006**, *119*, 319-326.

138. Liju, Y.; Banada, P. P.; Chatni, M. R.; Kwan Seop, L.; Bhunia, A. K.; Ladisch, M.; Bashir, R. *Lab on a Chip: 6 (7) 896-905* **2006**, *6*, 896-905.

139. Crews, N.; Darabi, J.; Voglewede, P.; Guo, F.; Bayoumi, A. *Sensors and Actuators B-Chemical* **2007**, *125*, 672-679.

140. Tu, Y.; Lin, Y. H.; Yantasee, W.; Ren, Z. F. *Electroanalysis* **2005**, *17*, 79-84.

141. Tu, Y.; Lin, Y. H.; Ren, Z. F. *Nano Lett.* **2003**, *3*, 107-109.

142. Baker, S. E.; Tse, K. Y.; Lee, C. S.; Hamers, R. J. *Diamond Relat. Mater.* **2006**, *15*, 433-439.

143. Arumugam, P. U.; Chen, H.; Siddiqui, S.; Weinrich, J. A. P.; Jejelowo, A.; Li, J.; Meyyappan, M. *Biosens. Bioelectron.* **2009**, *24*, 2818-2824.

144. Edgcombe, C. J.; Valdre, U. *Journal Of Microscopy-Oxford* **2001**, *203*, 188-194.

145. Guillorn, M. A.; Hale, M. D.; Merkulov, V. I.; Simpson, M. L.; Eres, G. Y.; Cui, H.; Puretzky, A. A.; Geohegan, D. B. *Appl. Phys. Lett.* **2002**, *81*, 2860-2862.

146. Teo, K. B. K.; Minoux, E.; Hudanski, L.; Peauger, F.; Schnell, J. P.; Gangloff, L.; Legagneux, P.; Dieumegard, D.; Amaratunga, G. A. J.; Milne, W. I. *Nature* **2005**, *437*, 968.

147. Tuukkanen, S.; Toppari, J. J.; Kuzyk, A.; Hirviniemi, L.; Hytonen, V. P.; Ihalainen, T.; Torma, P. *Nano Lett.* **2006**, *6*, 1339-1343.

148. Hughes, M. P. *Electrophoresis* **2002**, *23*, 2569-2582.

149. Voldman, J. PhD Thesis, MIT, 2001.

150. Burke, P. J., Nano-dielectrophoresis: Electronic Nanotweezers. In *Encyclopedia of Nanoscience and Nanotechnology*, 2004; Vol. 6, pp 623-641.

151. Jones, T. B., *Electromechanics of Particles*. Cambridge University Press: Cambridge, UK, 1995.

152. Pethig, R. *Biomicrofluidics* **2010**, *4*, 022811.

153. Clague, D. S.; Wheeler, E. K. *Physical Review E* **2001**, *64*, 026605.

154. Huang, Y.; Pethig, R. *Meas. Sci. Technol.* **1991**, *2*, 1142-1146.

155. Gray, D. S.; Tan, J. L.; Voldman, J.; Chen, C. S. *Biosens. Bioelectron.* **2004**, *19*, 1765-1774.

156. Ermolina, I.; Morgan, H.; Green, N. G.; Milner, J. J.; Feldman, Y. *Biochimica Et Biophysica Acta-General Subjects* **2003**, *1622*, 57-63.

157. Liu, Y. S.; Walter, T. M.; Chang, W. J.; Lim, K. S.; Yang, L. J.; Lee, S. W.; Aronson, A.; Bashir, R. *Lab Chip* **2007**, *7*, 603-610.

158. Markx G, M. T. a. R. P. *J Biotechnology* **1994**, *32*, 29.

159. Lapizco-Encinas, B. H.; Ozuna-Chacón, S.; Rito-Palomares, M. *J. Chromatogr. A* **2008**, *1206*, 45-51.

160. Kuzyk, A.; Yurke, B.; Toppari, J. J.; Linko, V.; Torma, P. *Small* **2008**, *4*, 447-450.

161. Huang, Y.; Joo, S.; Duhon, M.; Heller, M.; Wallace, B.; Xu, X. *Anal. Chem.* **2002**, *74*, 3362-3371.

162. Xu, G. C., M.; Yang, C.; Sukumar, P.; Choolani, M.; Ying, Y. J. *Journal of Physics: Conference Series* **2006**, *34*, 1106-1111.

163. Irimajiri, A.; Hanai, T.; Inouye, A. *J. Theor. Biol.* **1979**, *78*, 251-269.

164. Huang, Y.; Holzel, R.; Pethig, R.; Wang, X. B. *Phys. Med. Biol.* **1992**, *37*, 1499-1517.

165. Asami, K.; Hanai, T.; Koizumi, N. *Biophys. J.* **1980**, *31*, 215-228.

166. Sanchis, A.; Brown, A. P.; Sancho, M.; Martinez, G.; Sebastian, J. L.; Munoz, S.; Miranda, J. M. *Bioelectromagnetics* **2007**, *28*, 393-401.

167. Li, H.; Zheng, Y.; Akin, D.; Bashir, R. *Microelectromech. Syst.* **2005**, *14*, 103-112.

168. Suehiro, J.; Yatsunami, R.; Hamada, R.; Hara, M. *Journal of Physics D-Applied Physics* **1999**, *32*, 2814-2820.

169. Suehiro, J.; Noutomi, D.; Shutou, M.; Hara, M. *J. Electrostatics* **2003**, *58*, 229-246.

170. Su, Y.; Chen, H.; Wang, Z.; Lv, Y. *Appl. Spectrosc. Rev.* **2007**, *42*, 139-176.

171. Barni, F.; Lewis, S. W.; Berti, A.; Miskelly, G. M.; Lago, G. *Talanta* **2007**, *72*, 896-913.

172. Ronaghi, M.; Uhlén, M.; Nyrén, P. *Science* **1998**, *281*, 363-365.

173. Rechberger, W.; Hohenau, A.; Leitner, A.; Krenn, J. R.; Lamprecht, B.; Aussenegg, F. R. *Opt. Commun.* **2003**, *220*, 137-141.

174. Schmid, G.; Simon, U. *Chem. Commun.* **2005**, 697-710.

175. Jain, P. K.; Lee, K. S.; El-Sayed, I. H.; El-Sayed, M. A. *The Journal of Physical Chemistry B* **2006**, *110*, 7238-7248.

176. Abad, J. M.; Mertens, S. F. L.; Pita, M.; Fernández, V. M.; Schiffrin, D. J. *J. Am. Chem. Soc.* **2005**, *127*, 5689-5694.

177. Hostetler, M. J.; Green, S. J.; Stokes, J. J.; Murray, R. W. *J. Am. Chem. Soc.* **1996**, *118*, 4212-4213.

178. Hostetler, M. J.; Wingate, J. E.; Zhong, C.-J.; Harris, J. E.; Vachet, R. W.; Clark, M. R.; Londono, J. D.; Green, S. J.; Stokes, J. J.; Wignall, G. D.; Glish, G. L.; Porter, M. D.; Evans, N. D.; Murray, R. W. *Langmuir* **1998**, *14*, 17-30.

179. Bartz, M.; Kuther, J.; Nelles, G.; Weber, N.; Seshadri, R.; Tremel, W. *J. Mater. Chem.* **1999**, *9*, 1121-1125.

180. Alivisatos, A. P.; Johnsson, K. P.; Peng, X.; Wilson, T. E.; Loweth, C. J.; Bruchez, M. P.; Schultz, P. G. *Nature* **1996**, *382*, 609-611.

181. Lee, J.-S.; Ulmann, P. A.; Han, M. S.; Mirkin, C. A. *Nano Lett.* **2008**, *8*, 529-533.

182. Su, X.; Kanjanawarut, R. *ACS Nano* **2009**, *3*, 2751-2759.

183. Kim, J.-Y.; Lee, J.-S. *Nano Lett.* **2009**, *9*, 4564-4569.

184. Baptista, P.; Pereira, E.; Eaton, P.; Doria, G.; Miranda, A.; Gomes, I.; Quaresma, P.; Franco, R. *Anal. Bioanal. Chem.* **2008**, *391*, 943-950.

185. Yuan, J.; Shiller, A. M. *Anal. Chem.* **1999**, *71*, 1975-1980.

186. Prilutsky, D.; Shneider, E.; Shefer, A.; Rogachev, B.; Lobel, L.; Last, M.; Marks, R. S. *Anal. Chem.* **2011**, *83*, 4258-4265.

187. Tsukagoshi, K.; Nakahama, K.; Nakajima, R. *Anal. Chem.* **2004**, *76*, 4410-4415.

188. Liu, B.-F.; Ozaki, M.; Utsumi, Y.; Hattori, T.; Terabe, S. *Anal. Chem.* **2002**, *75*, 36-41.

189. Bergervoet, P. W. M.; van Riessen, N.; Sebens, F. W.; van der Zwet, W. C. *J. Hosp. Infect.* **2008**, *68*, 329-333.

190. Zhang, Z.-F.; Cui, H.; Lai, C.-Z.; Liu, L.-J. *Anal. Chem.* **2005**, *77*, 3324-3329.

191. Duan, C. F.; Cui, H.; Zhang, Z. F.; Liu, B.; Guo, J. Z.; Wang, W. *J. Phys. Chem. C* **2007**, *111*, 4561-4566.

192. Taton, T. A.; Mirkin, C. A.; Letsinger, R. L. *Science* **2000**, *289*, 1757-1760.

193. Zhao, L.; Sun, L.; Chu, X. *TrAC, Trends Anal. Chem.* **2009**, *28*, 404-415.

194. Li, D.; He, Q.; Cui, Y.; Duan, L.; Li, J. *Biochem. Biophys. Res. Commun.* **2007**, *355*, 488-493.

195. Silverstein, R. M.; Bassler, G. C.; Morrill, T. C., *Spectrometric Identification of Organic Compounds. 4th ed.* . John Wiley and Sons: New York, 1981.

196. Cui, H.; Wang, W.; Duan, C.-F.; Dong, Y.-P.; Guo, J.-Z. *Chemistry – A European Journal* **2007**, *13*, 6975-6984.

197. Yang, X.; Guo, Y.; Wang, A. *Anal. Chim. Acta* **2010**, *666*, 91-96.

198. Cai, S.; Xin, L.; Lau, C.; Lu, J. *Analyst* **2010**, *135*, 615-620.

Appendix A - ACV data analysis and EIS plots with different equivalent circuit fits

ACV experiment data analysis using Creager's approach

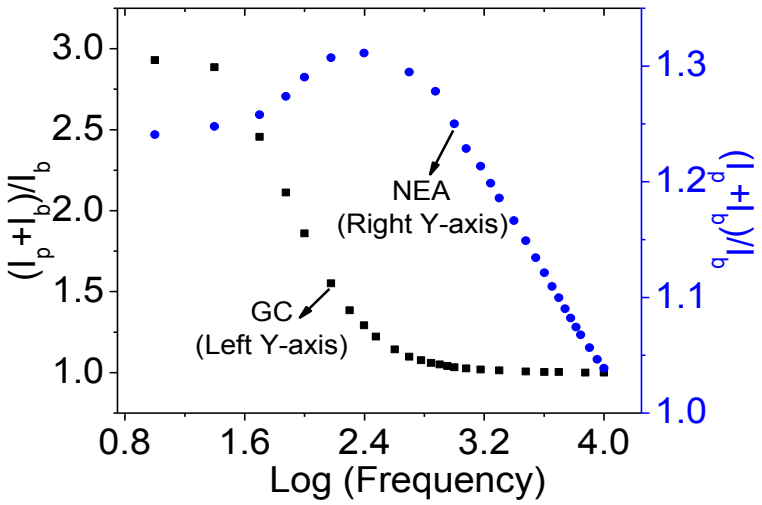

Figure A.1 Plots of $(I_p+I_b)/I_b$ vs. log(frequency) prepared using ACV data shown in Figure 3.7 for the Fc-CH_2-NH_2 modified GCE and CNF NEA, in the fashion reported by Creager et al.[94]

Bode plots of GCE and NEA

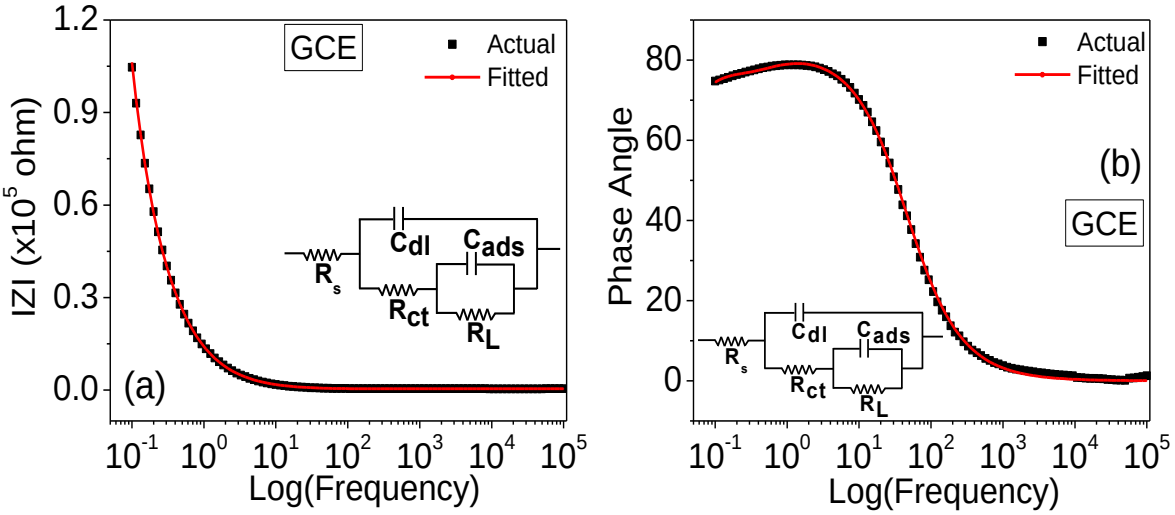

Figure A.2 Bode plots of a GCE functionalized with ferrocene with (a) total impedance vs. log(frequency) and (b) phase angle vs. log(frequency). These are the same EIS data shown in Nyquist plot in Figure 3.11a. The insets are the equivalent circuits used to fit the EIS data.

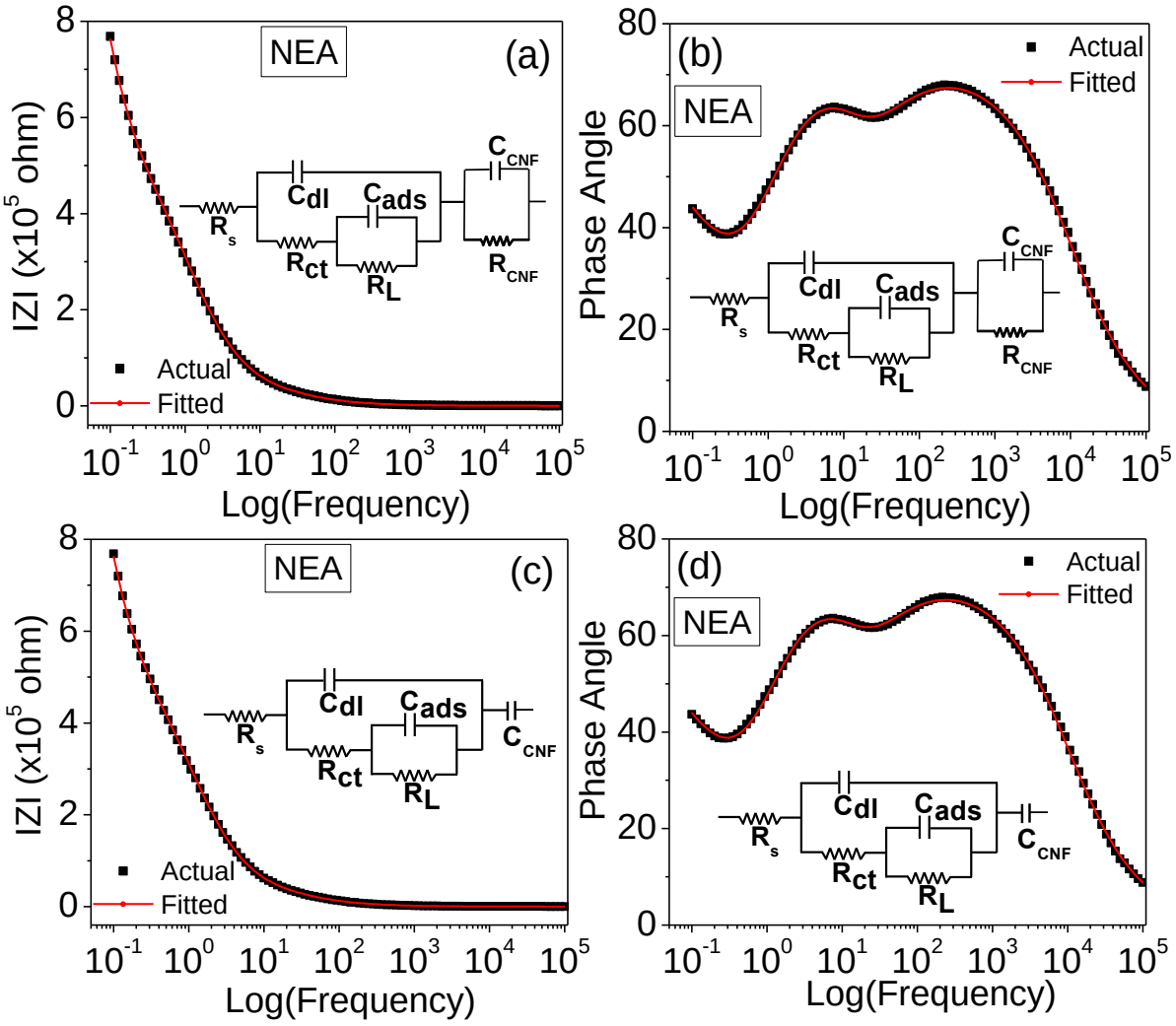

Figure A.3 Bode plots of a CNF NEA functionalized with ferrocene with (a) and (c) the total impedance vs. log(frequency); (b) and (d) phase angle vs. log(frequency). These are the same EIS data shown in Nyquist plot in Figure 3.11b. (a) and (b) use a parallel circuit (C_{CNF} and R_{CNF}) to represent intrinsic properties of the CNF while (c) and (d) only use a single capacitor C_{CNF}. As seen in the figure, the two equivalent circuits fit the experimental EIS data equally well.

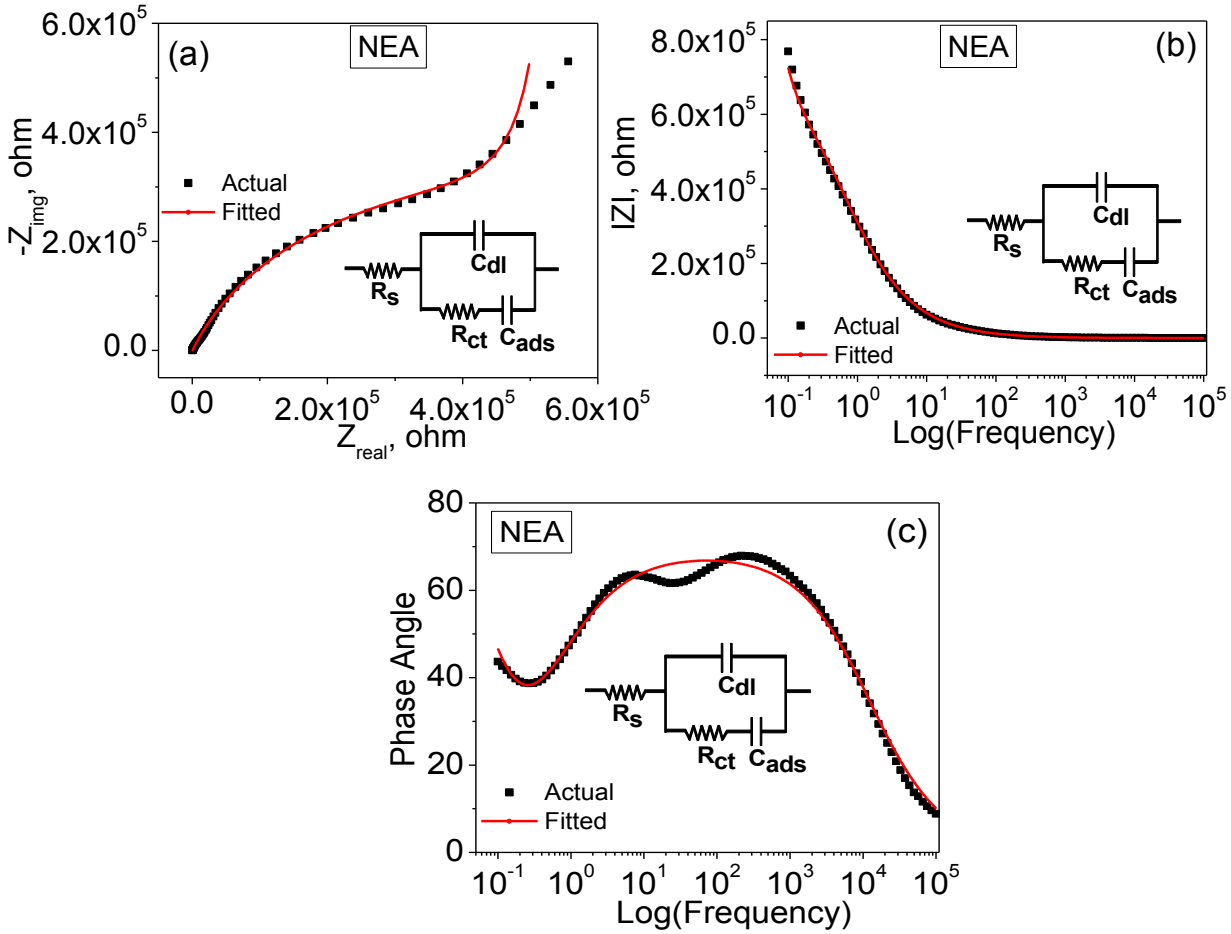

Figure A.4 Nyquist (a) and bode plots of (b) impedance vs. log(frequency) and (c) phase angle vs. log(frequency) of a CNF NEA functionalized with ferrocene, fitted with modified Randles circuit that was used by Creager et al.[94]

Modified Randles circuit which was used by Creager et al. [94] was initially tried to fit the EIS data of the ferrocene functionalized CNF NEA. The plots of which are shown in Figure A.4 and it can be clearly seen that this equivalent circuit cannot fit the data very well. The unsatisfied fitting quality is more obvious when we look at the bode plot (Figure A.4c) of phase angle vs. log(frequency). Particularly, the two peaks at ~5 Hz and ~650 Hz indicate that the circuit should consist of two RC circuits in series as shown in Figure A.3b. This provides strong justification to the equivalent circuit that is used (Figure 3.10b and Figure A.3) to fit the EIS data of the ferrocene-functionalized CNF NEA.

Table A.1 Comparison of the fitting parameters of the two equivalent circuits for the electrochemical impedance spectra of Fc-attached CNF NEA electrodes

Circuit for CNF	R_s, Ω	C_{dl}, F (n)	R_{ct}, Ω	C_{ads}, F (n)	R_L, Ω	C_{CNF}, F (n)	R_{CNF}, Ω	k^o_{ac} (s^{-1})
Parallel C_{CNF}, R_{CNF}	311.3	4.144×10^{-7} (0.864)	5.167×10^4	2.552×10^{-7} (0.976)	2.621×10^5	2.488×10^{-6} (0.707)	2.946×10^7	**38.0**
C_{CNF} only	312.5	4.451×10^{-7} (0.85)	5.997×10^4	2.187×10^{-7}	2.664×10^5	2.561×10^{-6} (0.715)	--	**38.1**

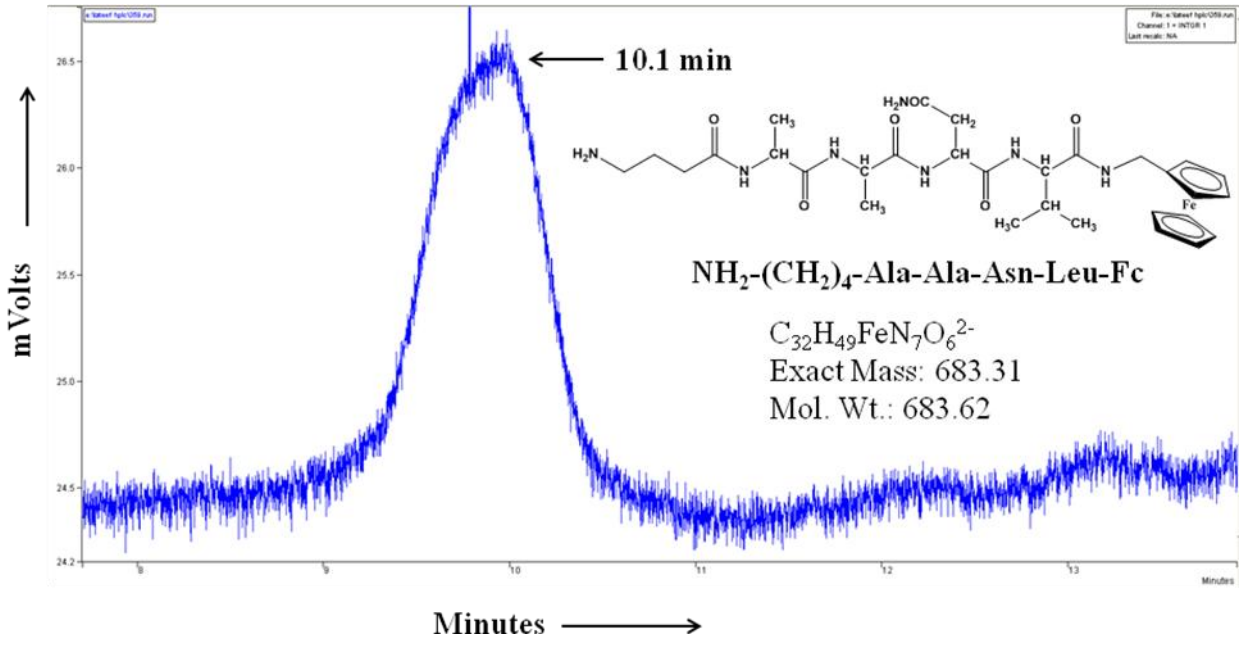

Figure A.5 Chromatogram of authentic ferrocenyl tetrapeptide sample. It elutes at a retention time of ~10.1 min.

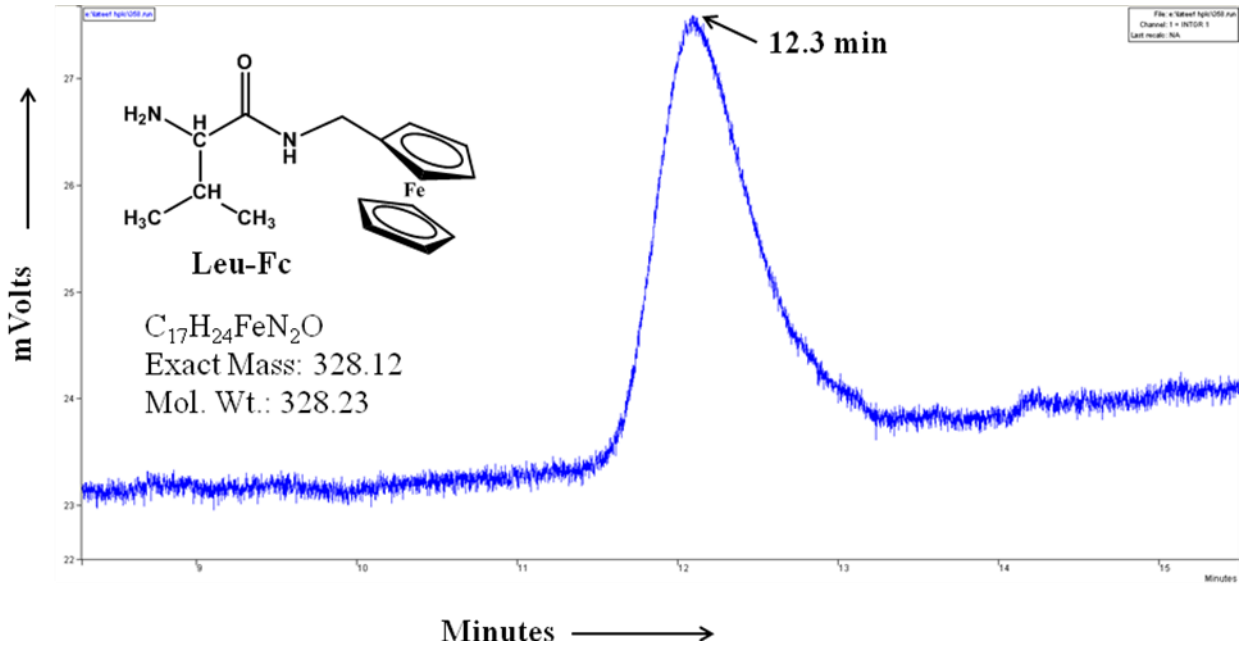

Figure A.6 Chromatogram of authentic fragment Leu-Fc sample. It elutes at a retention time of ~12.3 min.

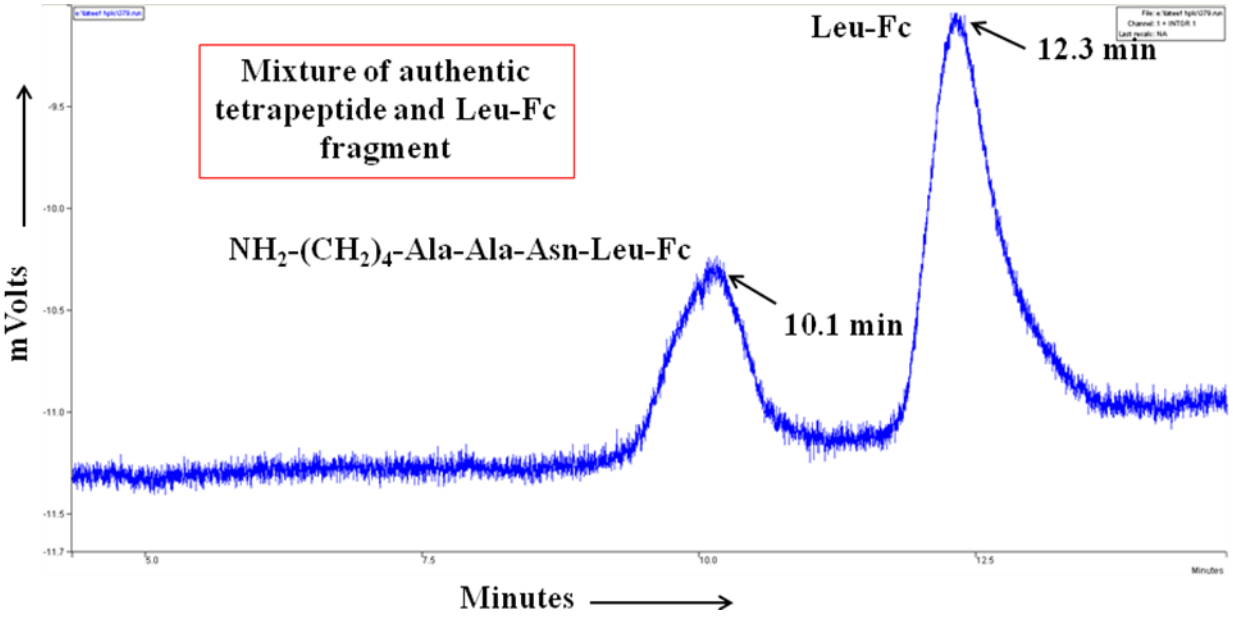

Figure A.7 Chromatogram of a mixture of authentic ferrocenyl tetrapeptide and fragment Leu-Fc sample. Tetrapeptide elutes at ~10.1 min and the fragment at 12.3 min.

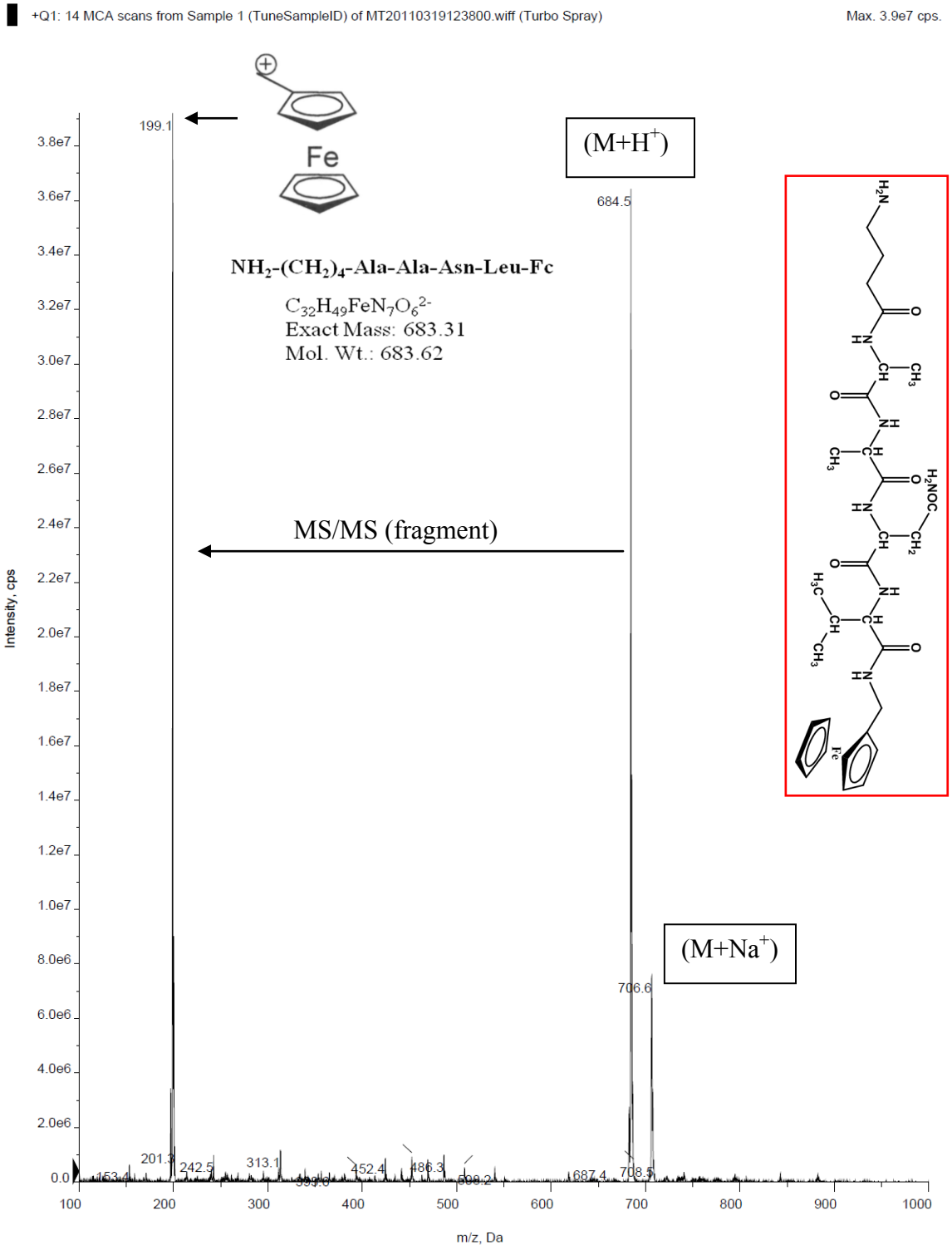

Figure A.8 Mass spectra of authentic ferrocenyl tetrapeptide.

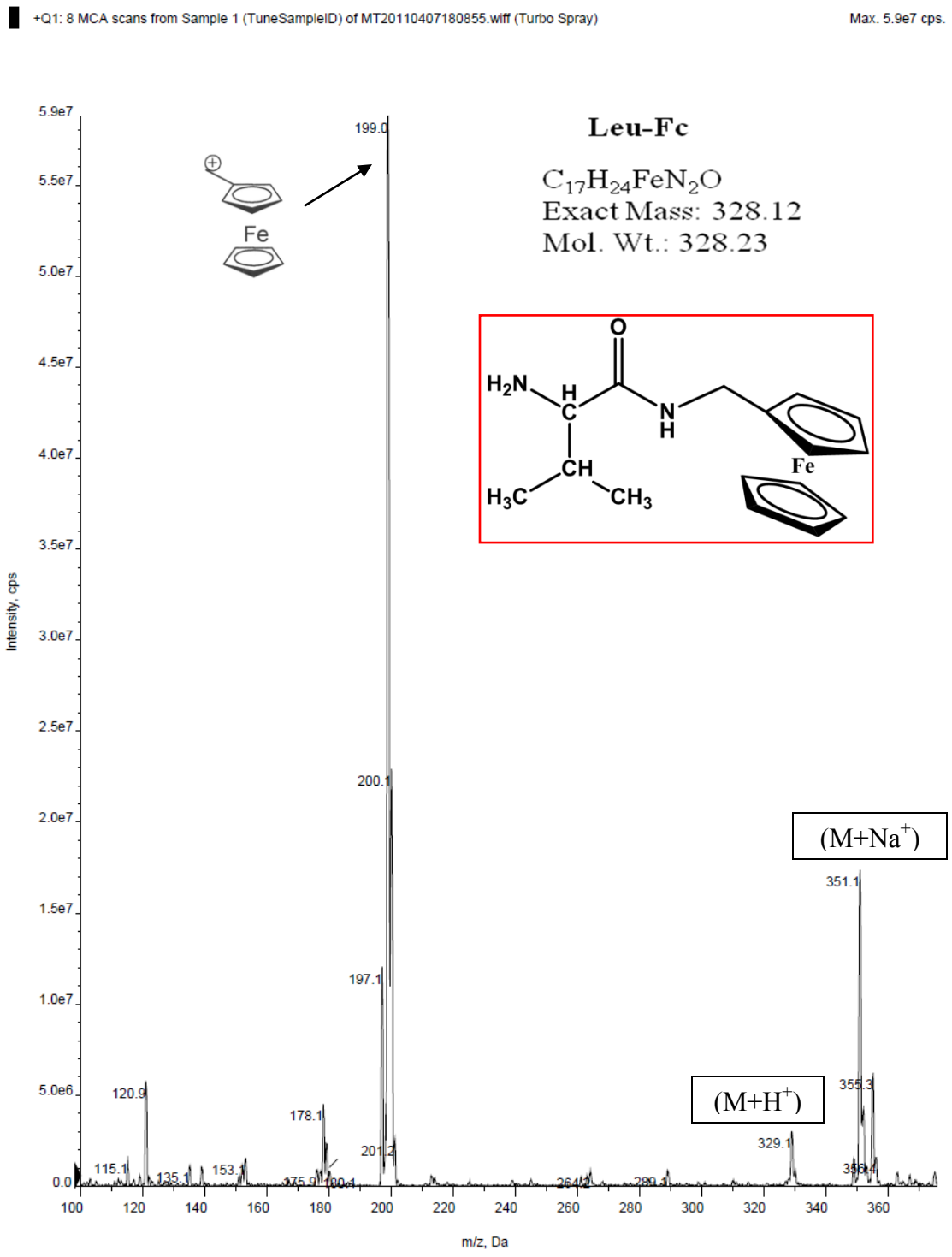

Figure A.9 Mass spectra of authentic Leu-Fc fragment.

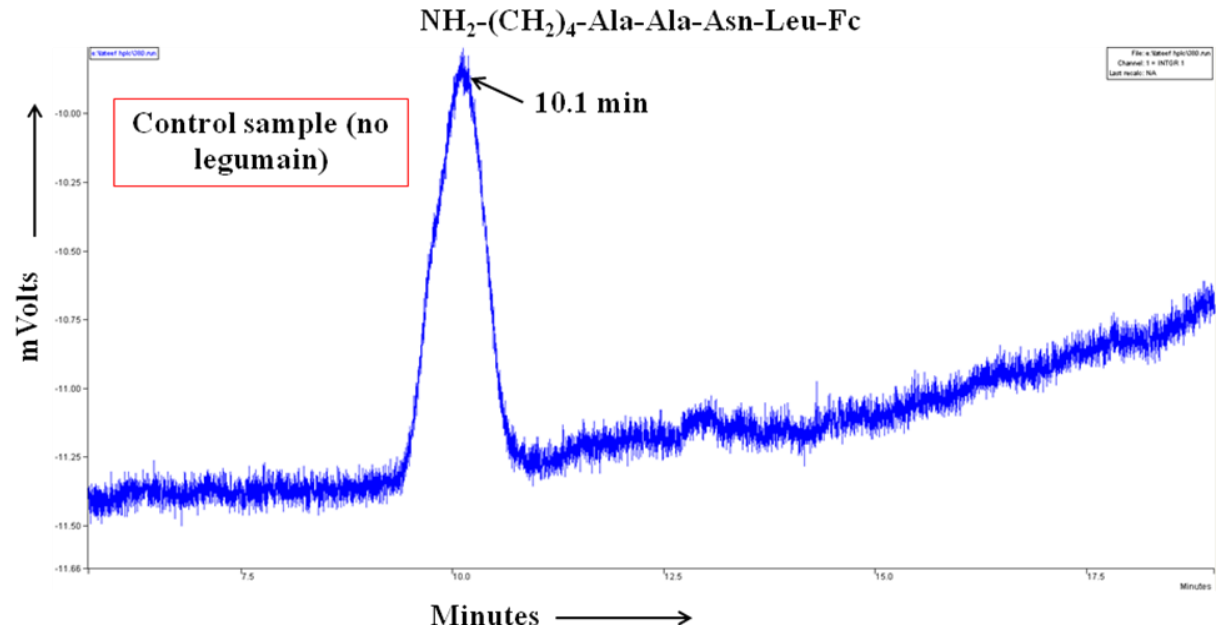

Figure A.10 Chromatogram of control sample i.e. tetrapeptide sample with no legumain added to it. Only one peak at a retention time of 10.1 min can be observed, confirming that no cleavage takes place.

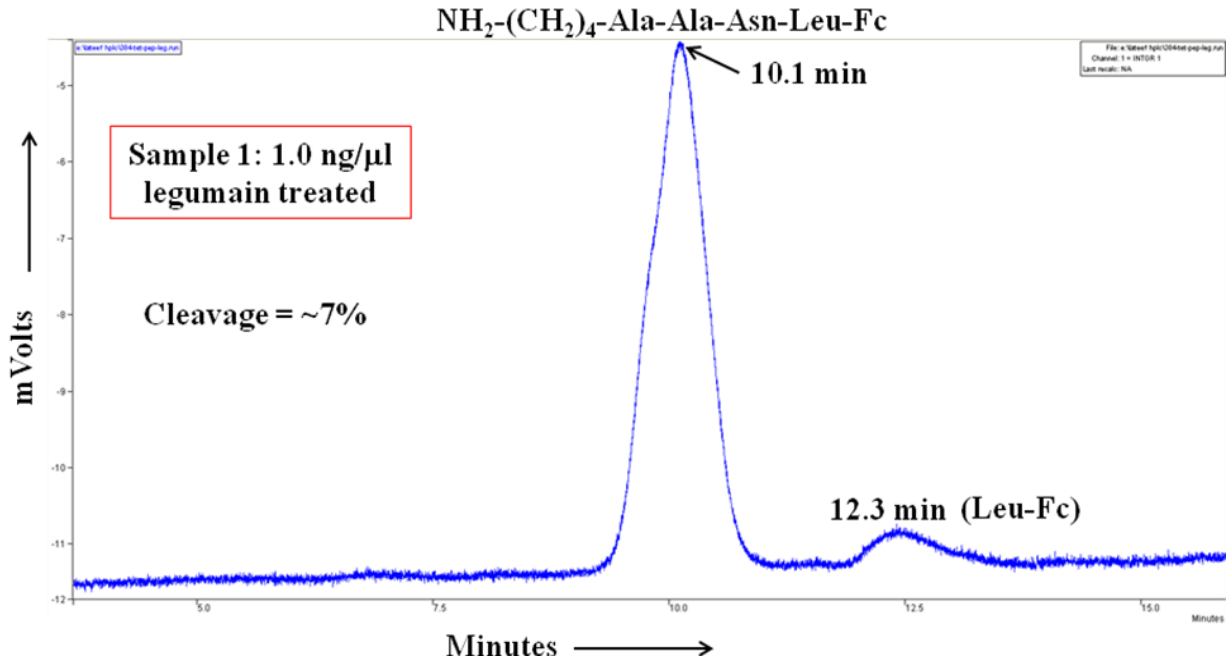

Figure A.11 Chromatogram of tetrapeptide sample (#1) after incubation with 1.0 ng/µl of legumain. Uncleaved tetrapeptide is eluted at 10.1 min and cleaved Leu-Fc fragment is eluted at 12.3 min.

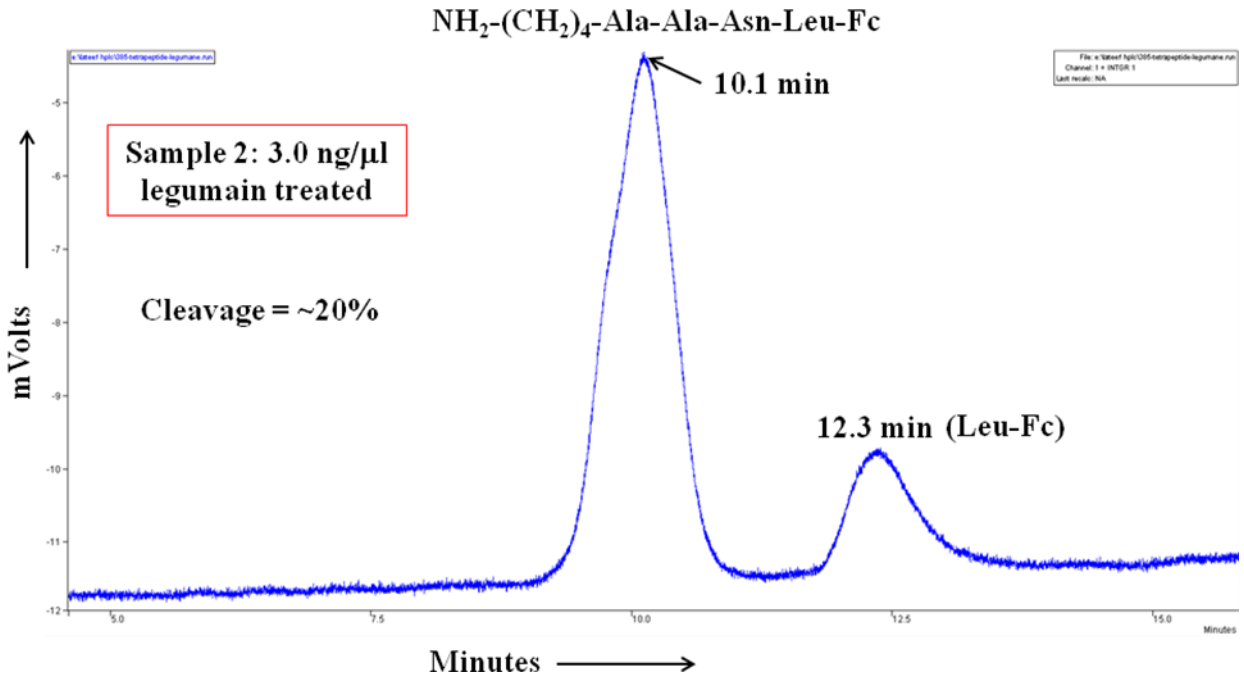

Figure A.12 Chromatogram of tetrapeptide sample (#2) after incubation with 3.0 ng/µl of legumain. Uncleaved tetrapeptide is eluted at 10.1 min and cleaved Leu-Fc fragment is eluted at 12.3 min.

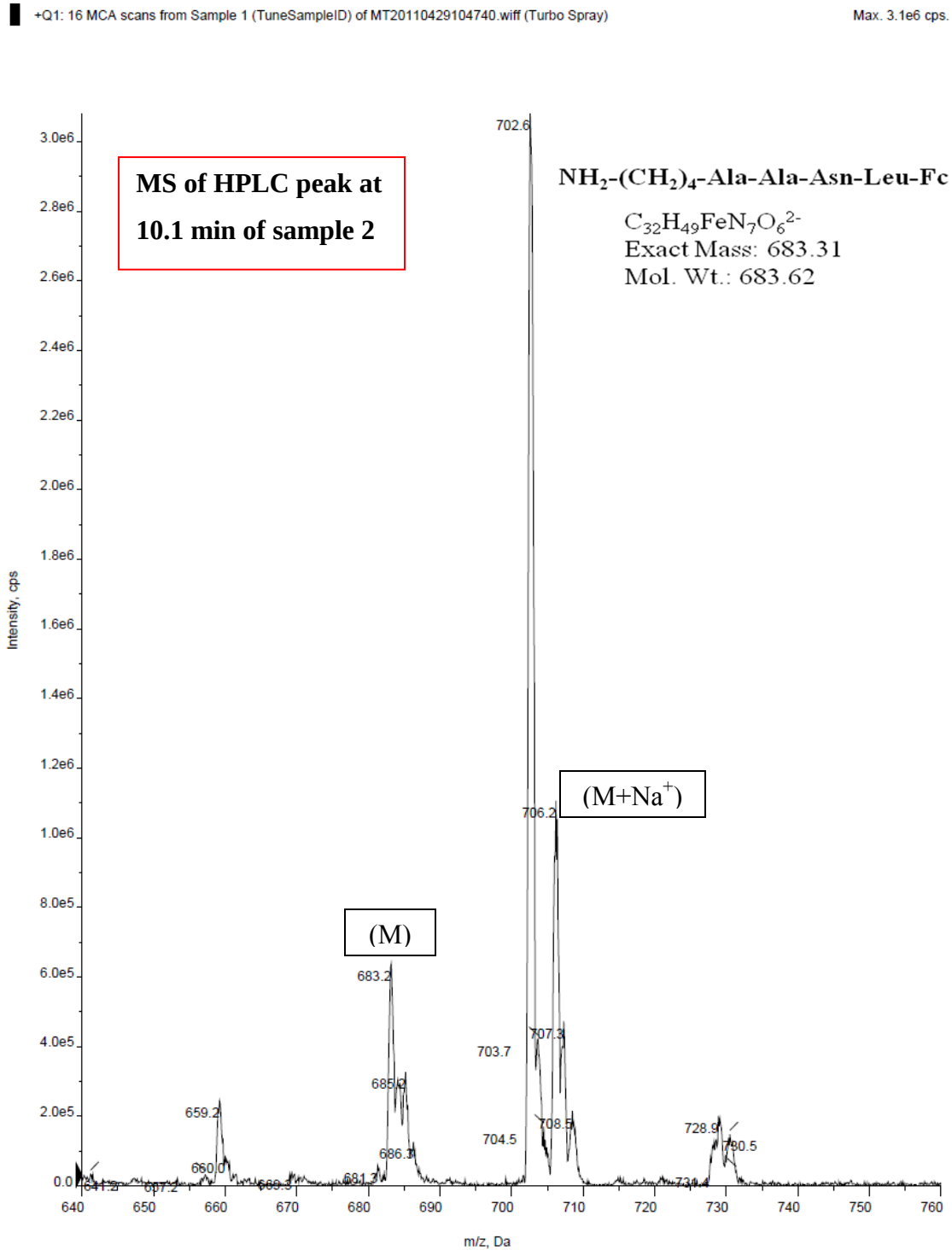

Figure A.13 Mass spectra of peak at 10.1 min of tetrapeptide incubated with legumain (sample #2).

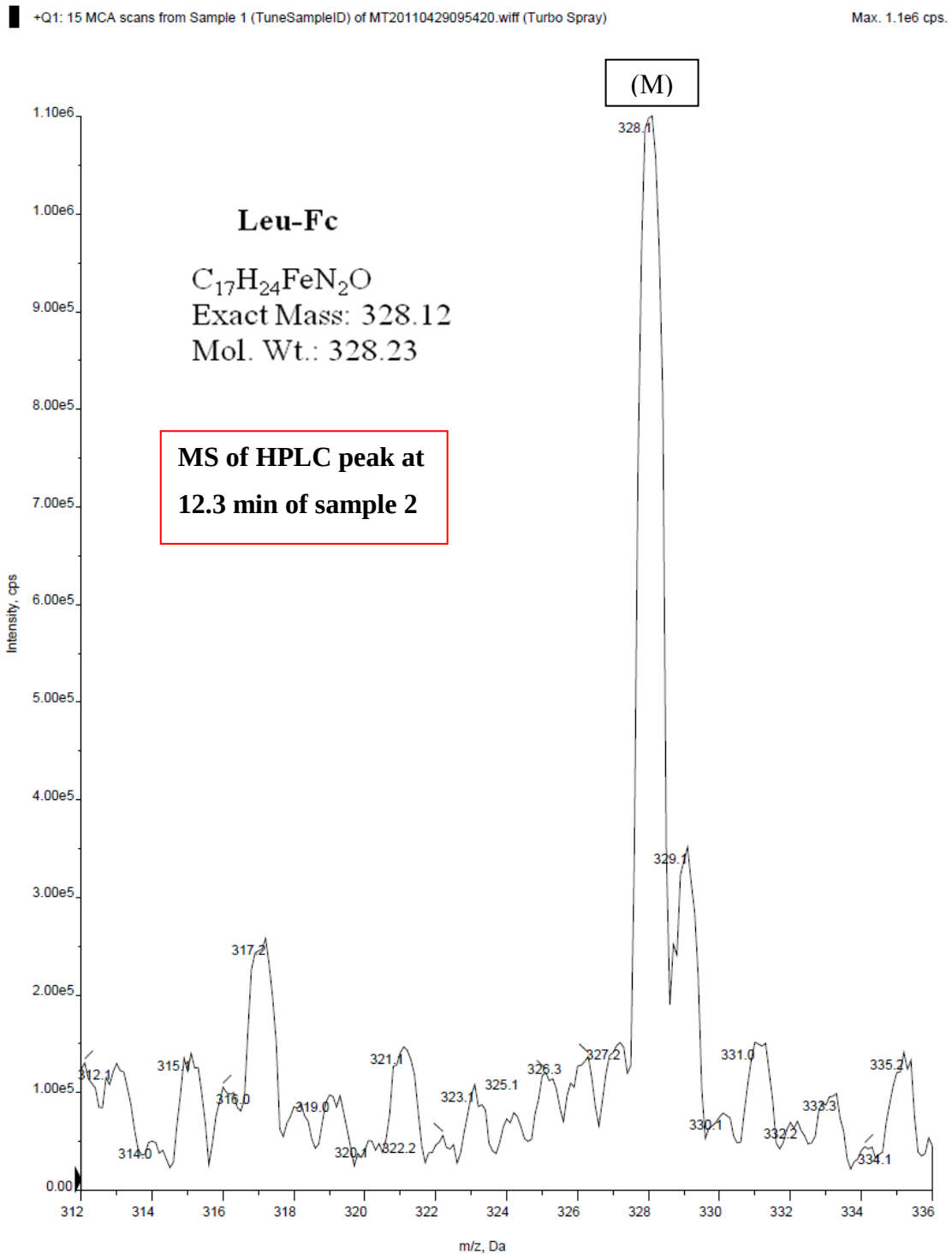

Figure A.14 Mass spectra of peak at 12.3 min of tetrapeptide incubated with legumain (sample #2).

Appendix B - Dielectrophoresis experimental set-up and details

Nano-DEP device and experimental set-up

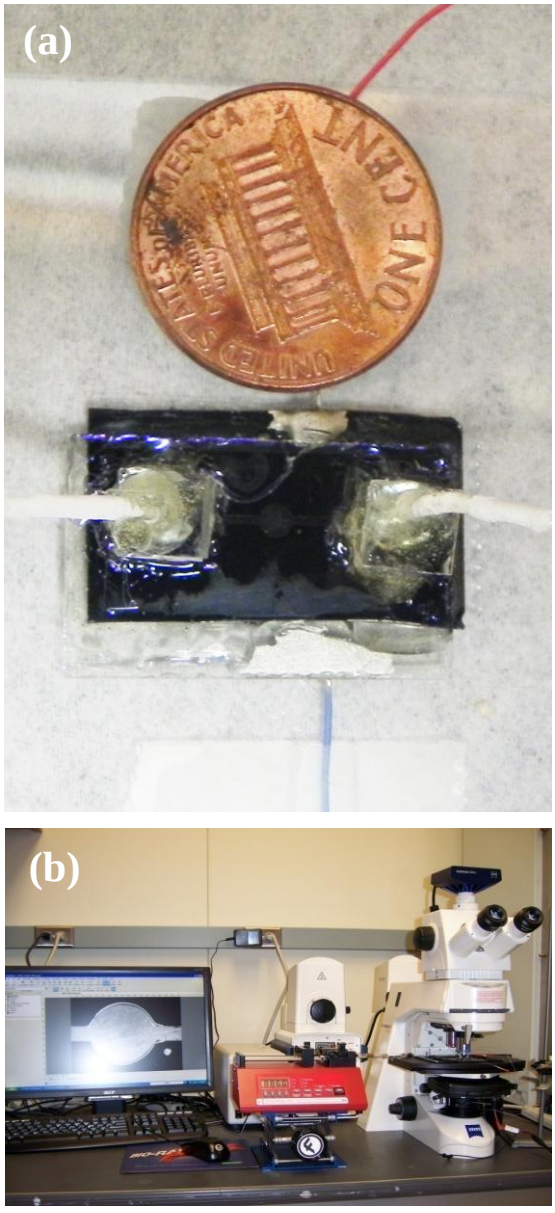

Figure B.1 (a) Shows a nano-DEP device mounted on a glass slide, integrated with microbore tubing and electrical wires. (b) Experimental set-up for DEP and EIS experiments.

Channel heights characterized by a surface profiler

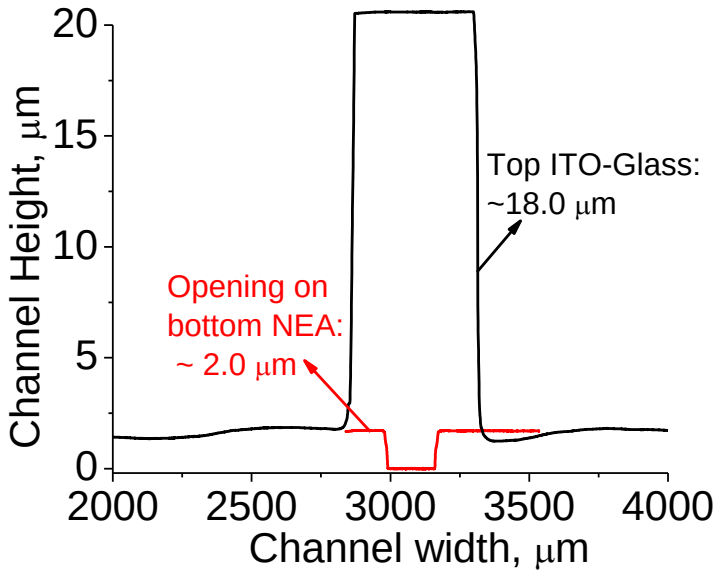

Figure B.2 The microchannel profile measured using profiler. The black curve on the top shows a channel height of ~18.0 μm etched in the SU-8 photoresist on the ITO-glass electrode (flipped upside down in the figure), and the red curve shows the ~2.0 μm deep recessed on the CNF NEA chip to define the 200 μm x 200 μm active area.

Flow velocity profile inside the microfluidic channel

The average flow velocities in the fluidic channel and at the center of the 2 mm diameter circular chamber were calculated from the volumetric flow rate and the channel dimension. More precise flow velocity at the surface of the CNF NEA in the exposed 200 μm x 200 μm area is calculated from the stretched lines in the video. The values are summarized below:

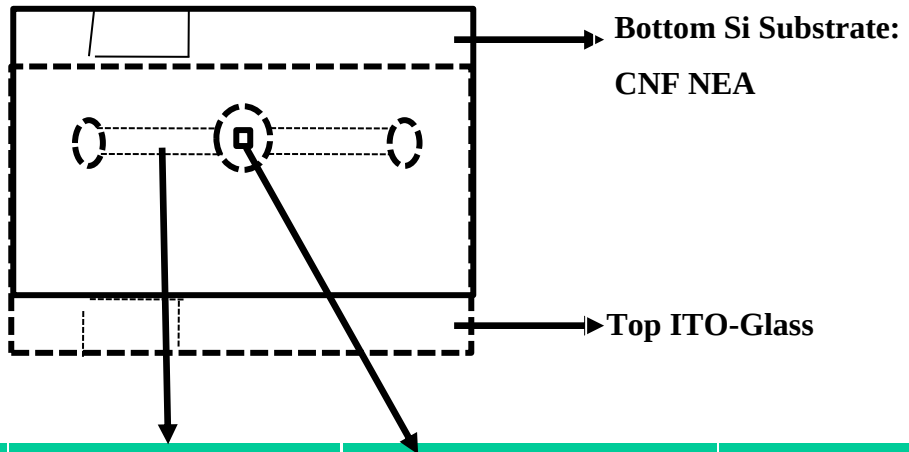

Volumetric flow rate (μl/min)	Average flow velocity in the 500-μm channel	Average flow velocity at the center of the 2-mm dia. circular chamber	Measured flow velocity (From Video)
0.1	0.185 mm/sec	0.046 mm/sec	0.108 mm/sec
0.2	0.370 mm/sec	0.093 mm/sec	0.216 mm/sec
0.4	0.740 mm/sec	0.185 mm/sec	0.432 mm/sec
0.6	1.1 mm/sec	0.278 mm/sec	0.648 mm/sec
0.8	1.5 mm/sec	0.370 mm/sec	0.864 mm/sec
1.0	1.85 mm/sec	0.460 mm/sec	1.1 mm/sec
1.5	2.78 mm/sec	0.695 mm/sec	1.6 mm/sec

Appendix C - Some miscellaneous results related to Chapter 5

UV-Visible spectra of unlysed and lysed sheep blood

Figures C.1a and C.1b below shows UV-Visible spectra of unlysed and lysed blood respectively. As seen in the figures, the lysed sample showed less scattering i.e. less background compared to unlysed blood sample, which is evident by a flat baseline. In case of unlysed blood due to scattering from the intact blood cells higher background can be observed.

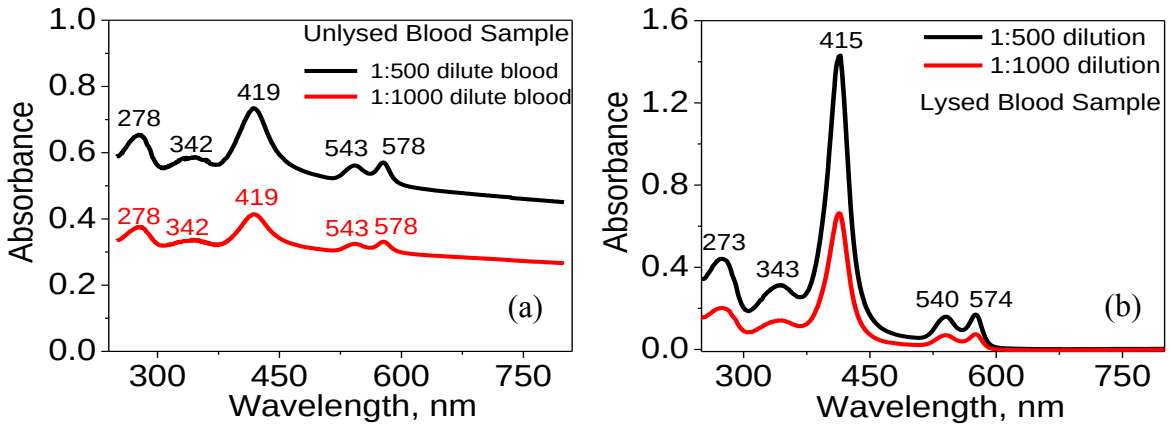

Figure C.1 UV-Visible spectra of (a) unlysed and (b) lysed blood of 500 and 1000 times dilution in 1X PBS buffer.

UV-Visible spectra of luminol

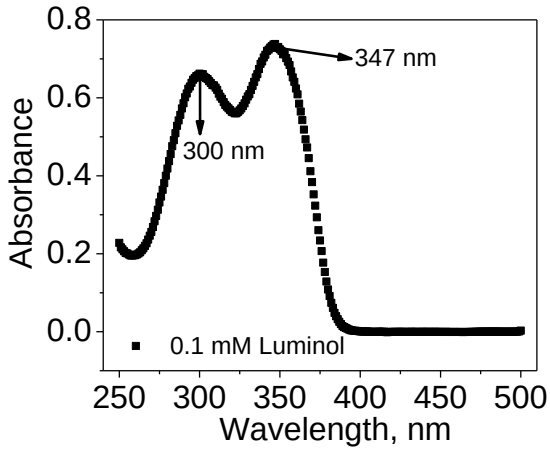

Figure C.2 UV-Visible spectra of 0.1 mM luminol in 0.1 M NaOH solution. Two characteristic peaks at ~347 nm and 300 nm can be seen, consistent with the spectra shown in earlier reports.[1,2]

Chemiluminescence of serially diluted GNP-MUA-LUM solution

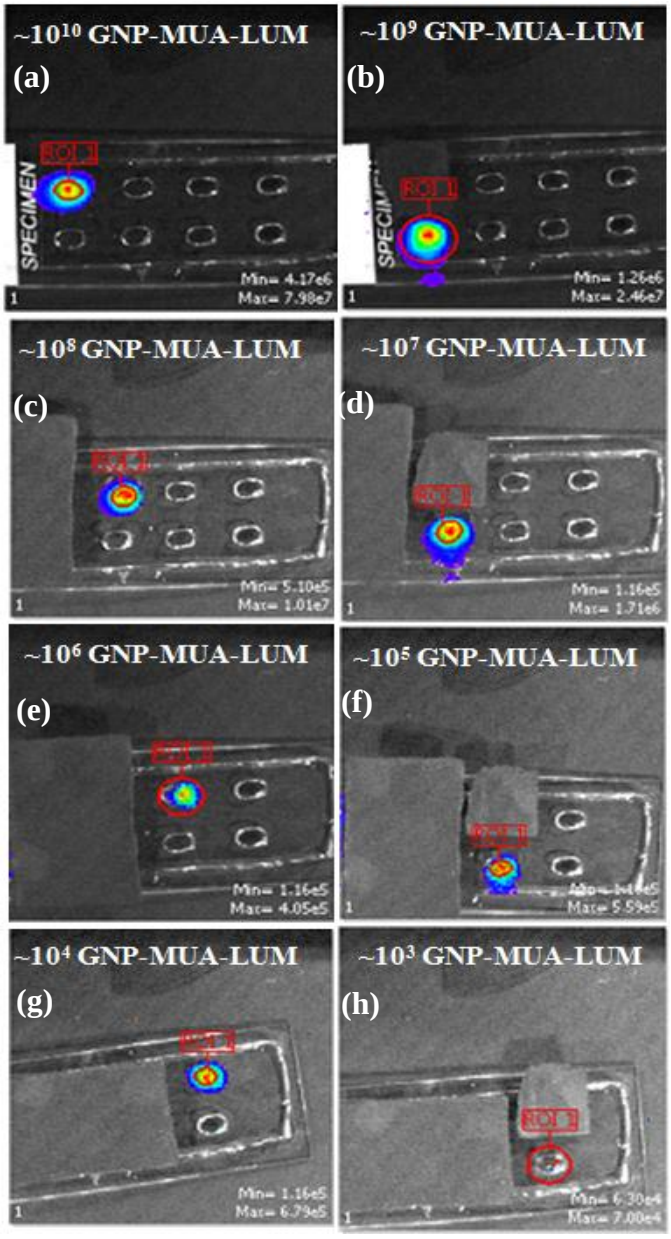

Figure C.3 Chemiluminescence signal recorded by a CCD camera in IVIS Lumina II at PDMS wells loaded with luminol-labeled GNPs (i.e. GNP-MUA-LUM) varying from ~$1.0x10^{10}$ to $1.0x10^{3}$. The images are presented in psuedocolor to represent the chemiluminescence intensities. The number of GNP-MUA-LUM in the well to be measured is indicated on each image. All previously measured wells are covered with a piece of paper to reduce the background.

Comparing chemiluminescence from GNP-MUA-LUM and bulk luminol

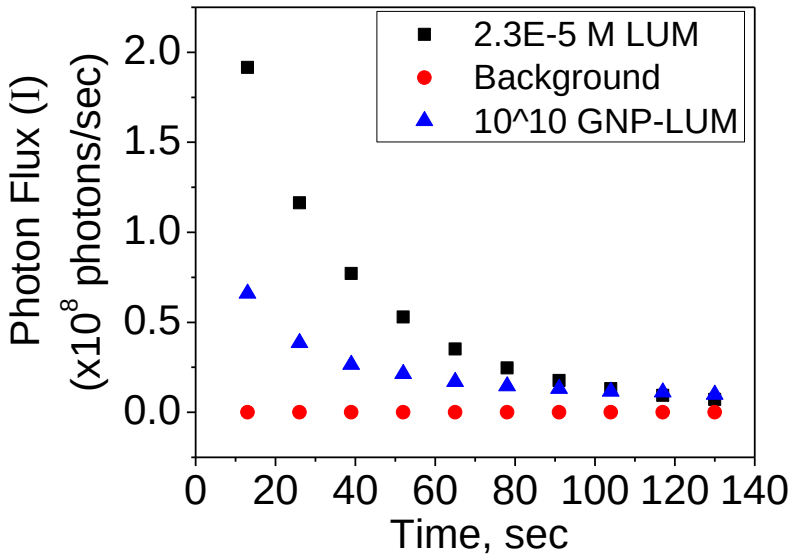

Figure C.4 The comparison of kinetic plots of the CL signal of 1.0×10^{10} luminol-attached gold nanoparticles in a PDMS well (filled triangles), the same amount of luminol molecules dispersed in the solution (filled squares), and blank control sample (filled circles). Each 10-nm-diameter gold nanoparticle is estimated to be attached with ~1.4×10^{3} luminol molecules by assuming the formation of a close-packed monolayer with the same density as that on the flat gold surface. The amount of luminol on 1.0×10^{10} luminol-attached gold nanoparticles is equivalent to 4.0 μL of 23 μM luminol solution used for comparison. The absorption of gold nanoparticles was not corrected.

Analysis of data shown in Figure 5.7 of Chapter 5

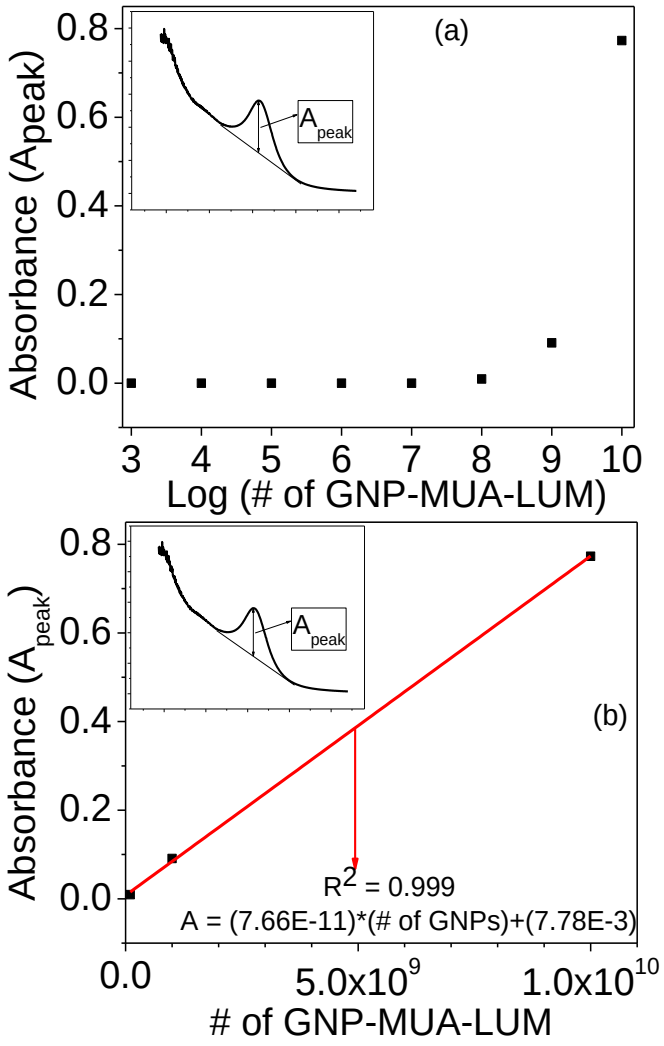

Figure C.5 The background subtracted peak absorption (Apeak) at ~520 nm derived from the UV-visible spectra shown Figure 5.7a and Figure 5.7b. (a) plots the value of A_{peak} vs the logarithm of the number of luminol-labeled GNPs. (b) is the linear plot of A_{peak} vs. number of luminol-labeled GNPs obtained with the sample containing ~$1.0x10^{10}$, $1.0x10^{9}$ and $1.0x10^{8}$ GNP-MUA-LUM. The solid line in (b) is the best fit line, which fits nicely with a linear equation. This indicates that the UV-visible signal linearly decreases till 10^{8} GNPs. At higher dilution (i.e. #GNP-MUA-LUM < 10^{8}) the samples did not show reliable UV-visible signal (as evident from Figure 5.7b). The detection limit by UV-visible absorption is clearly about 10^{7}-10^{8} GNPs/well.

Use of enhancer's to enhance chemiluminescence signal of luminol

It is known that certain enhancers can enhance the CL intensities under appropriate experimental conditions. Commonly p-phenol derivatives are preferred as enhancers to enhance the CL intensity.[3,4] We selected 4-iodophenol as the enhancer to study the CL enhancement effect. CL experiment was performed with 100 times diluted lysed blood sample, along with which 4 µl of 5 mM 4-IP was added. There was ~29 times higher CL intensity observed when compared to the case where no enhancer was added. In future, further careful optimization needs to be done, which may further increase the sensitivity of the CL protocols.

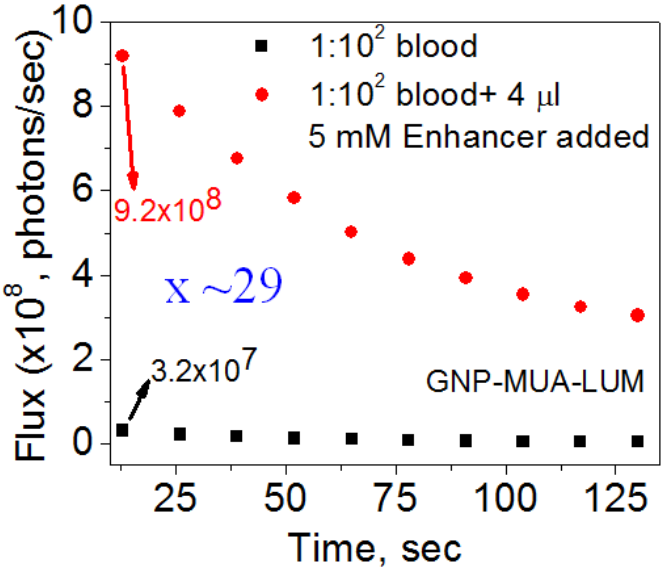

Figure C.6 Chemiluminescence detection of 100 times diluted lysed blood sample with and without enhancer. For the experiment with enhancer 4 µl of 5 mM 4-iodophenol solution (1:1 water and ethanol) was added.

References for Appendix C

1. Sun, Y. G.; Cui, H.; Li, Y. H.; Lin, X. Q. *Talanta* **2000,** *53*, 661-666.
2. Li, S. F.; Li, X. Z.; Xu, J.; Wei, X. W. *Talanta* **2008,** *75*, 32-37.
3. Sanchez, F. G.; Díaz, A. N.; García, J. A. G. *J. Lumin.* **1995,** *65*, 33-39.
4. Kamidate, T.; Maruya, M.; Tani, H.; Ishida, A. *Anal. Sci.* **2009,** *25*, 1163-1166.

Appendix D - List of publications and presentations

Publications

1. Syed, L. U.; Liu, J.; Price, A. K.; Li, Y.-f.; Culbertson, C. T.; Li, J., "Dielectrophoretic Capture of *E. coli* cells at Micropatterned Nanoelectrode Arrays"; *Electrophoresis*, **2011**, 32, 2358-2365 (published in special issue on Dielectrophoresis).
2. Syed, L. U.; Liu, J.; Prior, A. M.; Hua, D. H.; Li, J., "Enhanced Electron Transfer Rates by AC Voltammetry for Ferrocenes Attached to the End of Embedded Carbon Nanofiber Nanoelectrode Arrays"; *Electroanalysis*, **2011**, 23, 1709-1717.
3. Syed. L. U.; Rochford. C.; Wang. F.; Wu. J.; Richter. M.; Balivada. S.; Troyer. D.; Li. J., "An Ultrasensitive Chemiluminescence Method for Trace Blood Detection Using Luminol-Labeled Gold Nanoparticles" manuscript in preparation.
4. Li, Y.-f.; Syed, L. U.; Liu, J.; Hua, D.; Li, J., "Label-free electrochemical impedance detection of kinase and phosphatase activities using nanoelectrode arrays" submitted to *Analytica Chimica Acta*.

Presentations

ORAL

1. Syed, L. U.; Liu, J.; Price, A. K.; Li, Y.-f.; Culbertson, C. T.; Li, J. (2010); "Dielectrophoretic Capture of *E. coli* cells at Nanoelectrode Arrays". Abstracts, 45th Midwest Regional Meeting of the American Chemical Society, Wichita, KS.
2. Syed, L. U.; Madiyar, R. F.; Liu, J.; Price, A. K.; Li, Y.-f.; Culbertson, C. T.; Li, J. (2011); "Using Dielectrophoresis for Reversible Capture and Release of *E. coli* cells at Micropatterned Nanoelectrode Arrays". Abstracts, 46th Midwest Regional Meeting of the American Chemical Society, St Louis, MO.
3. Syed, L. U.; Zhang, L.; Prior, A. M.; Hua, D. H.; Li, J. (2011); "Real-Time AC Voltammetry Based Detection of Cancerous Protease (Legumain) Using

Nanoelectrode Arrays". Abstracts, 46th Midwest Regional Meeting of the American Chemical Society, St Louis, MO.

4. Syed, L. U.; Zhang, L.; Prior, A. M.; Hua, D. H.; Li, J. (Fall-2011); "High-Performance Electrochemical Sensing of Cancerous Protease (Legumain) Using Nanoelectrode Arrays" Abstracts, Materials Research Society, Boston, MA.
5. Syed. L. U.; Rochford. C.; Wang. F.; Wu. J.; Richter. M.; Balivada. S.; Troyer. D.; Li. J. (Spring-2012) "An Ultrasensitive Chemiluminescence Method for Trace Blood Detection Using Luminol-Labeled Gold Nanoparticles" Kansas State University Research Forum, Manhattan, KS.

POSTER

1. Syed, L. U.; Liu, J.; Prior, A. M.; Hua, D. H.; Li, J. (2010); "Distinct Electron Transfer Rates between DC and AC Voltammetry for Ferrocene-Attached Carbon Nanofiber Nanoelectrode Arrays". Abstracts, 45th Midwest Regional Meeting of the American Chemical Society, Wichita, KS.
2. Syed, L. U.; Liu, J.; Price, A. K.; Li, Y.-f.; Culbertson, C. T.; Li, J. (2011); "Dielectrophoretic Capture of *E. coli* cells at Nanoelectrode Arrays". 8th Annual Capitol Graduate Research Summit, Topeka, KS.